

# Integrated Working Fluid and System Optimization for Airborne Waste Heat Recovery Applications

The Onera Dragon Case Study

MSc Thesis

Maarten Krikke



# Integrated Working Fluid and System Optimization for Airborne Waste Heat Recovery Applications

The Onera Dragon Case Study

by

Maarten Krikke

To obtain the degree of Master of Science  
at the Delft University of Technology,  
to be defended publicly on Thursday the 20th of May 2025 at 09:15.

Student Number: 5102111  
Supervisor: C. de Servi  
Daily Supervisor: L. Galieti  
Project Duration: April, 2024 - May, 2025  
Equivalent Wordcount: 22,212

Cover: Onera [34]  
Style: TU Delft Report Style, with modifications by Daan Zwaneveld

# Preface

This report is made for the master thesis project at the faculty of aerospace engineering of TU Delft. Recent research on improving the fuel efficiency of aircraft explores the concept of waste heat recovery to improve power plant efficiency. The recovered power can be converted to electrical power using a generator. If the recovered power exceeds electric power demand, a (partial) turbo-electric configuration can use the electric power for propulsion. This thesis was initiated to study the potential of integrated working fluid optimization for airborne waste heat recovery systems. The propulsion and power department of the aerospace engineering faculty has studied multiple concepts that integrate waste heat recovery into an aircraft. Yet, the working fluid selection has not been thoroughly done. The working fluid for optimal performance depends on the particular system. For land-based systems, system cost is an important factor, while system volume and mass are of little importance. In aircraft design, fuel consumption is not only influenced by the efficiency of the power plant and the propulsion system but also by the mass and volume of the system through the effect on drag. Due to the strong coupling between the different aspects of the system, making an optimal design choice is difficult. In such a case, optimization algorithms can be used to discover optimal design choices that are not obvious to a designer.

I want to thank Lorenzo for his accessible supervision and especially for taking the time to help in the early stages of the thesis when it was difficult to get familiar with the code developed in previous works. Also, thanks to Carlo for providing helpful guidance in the later stages of the project. Thanks to Fabio for thinking along about the approach to take. Finally, Thanks to Mees, Edoardo, and Nicholas for the periods we shared a master room and had breaks from working on the thesis together.

*This work used the Dutch national e-infrastructure with the support of the SURF Cooperative using grant no. EINF-10795*

*Maarten Krikke  
Delft, May 2025*

# Summary

Aviation is simultaneously a great asset in connecting the world and an environmental burden. Starting at the beginning of the jet age, innovation in passenger aircraft design strongly focused on reducing fuel consumption. Throughout the decades, the physical limits to the performance of the conventional aero engine architecture have been approached. For this reason, disruptive architecture changes are needed to sustain progress in reducing fuel consumption. One disruptive architecture change is to adopt waste heat recovery in a (partial) turboelectric aircraft configuration. Previous works have studied the potential of such waste heat recovery systems applied to the Onera Dragon turboelectric aircraft concept.

The previous works have not yet thoroughly studied the role of the working fluid in the performance of the waste heat recovery system. Krempus et al. use cyclopentane as a working fluid. Their analysis shows the system can indeed realize fuel savings, albeit by a relatively small amount. Subsequently, Sinopoli et al. examined the performance of the same system with ethanol and toluene as additional working fluid options; they found a slight advantage for ethanol but concluded the difference is negligible.

In this work, the Perturbed Chain (PC)-Statistical Associating Fluid Theory (SAFT) equation of state is used as the fluid model, supplemented with Quantitative Structure Property Relationship (QSPR)s for additional fluid properties. Subsequently, the design vector is extended with the PC-SAFT parameters. An optimization of this design vector will most likely not converge to PC-SAFT parameters of a real fluid, in which case the term pseudo-fluid is used. Since, in the end, only real fluids are of interest, the closest neighboring real fluid to each pseudo-fluid optimum is identified as the one with the smallest Euclidean norm distance in PC-SAFT parameter space, and system performance is then evaluated for this real fluid. Additionally, a bi-objective optimization is performed, which, in addition to minimizing total fuel mass, also includes an objective that reduces this distance to encourage convergence toward real-fluid properties. Conceptually, the real fluids can be thought of as discrete "attractors" in the continuous PC-SAFT parameter space, with the optimization navigating toward the best-performing one. Finally, binary non-polar fluid mixtures are also assessed by optimizing the composition of a pseudo-mixture.

For the pure pseudo-fluids, a 1.56% fuel savings by the Organic Rankine Cycle (ORC) system is found. This is a slight improvement compared to the reference fuel savings of 0.92% for the ORC system using cyclopentane. The best real fluid counterpart to a pseudo-fluid is found to be acetyl chloride, featuring a 1.37% improvement over the original Dragon aircraft as evaluated in this work. The pseudo-fluid and real-fluid optima could not be identified using a bi-objective optimization. Optimizations of non-polar pseudo-fluid mixtures did not show improvement over the pure fluids. An optimization with the fixed PC-SAFT parameters of cyclopropane and cyclopentane with a varying mixture fraction showed a tendency for the mixture fraction to go toward the bounds. This points to the fact that the system cannot benefit from a temperature glide in the condenser.

It is recommended that bi-objective optimization be tested more thoroughly to verify its ability to find the real fluid optima in one step. As a general method for working fluid optimization, it can offer an efficient process. While it is not suspected that there is a substantial improvement margin over the results obtained, binary mixtures of polar (pseudo) fluids can still be optimized to prove this more rigorously. Finally, the work does indicate that integrated working fluid optimization is worthwhile for airborne waste heat recovery systems. Conducting an integrated working fluid optimization for other, better-performing airborne waste heat recovery system architectures is highly recommended.

# Contents

<b>Preface</b>	<b>i</b>
<b>Summary</b>	<b>ii</b>
<b>Nomenclature</b>	<b>v</b>
<b>1 Introduction</b>	<b>1</b>
1.1 Background . . . . .	1
1.2 Research Objective and Question . . . . .	5
1.3 Report Outline . . . . .	5
<b>2 Literature Review on Integrated Working Fluid and Process Optimization</b>	<b>6</b>
2.1 The Heuristic Approach . . . . .	6
2.1.1 Key Fluid Properties Affecting the Cycle . . . . .	7
2.1.2 Additional Relevant Fluid Properties . . . . .	7
2.2 Fluid Property Models . . . . .	8
2.3 Computer Aided Working Fluid Optimization . . . . .	9
2.4 Working Fluid Mixtures . . . . .	11
<b>3 Methodology</b>	<b>12</b>
3.1 Aircraft and Propulsion System Model . . . . .	12
3.1.1 Aircraft Overview . . . . .	12
3.1.2 Combined Cycle Power Unit . . . . .	13
3.2 Working Fluid Optimization Approach . . . . .	18
3.2.1 Continuous-Molecular Targeting . . . . .	19
3.2.2 Finding a Real Fluid . . . . .	19
3.2.3 Fluid Database and Convex Hull . . . . .	20
3.3 Optimizer Details . . . . .	21
<b>4 Results</b>	<b>26</b>
4.1 Reference Cases . . . . .	26
4.1.1 Original Dragon Aircraft . . . . .	26
4.1.2 Cyclopentane Baseline Case . . . . .	27
4.2 Working Fluid Optimization Results . . . . .	29
4.2.1 Optimized CCPU using Pure Fluids . . . . .	29
4.2.2 Optimized CCPU using Fluid Mixture CoMT . . . . .	39

---

4.3 Parametric Studies . . . . .	44
4.3.1 Core exhaust nozzle pressure ratio trend for cyclopentane as working fluid . . .	44
4.3.2 Core exhaust nozzle pressure ratio trend for pseudofluids as working fluids . . .	45
<b>5 Conclusions and Recommendations</b>	<b>48</b>
<b>References</b>	<b>50</b>
<b>A Figures Related to Fluid Modeling</b>	<b>55</b>

# Nomenclature

## Symbols

$\Pi$	Pressure ratio	$Q$	Heat flux
$T$	Temperature	$C_D$	Drag coefficient
$p$	Pressure	$C_{D,\min}$	Minimum drag coefficient
$m$	Segment length	$C_L$	Lift coefficient
$\sigma$	Segment diameter	$C_{L,\min}$	Minimum lift coefficient
$\epsilon_k$	Segment dispersion energy	$K_L$	Drag polar coefficient
$\mu$	Dipole moment	$\epsilon^{A_i B_i}$	Associating energy
$z$	Mixture fraction	$\kappa^{A_i B_i}$	Associating volume
$m_t$	Total mass	$F_{RAD}$	Cumulative ram air duct thrust of one CCPU
$m_{t,oe}$	Operating empty mass	$\dot{m}_{RAD}$	Ram air duct massflow
$\dot{m}$	Mass flow rate	$\Delta T_{GL}$	Condenser temperature glide
$\mathbf{q}$	PC-SAFT parameter vector	$m_{t,TO}$	Maximum take-off mass
$\eta$	Efficiency	$\dot{m}_{fuel}$	Fuel mass flow rate
$\psi$	Work coefficient	$\eta_{trans}$	Total efficiency of transmission
$\phi$	Flow coefficient	$\eta_{acdc}$	AC-DC conversion efficiency
$f_1$	Primary objective function	$\eta_{pmu}$	Power management unit efficiency
$f_2$	Secondary objective function	$\eta_{dcac}$	DC-AC conversion efficiency
$\dot{W}$	Power	$\eta_{mot}$	Motor efficiency
$D$	Drag	$D$	Drag force
$F$	Thrust	$F_{jet}$	Core thrust of one CCPU
$Z$	Mixture fraction	$V_\infty$	Freestream velocity
$\phi_1$	Louver angle	$m_{cr}$	Reference aircraft mass for cruise
$b_f$	Fin height	$m_{fuel,cr}$	Fuel mass consumed during a nominal mission
$p_f$	Fin pitch	$F_{RAD}$	Net force of a single ram air duct
$w_{mc}$	Microchannel width	$\eta_{pp,core}$	Efficiency from fuel to propulsive power from the core exhaust
$n_{pass}$	Number of passes	$\eta_{pp,EDF,RAD}$	Efficiency from fuel to propulsive power from the ram air duct and electric ducted fans
$\xi$	Intake massflow ratio	$\dot{W}_{pp,req}$	Required propulsive power in the cruise condition
$\theta_{cond}$	Condenser tilt angle		
$c_p^{ig}$	Ideal gas isobaric specific heat		
$B$	Exergy		
$x_{t,evap}$	Evaporator transverse pitch		
$x_{l,evap}$	Evaporator longitudinal pitch		

## Sub- and Superscripts

pu	Power unit	<i>s</i>	Isentropic
cond	Condenser	$N_{\text{mech}}$	Shaft rotational velocity
orc	Organic Rankine cycle	LPC	Low pressure compressor
ccpu	Combined cycle power unit	HPC	High pressure compressor
HS	Hotside	HPT	High pressure turbine
CS	Coldside	LPT	Low pressure turbine
evap	Evaporator	FPT	Free power turbine
noz	Core exhaust nozzle	ORCT	ORC turbine
ts	Turboshaft	tf	Total fuel
t	Total	av	Available
red	Reduced	chem	Chemical
pf	Pseudo fluid	pump	Pump
rf	Real fluid	mot	Electric motor
mp	Midpoint	cr	Cruise
0	Free stream	trans	Transmission
1	Inlet entrance	acdc	AC–DC conversion
2	Compressor entrance	pmu	Power management unit
3	Combustor entrance	dcac	DC–AC conversion
4	High pressure turbine entrance	prop	Propulsion
42	Low pressure turbine entrance	gen	Generator
45	Free power turbine entrance	mech	Mechanical shaft
5	Evaporator entrance	th	Thermal
7	Evaporator exit	TO	Take-off
9	Nozzle exit	EDF	Electric Ducted Fans
<i>poly</i>	Polytropic		

## Acronyms

<b>BM</b>	Binary Mixture	<b>HRSG</b>	Heat Recovery Steam Generator
<b>BTB</b>	Bare Tube Bundle	<b>HTC</b>	Heat Transfer Coefficient
<b>CAMD</b>	Computer Aided Molecular Design	<b>L/D</b>	Lift-to-Drag Ratio
<b>CC-TS</b>	Combined-Cycle Turboshaft	<b>LCOE</b>	Levelized Cost of Energy
<b>CCPU</b>	Combined Cycle Power Unit	<b>LHV</b>	Lower Heating Value
<b>CNRF</b>	Closest Neighbouring Real Fluid	<b>LMTD</b>	Logarithmic Mean Temperature Difference
<b>CoMT</b>	Continuous-Molecular Targeting	<b>MO</b>	Multi-Objective
<b>EDFs</b>	Electric Ducted Fans	<b>NPPF</b>	Non-Polar Pseudo-Fluid
<b>EIS</b>	Entry Into Service	<b>ODP</b>	Ozone Depletion Potential
<b>EOS</b>	Equation of State	<b>OPR</b>	Overall Pressure Ratio
<b>ERF</b>	Effective Radiative Forcing	<b>ORC</b>	Organic Rankine Cycle
<b>FPT</b>	Free Power Turbine	<b>PC</b>	Perturbed Chain
<b>GCM</b>	Group Contribution Method	<b>PPF</b>	Polar Pseudo-Fluid
<b>GHG</b>	Greenhouse Gas	<b>PR</b>	Peng-Robinson
<b>GWP</b>	Global Warming Potential	<b>PSFC</b>	Power Specific Fuel Consumption

---

<b>QSPR</b> Quantitative Structure Property Relationship	<b>TIT</b> Turbine Inlet Temperature
<b>SAFT</b> Statistical Associating Fluid Theory	<b>TLARs</b> Top-Level Aircraft Requirements
<b>SFC</b> Specific Fuel Consumption	<b>WHR</b> Waste Heat Recovery

# 1

## Introduction

First, in section 1.1, the motivation for improving the efficiency of aircraft engines and the concept of airborne waste heat recovery are discussed. Then, in section 1.2, the research question for this work is explained. Finally, section 1.3 provides an outline of this thesis report.

### 1.1. Background

Air transport is an invaluable asset in connecting different parts of the world on timescales unmatched by any other mode of transport. Unfortunately, the tight technological constraints on aircraft and their mass result in the continued use of fossil fuels, with over 2.5% of global fossil energy consumption in 2019 attributed to aviation.<sup>1</sup> The share of global warming (Effective Radiative Forcing, ERF) attributed to aviation is even greater and is estimated at 3.5% in 2011 [28].<sup>2</sup> At first glance, this percentage might not seem significant. However, according to a report by Possible [12], an estimated 2% of the population in France is responsible for 50% of the flights by French citizens. If everyone had such flying habits, global fossil energy consumption would increase by almost 60%, and the share of fossil energy consumed by aviation would increase to a staggering 39%.<sup>3</sup> This underscores the need to sufficiently reduce Greenhouse Gas (GHG) emissions from aviation through innovation, market-based regulations, or a combination of both.

Climate impact reduction through technological innovation can be broken down into two key factors: low specific ERF fuel-aircraft combinations and reduced fuel consumption per passenger-kilometer. The latter is, in part, determined by the conversion efficiency of the propulsion system.

Motivated primarily by cost savings, aircraft and engine manufacturers have focused on reducing aircraft fuel burn. Between 1970 and 2019, the average block fuel intensity<sup>4</sup> of new aircraft decreased by 41% [43]. However, between 2009 and 2019, the CO<sub>2</sub> emissions from commercial airlines increased by 44%. This indicates that the growth in air travel has far outpaced the reduction in block fuel intensity. This phenomenon aligns with the rebound effect first identified by Jevons [21], who observed that efficiency improvements do not necessarily mitigate the scarcity of fuels—or, in this context, the negative climate impact caused by fuel consumption.

While one might question the certainty that investing in energy efficiency improvements will lead to a reduction in climate impact, it can be said with confidence that, for a given GHG emission budget and all other factors held constant, efficiency improvements will enable a greater capacity for air transport.

---

<sup>1</sup>Global fossil fuel usage (accessed 28-01-2025): <https://ourworldindata.org/fossil-fuels>, Jet fuel usage (accessed 28-01-2025): <https://www.statista.com/statistics/655057/fuel-consumption-of-airlines-worldwide/>, Jet fuel properties (accessed 28-01-2025): <https://www.exxonmobil.com/en/aviation/products-and-services/products/exxonmobil-jet-a-1>

<sup>2</sup>The discrepancy is on one hand explained by non-CO<sub>2</sub> effects and on the other hand by the variation in CO<sub>2</sub> intensity of different fossil fuels.

<sup>3</sup>Assuming the global share of fossil energy usage is representative for France and vice versa for the global jet fuel usage. All other fossil fuel usage is assumed to remain equal.

<sup>4</sup>Measured in grams of fuel per tonne-kilometer.

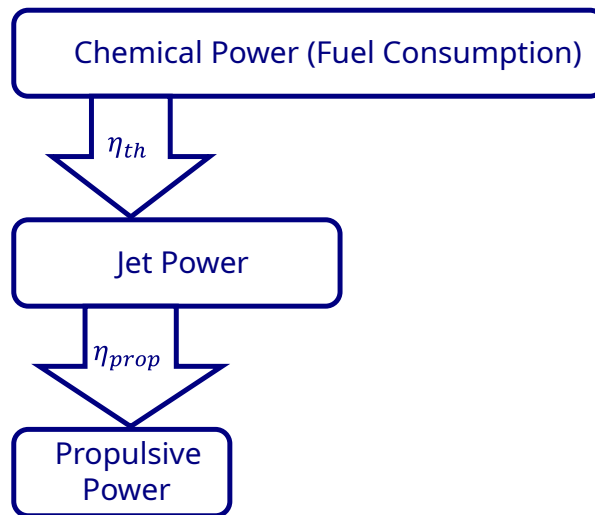


**Figure 1.1:** Illustration of the fuel consumption decoupling.

The fuel or energy consumption of an aircraft can be analyzed through three key factors: (I) the required power (which is equal to the propulsive power), (II) the propulsive efficiency ( $\eta_{prop}$ ), and (III) the thermal efficiency ( $\eta_{th}$ ). The latter two aspects are particularly relevant to the design of the propulsion system. Propulsive efficiency is primarily determined by the amount of accelerated air mass flow per unit of thrust force. However, improving this efficiency is not the primary focus of the current work.

Thermal efficiency refers to the portion of the energy contained in the fuel that is converted into either shaft power or the kinetic energy of the jet flow. The remaining energy is expelled into the environment as hot exhaust gas. Most aircraft engines produce power using gas turbines. The ideal cycle corresponding to a gas turbine is called the Brayton cycle.

The efficiency of a Brayton cycle can be improved by increasing the Overall Pressure Ratio (OPR) which is defined as the total pressure at the high pressure compressor exit divided by the total pressure at the compressor (or fan) inlet. The OPR can be increased if the Turbine Inlet Temperature (TIT) is sufficiently high. However, an increased TIT faces material limitations and the production of nitrogen oxides ( $\text{NO}_x$ ) due to the high temperature. Also, the OPR is constrained by material limitations at the compressor outlet due to the high compressed air temperature. This means the OPR cannot be increased indefinitely for efficiency improvement. Additional efficiency gains may be achieved by recovering thermal power from the hot exhaust gas and converting it into additional mechanical or electric power. This process is known as Waste Heat Recovery (WHR). While this concept is already common in land-based power generation, where mass and volume constraints are less important, it has not been applied in aviation yet.

Waste heat, or heat in general, can be harnessed to generate power through various thermodynamic cycles. The Rankine cycle is the most common ideal cycle used for this purpose. It is characterized by the addition of heat to evaporate the working fluid, typically water. If the maximum pressure of the cycle is below the critical pressure of the working fluid, the cycle is referred to as a subcritical Rankine cycle. If the maximum pressure exceeds the critical pressure, the cycle is termed a supercritical Rankine cycle. In subcritical cycles,<sup>5</sup> the working fluid can be superheated (heated beyond its saturation temperature) before it expands in a turbine. If the fully vaporized liquid is not superheated and remains saturated throughout the process, the cycle is called a saturated Rankine cycle. This classification is summarized in Table 1.1. After expansion in the turbine, the working fluid releases its remaining thermal energy during the condensation phase, where it is cooled and brought back into the liquid phase. The condensate is then pumped back to the boiler, completing the cycle. A T-s diagram of a subcritical, saturated Rankine cycle and a process flow diagram illustrating the system components are shown in Figure 1.2. It can be recognized that the cycle is saturated because point 3 lies on the saturated vapor

<sup>5</sup>In supercritical cycles, the working fluid can also be heated to any temperature. However, a saturation temperature cannot be defined such that the term superheating is not applicable.

	$p_{\max} > p_{\text{crit}}$	Subcritical & $T_{\max} > T_{\text{evap}}$
False	Subcritical	Saturated
True	Supercritical	Superheated

**Table 1.1:** Rankine cycle terminology.

line. If point 4 is not within or on the edge of the saturation dome, this indicates that the fluid needs to be desuperheated before it can condense. The line segment between point 4 and the saturated vapor line represents the desuperheating phase.

The Rankine cycle is widely utilized in land-based power plants to exploit the thermal energy in the gas turbine exhaust gases. The Rankine cycle has two key advantages: first, compression in the liquid phase requires low pump power. Additionally, heat transfer during phase transition (evaporation or condensation) allows for heat addition to occur close to the maximum cycle temperature, and heat rejection to take place essentially at the minimum cycle temperature, thereby minimizing irreversibilities and enabling high conversion efficiency. When an organic working fluid is used (defined as containing carbon atoms<sup>6</sup>), the cycle is referred to as the Organic Rankine Cycle (ORC).

For the Rankine cycle, the optimal configuration and choice of working fluid depend on the heat source's power and temperature. According to Macchi and Astolfi [31, p. 6], 'ORCs are the unrivaled technical solution for generating electricity from low-medium temperature heat sources of limited capacity.' They further explain that the main advantage of organic working fluids is that the resulting turbine design is simpler than when water is used. This is partly because water partially condensates during expansion when it is not sufficiently superheated. This condensate leads to excessive turbine wear and decreased performance [31, p. 15]. Additional considerations concerning working fluid properties and the process design are given in subsection 2.1.1. For WHR in aviation, lightweight, and thus simple, equipment is needed. Also, the available waste heat power is in the order of a few tens of MW. Thus, the ORC is most suitable for airborne WHR.

One of the earlier works on an airborne ORC application for a commercial turbofan-powered aircraft is that of Perullo et al. [37]. They explain that steam-based heat recuperation is not feasible for aircraft gas turbines for multiple reasons. These include manufacturing cost, system weight, water supply, and poor performance for low power levels. They add that ORCs, on the other hand, are 'ideal for extracting low grade heat', which is in agreement with what is stated by Macchi and Astolfi. From the work of Perullo, it is found that an ORC unit added to a CFM56 turbofan engine (this engine is used, for example, on the Boeing 737 family) to drive a cabin air compressor could reduce the Specific Fuel Consumption (SFC) by 2.2%. They find a fuel burn, that is, mission fuel mass reduction of 0.9%. However, the pressure drop in the heat exchangers is neglected meaning that this is a somewhat optimistic figure. Nonetheless, it does demonstrate that using an ORC to recuperate waste heat from an airborne gas turbine is worth exploring further. Further research into airborne WHR was done in subsequent years. De Servi et al. [50] did a study on WHR using CO<sub>2</sub> as a working fluid. The recovered power is used to produce thrust. The equipment required for this is not specified. They could not realize a reduction in fuel burn, mainly due to their high estimate of the system mass for the bottoming cycle. Hughes and Olson [20] studied an ORC unit coupled with an internal combustion engine for a parallel-hybrid electric drivetrain for small regional aircraft. They found a fuel burn reduction of 13%. However, multiple side notes should be made for this figure. Firstly, this result would likely not be achieved when applying an ORC system to a turbofan-powered commercial aircraft since an internal combustion engine cannot be readily compared to a gas turbine. Also, the architecture involves a traction battery providing power in the climb phase. This might be a relevant difference since small aircraft have rather different flight profiles compared to (large) passenger aircraft. Finally, the study did not consider the volumetric sizing of the ORC equipment, meaning that the effect on drag is not accounted for.

More recently, Krempus et al. developed a framework they call *ARENA*; this name stands for Airborne Energy Harvesting for Aircraft. The *ARENA* framework evaluates the fuel consumption of an aircraft

<sup>6</sup>With a few exceptions, see <https://www.britannica.com/science/organic-compound> (accessed 28-01-2025).

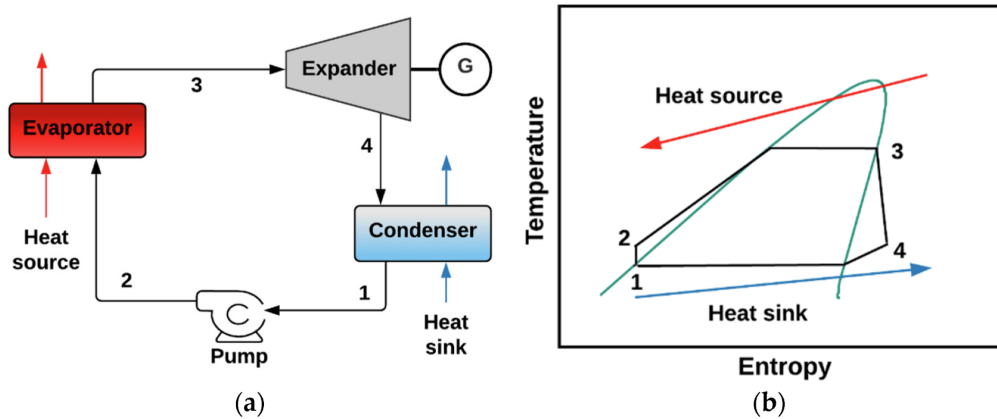


**Figure 1.2:** ORC system schematic (left) and T-s diagram illustration of a subcritical, saturated Rankine cycle (right).  
Reproduced from ref. [22].

equipped with an ORC-based WHR system, focusing on modeling the engine in detail.

In ref. [7], Krempus et al. use the *ARENA* framework to evaluate waste heat recovery for the Onera Dragon turboelectric aircraft. A turboelectric aircraft has turboshaft engines that drive generators. The generators deliver electric power to an electric propulsion system. The Onera Dragon has an under-the-wing distributed electric propulsion system consisting of 26 Electric Ducted Fans (EDFs) in total. Two turboshaft engines are mounted on the tail, one on either side. Krempus et al. include a supercritical ORC system to recover heat from the exhaust gas and produce part of the power required by the propulsion system. The working fluid chosen by Krempus et al. is cyclopentane. A set of 18 parameters related to mostly the ORC system design is optimized using a genetic algorithm. They find that the proposed configuration could result in 1.5% fuel mass savings compared to the reference version of the Onera Dragon without the WHR system.

The system is modeled as follows: sizing of the electric power distribution and propulsion system is based on the takeoff mass and a fixed ratio between the takeoff propulsive power ( $\dot{W}_{TO}$ ) and the takeoff mass ( $m_{t,TO}$ ). This ratio is referred to as the power loading. The turboshaft engine performance is modeled using the *pyCycle* package available for *Python* [19]. The mass of the turboshaft engine is estimated using a regression based on data for existing turboshaft engines. The mass of the ORC unit is calculated by summing contributions from the radial inflow turbine, the volute, the ORC generator, the condenser, the Heat Recovery Steam Generator (HRSG), the pump, the working fluid, and the Balance of Plant. The Balance of Plant consists of miscellaneous supporting components needed for the functioning of the system. The two heat exchangers are modeled in relatively high detail, discretizing the hot and cold stream path in different control volumes based on the working fluid phase. Certain geometric design parameters, namely fin height, fin pitch, the louver angle, and the length of the flat tubes, are included in the set of optimization variables. The heat exchanger sizing outputs include the heat exchanger's mass, dimensions, and the pressure drop on both the hot and cold sides. The single-stage radial turbine is sized using an in-house design code. The mass of the generator is estimated using data regression, given the power output and the rotor surface velocity. The pump is simply modeled by an isentropic efficiency and a mass-specific power value. Finally, the Balance of Plant is estimated as 10% of the mass of the ORC unit.

Subsequently, Sinopoli et al. [9] looked at the sensitivity of the fuel burn to different working fluids. In their work, they no longer have a detailed model for the ORC turbine but rather use a correlation for the efficiency based on the turbine's pressure ratio and volume ratio. They found that compared to cyclopentane, ethanol as a working fluid could decrease the fuel mass by 0.3%. Toluene as a working fluid would increase the fuel mass by 0.6%. The authors mention that the main constraint on the performance is the size constraint on the heat exchangers. Although the authors consider the fuel burn variations negligible, they are significant enough to call for a careful selection of the working fluid in the design process of an airborne WHR system.

## 1.2. Research Objective and Question

From reviewing the literature presented above, it is concluded that to explore the potential of a new ORC based airborne WHR application, a simultaneous optimization of the working fluid and the process is needed due to the highly coupled nature of these two design aspects. Since such a simultaneous optimization has not yet been implemented in the *ARENA* framework, it is conceivable that the potential for fuel savings, e.g., for the Combined-Cycle Turboshaft (CC-TS) version of the Onera Dragon, is higher than currently estimated by Krempus et al. and Sinopoli et al. To determine if this is indeed the case, an integrated working fluid and component design optimization should be carried out. The research question is formulated as follows:

- **”Is there a pure fluid or fluid mixture that can be used as the working fluid for the ORC system used as bottoming unit of the turboshaft engines of the Onera Dragon aircraft concept, that will reduce the fuel consumption of the aircraft compared to using cyclopentane as a working fluid?”**
  - How much is the difference in fuel consumption compared to the uncertainty in the total fuel mass predicted by the model?

## 1.3. Report Outline

The report is structured as follows. First, in chapter 2, the relevant literature on integrated working fluid and process optimization is reviewed. Next, in chapter 3, the approach used to answer the research question is explained. Then, in chapter 4, the results are presented. Finally, the conclusions from the study are summarized in chapter 5.

# 2

## Literature Review on Integrated Working Fluid and Process Optimization

This chapter reviews the literature on integrated working fluid optimization for processes and, more specifically, ORC systems. This chapter is structured as follows. First, in section 2.1, heuristics-based working fluid selection is explained. Then, in section 2.2, some relevant working fluid property models are explained. Next, section 2.3 details a more recent development: computer-aided working fluid selection. Finally, in section 2.4, the existing literature on optimizing binary mixtures as working fluids is discussed.

### 2.1. The Heuristic Approach

Lampe et al. [27] mention that up to the time of writing (2014), the selection of a working fluid for an ORC-based system is done separately and before the process optimization. The choice of the working fluid is almost exclusively made by the designer using 'heuristic knowledge.' However, if the designer fails to sufficiently comprehend the interplay between working fluid properties and process variables, a suboptimal working fluid can be chosen. In subsection 2.1.1, the relation between a set of working fluid properties and the cycle performance is explained. Next, in subsection 2.1.2, intermediate working fluid selection criteria are explained.

A designer can make the choice of working fluid for ORC applications based on fluid thermodynamic properties and heuristic knowledge of their effect. Macchi and Astolfi [31] explain several considerations regarding the interplay between process and working fluid properties. Two types of heat sources are distinguished.

- **Constant temperature heat sources.** To maximize cycle efficiency for such a heat source, the saturated Rankine cycle is best suited. Then, the temperature profiles in the HRSG are close to parallel during the evaporation of the working fluid.
- **Variable temperature heat sources.** Airborne waste heat recovery falls into this category. In addition to cycle efficiency, the cycle's ability to cool down the heat source as much as possible is relevant. Contrary to the constant temperature heat source, multiple cycle configurations can be advantageous, such as superheated cycles, supercritical cycles, and multipressure cycles. Relevant properties of the working fluid are the critical temperature and the molecular complexity. For subcritical cycles with a high critical temperature, the cycle efficiency increases with increasing evaporation pressure. However, superheated cycles cannot fully use the available heat at high evaporation pressure. Saturated cycles can run at increased evaporation pressure while maintaining the ability to cool the heat source down. For supercritical cycles, the temperature profiles can be relatively well matched in the HRSG for pure fluids since the temperature continuously

increases during heat transfer. If the cycle is subcritical, pure fluids will show a nearly isothermal evaporation profile, which is likely not well matched with a variable temperature heat source. If a saturated cycle is used, a general rule is that the critical temperature should be close to the HRSG hotside entry temperature.

### 2.1.1. Key Fluid Properties Affecting the Cycle

Properties of the working fluid strongly influence the efficiency and design of the Rankine cycle. The most relevant factors include (I) molecular complexity, (II) critical temperature, and (III) molecular mass. These properties impact cycle performance, turbine design, and overall system efficiency. Next, the effects of each of the three properties shall be explained in more detail.

**Molecular mass:** A high molecular mass results in a small enthalpy drop during expansion and a low speed of sound, leading to higher Mach numbers in the turbine. The small enthalpy drop enables the use of a single or a few turbine stages. However, high Mach numbers necessitate specialized turbine design [31, p. 182].

**Molecular complexity:** Increasing molecular complexity necessitates a recuperator to maintain efficiency, as vapor desuperheating begins at a relatively high temperature. Complex molecules exhibit a larger volume ratio during expansion for a given pressure ratio. This leads to high flaring angles in the turbine. High flaring angles may cause flow separation and pose construction challenges. However, an advantage of complex molecules is that expansion occurs without any condensation, preserving turbine lifetime [31, p. 182].

**Critical point:** For constant evaporation and condensation temperatures and a saturated cycle, a higher critical temperature increases pressure and volume ratios. A high critical temperature also leads to a greater condenser volume flow rate, raising system size and cost. For low power capacity applications, increasing turbine volume flow enhances efficiency. Furthermore, a higher critical temperature reduces condensation pressure for a given condensation temperature [31, pp. 182–183].

### 2.1.2. Additional Relevant Fluid Properties

Different studies have optimized the working fluid for an ORC system for various objectives. Broadly speaking, the primary objective for a land-based powerplant is minimizing the Levelized Cost of Energy (LCOE). For airborne power generation, the primary objective is to minimize the mission fuel mass. However, this assumes the cost of the equipment remains within reasonable limits. In a heuristic working fluid selection procedure, objectives for molecular properties as a proxy for thermodynamic performance or system cost can include [35]:

- **High density** enables compact heat exchanger design.
- **Low liquid heat capacity** for better temperature profile matching.
- **Low viscosity** to minimize pressure loss in components.
- **High thermal conductivity** for efficient heat transfer and/or compact heat exchangers.
- **Sufficiently low melting point temperature.**
- **Sufficiently high critical temperature.**

Other requirements include a sufficiently low Ozone Depletion Potential (ODP), Global Warming Potential (GWP), toxicity, and flammability. Another constraint that might be included is that the condensation pressure is above atmospheric pressure to avoid air entering and forming an explosive mixture inside the system.

Macchi and Astolfi [31] mention two additional requirements to keep in mind, namely, compatibility with materials and commercial availability at a reasonable cost, although the latter is redundant if already included in determining the LCOE.

A key consideration is that the working fluid's maximum operational temperature must remain low enough to prevent decomposition-related issues. Macchi and Astolfi [31, p. 179] suggest a cycle temperature limit of approximately 350 – 400°C. Fluid decomposition can cause fouling buildup on heat exchanger surfaces, turbine damage, and unfavorable changes in thermodynamic properties.

## 2.2. Fluid Property Models

Some working fluid property models will be discussed before proceeding to the literature review on computer-aided fluid optimization methods. This section will briefly explain the Statistical Associating Fluid Theory (SAFT) Equation of State (EOS), the Group Contribution Method (GCM), the role of the Quantitative Structure Property Relationship (QSPR), as well as how transport properties of fluids can be predicted.

### Statistical Associating Fluid Theory

An EOS relates different fluid or gas state properties. Various EOS have been developed for different purposes and levels of fidelity. The current work uses the Perturbed Chain (PC)-SAFT EOS. A brief background and description of PC-SAFT is given in this subsection. The foundation of PC-SAFT was laid in the 1970s with perturbed hard-chain theory [2, 11]. This theory was first improved to account for polar and associating interactions, such as hydrogen bonding [53, 54, 55, 56], and was later further extended for modeling mixtures [3, 4]. For this mixture extension and its successors, the term SAFT was introduced. Expanding upon SAFT, Gross and Sadowski [18, 17] developed the PC-SAFT EOS by deriving an expression for the dispersion term, where molecules are modeled as chains of spheres. A SAFT EOS predicts the residual Helmholtz energy by summing different contributions, including the hard-chain system, dispersion attractions (e.g., London dispersion forces), and associating interactions. When combined with the Helmholtz energy of the ideal gas, thermodynamic quantities of interest are obtained through partial derivatives of the Helmholtz energy [31]. The parameters of the PC-SAFT EOS are as follows:

- $m$  - number of segments in a chain
- $\sigma$  - diameter of the segments
- $\epsilon_k$  - the dispersion energy of interaction between segments
- $\mu$  - dipole moment (0 for non-polar molecules)
- Associating sites (for example, hydrogen bonds)
  - $\epsilon^{A_i B_i}$  - Associating energy
  - $\kappa^{A_i B_i}$  - Associating volume

For binary mixtures, interactions between the two components are modeled with cross-interaction parameters like  $\sigma_{ij}$  and  $\epsilon_{ij}$ , which are the arithmetic mean and the geometric mean of the pure component  $\sigma$  and  $\epsilon_k$  values respectively [30]. The  $\epsilon_{ij}$  value can be corrected with the factor  $k_{ij}$  as can be seen in Equation 2.1. A graphical illustration of the first four parameters is shown in Figure 2.1.  $m$  thus represents the number of spherical segments that form the chain.  $\sigma$  is the diameter of each sphere,  $\epsilon_k$  is the dispersion energy between two molecules. The PC-SAFT parameters for a substance can be calculated from experimental vapor pressure and liquid density data using a regression. This is, for example, done by Esper et al. [14] for a database of 1842 fluids. This includes associating fluids, namely fluids with associating sites. As mentioned, a property of SAFT is that it is physically based. This is beneficial for integrated working fluid optimization. If the fluid model were not physically based, there would not be a straightforward approach to identify a real fluid from optimized fluid model (EOS) parameters.

$$\epsilon_{ij} = \sqrt{\epsilon_i \epsilon_j} (1 - k_{ij}) \quad (2.1)$$

### Group Contribution Methods

The GCM can be used to predict the properties of fluids described by the functional groups that the molecule consists of. A functional group is a (generally small) subset of the atoms comprising a molecule bonded in a specified manner. The division of a molecule into functional groups is done so that they can be used to predict chemical properties. Joback and Reid describe the method [23]. A method to determine the PC-SAFT parameters from the group contributions is described by Sauer et al. [46]. The reason that PC-SAFT parameters can, in fact, be predicted from group contributions is that it is a physics-based model.

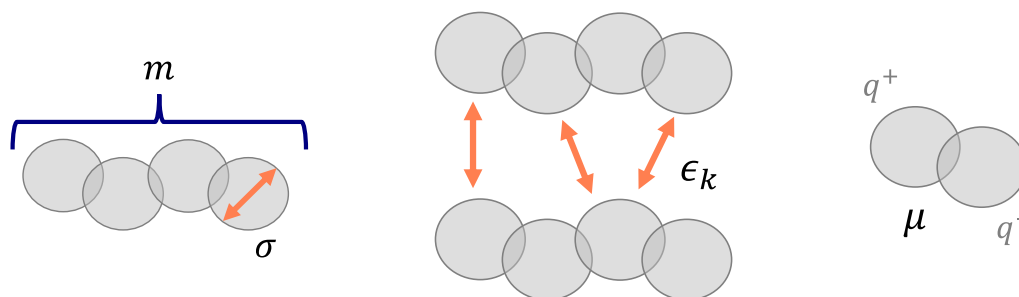


**Figure 2.1:** Illustration of the meaning of the (polar) PC-SAFT parameters.  $m$  is the number of spheres,  $\sigma$  is the sphere diameter,  $\epsilon_k$  represents the dispersion attraction between chains (molecules) and  $\mu$  represents dipole-dipole interaction.

GCMs are divided into homosegmented and heterosegmented variants. The homosegmented version models molecules without taking into account the connectivity or spatial orientation of the different segments. The model loses some fidelity during an averaging step. This is the case because the model consists of identical segments. The heterosegmented version, on the other hand, does account for the connectivity of the different groups. Also, as Sauer et al. noted, '(...) the molecular model of a heterosegmented GC approach consists of nonidentical segments.' This leads to a more accurate representation of the molecule [46]. Unsurprisingly, the heterosegmented version is computationally more expensive than the homosegmented one. For mixtures, the binary component/component interaction parameter  $k_{ij}$  (see Equation 2.1) can be found using a sum rule based on the number of groups  $n_{i,\alpha}$  and the binary group/group interaction parameters  $k_{\alpha\beta}$  [42].

### Predicting Additional Fluid Properties

As explained by Katritzky et al. [24, p. 279], a QSPR is a mathematical relationship between a property and one or more descriptive parameters (descriptors) related to the structure of the molecule. The first usage of a QSPR in an integrated process-fluid optimization was performed by Stavrou [30]. The application considered by Stavrou is a solvent for CO<sub>2</sub> capture where the molar mass and ideal gas heat capacity of the solvent are estimated based on the PC-SAFT parameters as descriptors. Once again, such a QSPR is enabled by the property of PC-SAFT that it is a physically based model. For ORC applications, viscosity and thermal conductivity are relevant transport properties. Schilling et al. [47, p. 19] explain that these properties can be estimated using Rosenfeld's entropy scaling. The residual entropy, which is then needed, can be found using the PC-SAFT EOS. The entropy scaling approach requires substance-specific model parameters that can be calculated using a group contribution method [29]. However, for pseudo-fluids (a modeled fluid defined by its PC-SAFT parameters only, not necessarily corresponding to a real fluid), entropy scaling is not an option. An alternative approach to estimating the viscosity and thermal conductivity for pseudo-fluids is the method by Chung et al. [5].

## 2.3. Computer Aided Working Fluid Optimization

By selecting a working fluid from a small set using heuristic guidelines, a suboptimal working fluid is likely chosen. A rigorous approach to finding the best working fluid would be to repeat the system optimization for every known substance. However, this is not feasible due to the extreme computational cost. To overcome this limitation, Bardow et al. [1] developed a simultaneous process and working fluid optimization method. An EOS is used to model the working fluid. Then, as an initial step, the parameters of this EOS are optimized as continuous design variables. Treating the substance-dependent EOS parameters as continuous design variables allows them to be efficiently optimized by an optimization algorithm. Any point in the N-dimensional space of the EOS parameters that does not correspond to a real fluid is called a pseudo-fluid. An illustration of a pseudo-fluid point and real fluid points in the PC-SAFT parameter space is given in Figure 2.2. The performance of the optimal pseudo-fluid is referred to as the target. Once the target is established, the next step is to identify the real fluid that most closely approximates the target; this process is called structure-mapping. The complete method is called Continuous-Molecular Targeting (CoMT)-Computer Aided Molecular Design (CAMD), where the CoMT part refers to the idea that the EOS parameters are treated as continuous variables. This method is not limited to ORC applications; any (industrial) process where the design and subsequent

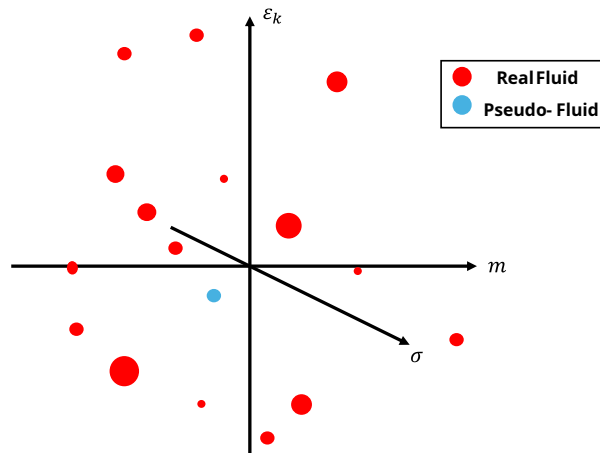


**Figure 2.2:** Illustration of a pseudo-fluid point and real fluid points in the 3D space of PC-SAFT parameter for non-polar, non-associating substances.

performance of the process depend on properties of the working fluid can benefit from an integrated working fluid optimization.

Early work on a fluid optimization method tailored to ORC systems was done by Papadopoulos et al. [35]. They proposed adapting the group-based CAMD methods already in use for designing polymers, refrigerants, and solvents to improve the process of selecting a working fluid for ORC applications. Their approach includes multiple steps. First, a Pareto front for minimizing or maximizing a set of molecular properties is produced. Subsequently, the fluids on the Pareto front are separated into groups by similar chemical structure or process performance. A well-performing substance is selected from each group to evaluate its economic performance for an optimized process using the Peng-Robinson (PR)-EOS to model the working fluid. While this approach does expand the design space of the working fluid, its use of intermediate design objectives based on fluid properties still suffers from some of the problems of a heuristic working fluid selection.

Lampe et al. used the CoMT-CAMD method to optimize the working fluid of an ORC system [27]. A second-order Taylor approximation with respect to the PC-SAFT parameters is made for the objective function around the target. Subsequently, the objective function can be evaluated for real fluids in the neighborhood of the pseudo-fluid using the Taylor approximation. The objective function values estimated using the Taylor approximation are used to make a ranking of real fluids in the neighbourhood.

This process can be refined using an adaptive structure mapping where the error between an evaluation of the objective function for the real fluid and the value estimated using the second-order Taylor approximation is evaluated. If the error exceeds a specified threshold, a Taylor approximation around the real fluid is combined with the Taylor approximation around the target.

Schilling et al. [48] proposed an improved methodology, where they avoid the 2-staged approach of Lampe et al. and use an optimization algorithm that can accept discrete variables, such that the two steps are combined. This is made possible by the parametrization of the working fluid molecular structure using functional groups where group occurrences are discrete design variables. The working fluid properties are then evaluated using the GCM as illustrated in Figure 2.2. This approach is beneficial because it guarantees an accurate molar mass estimate since it is evaluated directly from the molecular structure instead of being estimated by a QSPR. Additionally, a larger design space for real fluids is enabled since a database needs to be only for the groups. Thus, any molecule that can be constructed using the groups does not need to be present in a database for it to be constructed by this method.

The 1-stage CoMT-CAMD approach is an improvement over the 2-stage version from Lampe et al. by avoiding additional uncertainty introduced in the structure-mapping step. A drawback is that pure component parameters estimated using the homosegmented GCM introduce some inaccuracy, leading, on average, to an underestimation of the objective by 0.8% in the work by Schilling et al. Isomers, using fitted data, could have a different objective function value by up to 0.4%. These differences are

insignificant for the preliminary design of the system. The identified optimal fluid is excluded from the design space for a subsequent re-evaluation of the optimization problem. This is referred to as 'integer-cutting.' The idea is that a ranking of multiple well-performing fluids is obtained. Having a ranking of multiple fluids instead of a single fluid is beneficial as uncertainties may affect the true ranking. Also, well-performing alternatives are still available if any of the obtained fluids is not usable due to toxicity or other limitations.

## 2.4. Working Fluid Mixtures

Matching the temperature glide (temperature difference between the bubble point temperature and dew point temperature of a fluid for a specified pressure) of the working fluid with that of the heat source and sink enables the minimization of irreversibilities that arise during heat transfer. This enables a more efficient cycle. Since zeotropic mixtures feature a temperature glide during condensation and, if the cycle is subcritical, evaporation, this property can be exploited to minimize exergy destruction—something that cannot be achieved with pure fluids, which do not have a temperature glide during phase change.

Macchi and Astolfi [31, p. 183] note that mixtures are associated with increased heat exchanger size and cost. This is a direct consequence of the decreased temperature difference since that entails an increased heat transfer area for the same heat duty. Also, heat transfer coefficients are lower for mixtures compared to their pure components. The requirement that a working fluid does not degrade at the peak temperature reached during operation is relatively easily verified for pure components. For mixtures, on the other hand, little consensus exists about how to predict thermal stability. Krempus et al. assume in ref. [26, p. 5] that thermal degradation of the mixture does not occur at a temperature lower than the lowest decomposition temperature of the individual components.

Papadopoulos et al. [36] developed a method to design optimal binary mixtures for ORC applications. Additionally, they developed a sensitivity analysis to identify which fluid properties have the strongest influence on the optimization objective. This is useful to determine if the used property model is sufficiently accurate to deliver an accurate result for the optimization. Furthermore, they integrate the sensitivity analysis into the decision-making process by, when possible, selecting mixtures with relatively little sensitivity to fluid properties with a high uncertainty. The proposed method starts by relaxing the structural feasibility constraint on component B of the mixture. It is explained that this is done to avoid losing high-performance individual components from the Pareto front. In the second stage, component B is optimized for parts of the Pareto front where the B component is infeasible.

Schilling et al. [47] note that the approach by Papadopoulos et al. highlights the advantages of integrating process and mixture design. However, it has limitations, such as relying on a thermodynamic property model that fails to accurately predict the properties of non-ideal mixtures. Additionally, optimization is performed only for maximum power output. To address these limitations, Schilling et al. propose two improvements: (I) '[integrating] a consistent thermodynamic model with strong prediction power for mixtures,' namely PC-SAFT, and (II) '[integrating] detailed models for equipment sizing based on the transport properties of the mixture.' Building on their earlier 1-stage CoMT-CAMD method for pure fluids, Schilling introduces a second component and a mixture fraction. Unlike Papadopoulos [36], they impose feasibility constraints directly for both components, believing that their optimization algorithm can identify the optima without initially relaxing feasibility constraints for the second component. Another key difference is that while Papadopoulos did not consider transport properties, Schilling incorporates Rosenfeld's entropy scaling to predict viscosity and thermal conductivity. Their study shows that using working fluid mixtures in an ORC system for power generation from hot wastewater can increase net power output by up to 7% compared to an optimized pure working fluid, depending on the temperature glide of the cooling water. However, they observe a reduced economic benefit.

Krempus et al. [26] researched the performance benefit of working fluid mixtures for ORC bottoming units combined with land-based gas turbine powerplants. 26 working fluids (meaning 325 possible mixture combinations) were tested. They did not find efficiency benefits for any mixture. They do mention that certain fluids and mixtures can enable a more compact and low-cost turbine.

# 3

## Methodology

As implied by the research question given in section 1.2, it is not yet established if cyclopentane is an optimal working fluid to use in the ORC waste heat recovery system for the turboshaft engines of the Onera Dragon aircraft. To determine this, the set of process parameters previously optimized by Sinopoli et al. is extended with working fluid parameters for this test case. Integrated working fluid optimizations of the power generation system are then done to evaluate whether the objective function value can be significantly better than the optimum value found for the WHR unit using cyclopentane.

This chapter explains the system model, the fluid optimization approach, and the optimization details. First, in section 3.1, the aircraft and its propulsion system are detailed. Then, in section 3.2, the approach for optimizing the working fluid is explained. Finally, in section 3.3, details about the optimization process are laid out.

### 3.1. Aircraft and Propulsion System Model

In this section, the original aircraft concept from Schmollgruber et al. [49] and the adaption proposed by Krempeus et al. [7] to integrate two ORC WHR systems are described in subsection 3.1.1. Then, in subsection 3.1.2, some further details about the Combined Cycle Power Unit (CCPU) configuration and model details relevant to the current work are given.

#### 3.1.1. Aircraft Overview

The aircraft model that shall be considered in this work is the Onera Dragon turboelectric aircraft concept (also described in section 1.1). An illustration of this aircraft can be seen in Figure 3.1. The Top-Level Aircraft Requirements (TLARs) of this concept are shown in Table 3.1.

The aircraft utilizes distributed electric propulsion for nearly all of its required thrust. Depending on the design specifics, a minor fraction of the required thrust may be supplemented by ram air ducts or the turboshaft exhaust flow. Distributed electric propulsion, characterized by a high total air mass flow, facilitates a low fan pressure ratio, which is advantageous for propulsive efficiency. Additionally, the distributed propulsion system can positively influence wing performance [8].

The EDFs are modeled with relatively low detail. The product of jet generation and propulsive efficiency for the EDFs is assumed to be a constant 86% during cruise. The electric power is supplied by two CCPU's mounted on the tail. The fuel consumption presented in this study corresponds to a mission of 5100 km. To account for diversion, loitering, contingencies, and additional energy requirements for climbing to cruise altitude, additional distances are added. The final equivalent range amounts to 6611 km.

The total fuel mass is determined using the Breguet equation, under the assumption of a constant Lift-to-Drag Ratio ( $L/D$ ) and Power Specific Fuel Consumption (PSFC) throughout the flight. The aircraft drag is evaluated using the three-term drag polar shown in 3.1, where  $C_{D,\min} = 0.0183$ ,  $K_L = 0.0937$ , and  $C_{L,\min} = 0.16$ . The latter two parameters are estimated based on the cruise lift and drag coefficients

of the Onera Dragon, while  $C_{D,\min}$  is determined using the method proposed by Obert [33]. A constant  $C_L$  is assumed, selected to maximize L/D according to the drag polar.

The mass of the power delivery (inverters, cables, et cetera.) and propulsion system (EDFs) is estimated based on the power capacity estimated for the takeoff condition. The maximum performance requirement is translated into a power loading value, meaning a specified propulsive power value per unit of takeoff weight. The required propulsive power is obtained by multiplying the takeoff mass with the power loading value. The system's mass is estimated using mass-specific power values for each component. This implies assuming a linear relation between the mass of the component and the maximum power transferred by the component.

$$C_D = C_{D,\min} + K_L(C_L - C_{L,\min})^2 \quad (3.1)$$

### 3.1.2. Combined Cycle Power Unit

Each CCPU consists of a turboshaft engine with an ORC bottoming cycle. The CCPU system architecture is shown in Figure 3.2. The turboshaft engine consists of a twin-spool gas generator and an Free Power Turbine (FPT) that drives two generators for redundancy. The ORC unit also produces electrical power using a turbogenerator. The turboshaft engine will also be referred to as the engine for brevity. A schematic of a CCPU is shown in Figure 3.3. As can be seen, the exhaust gas exiting the FPT passes through a heat exchanger: the HRSG (labeled 'Evaporator' in the schematic). The ORC working fluid is then expanded through a radial inflow turbine. The efficiency of this turbine is estimated in the current work using the approach also used for ref. [9]. The condensers are mounted in two ram-air ducts, one above and one below the engine. After condensing, the liquid working fluid is pumped back to  $p_{max,orc}$ , after which the cycle continues in the HRSG.

Next, some important points concerning the powertrain model are described. The impact of the net force of the ram air duct on aircraft fuel consumption is accounted for by adapting the zero-lift drag. Note that the net force of the ram air duct does not take into account external nacelle drag. The ram air duct intake drag is evaluated using the method from ref. [13]. As for the design point of the engine, a single design point is considered, namely the cruise condition at the flying weight  $m_{cr}$  defined in Equation 3.13. The engine's mass is estimated with Equation 3.2 based on the corrected air mass flow rate at the compressor inlet in the cruise condition. Krempus et al. fitted Equation 3.2 to data of existing turboshaft engines [7]. In Equation 3.2 and Equation 3.3, The mass of the engine ( $m_{tts}$ ) is in kg, and  $\dot{m}_{2,\text{red}}$  is calculated using Equation 3.3.  $T_{t,2}$  is in K,  $p_{t,2}$  is in bar and  $\dot{m}_2$  is in kg/s.

$$m_{tts} = 21.56 \cdot \dot{m}_{2,\text{red}} + 85 \quad (3.2)$$

$$\dot{m}_{2,\text{red}} = \dot{m}_2 \cdot \sqrt{\frac{T_{t,2}}{288.15}} \cdot \frac{1.01325}{p_{t,2}} \quad (3.3)$$

The following definitions are used in the model. The chemical power of the fuel flow ( $\dot{W}_{\text{chem}}$ ) is given by Equation 3.4, where  $\dot{m}_{\text{fuel}}$  represents the fuel mass flow, and LHV is the lower heating value of the fuel (43 MJ/kg). The electric power produced by a single ORC turbine ( $\dot{W}_{\text{net,ORCT}}$ ) is defined in Equation 3.5. Here,  $\dot{W}_{\text{gross,ORCT}}$  denotes the power delivered to the turbogenerator shaft by the ORC turbine rotor. The efficiency of power production by the CCPU ( $\eta_{\text{net,ccpu}}$ ) is given in Equation 3.6. The electric power generated by a single CCPU ( $\dot{W}_{\text{net,ccpu}}$ ) is defined in Equation 3.7, where  $\dot{W}_{\text{net,pump}}$  represents the shaft power demand of the pump. Additionally,  $\eta_{\text{mech,pump}}$  and  $\eta_{\text{mot,pump}}$  correspond to the efficiency of the shaft connecting the pump motor to the pump rotor and the efficiency of the electric motor driving the pump, respectively. The electric power produced by a single turboshaft engine ( $\dot{W}_{\text{net,pu}}$ ) is given by Equation 3.8. The efficiency of the ORC system ( $\eta_{\text{net,orc}}$ ) is defined in Equation 3.9, while the net power output of a single ORC unit ( $\dot{W}_{\text{net,orc}}$ ) is given in Equation 3.10. The transmission efficiency between the electric output power of any of the generators and the shaft power driving the EDFs ( $\eta_{\text{trans}}$ ) is described in Equation 3.11, where  $\eta_{\text{acdc}}$ ,  $\eta_{\text{pmu}}$ , and  $\eta_{\text{dcac}}$  represent the efficiencies of the AC-to-DC inverter, the power management unit, and the DC-to-AC inverter, respectively. Additionally,  $\eta_{\text{mot,EDF}}$  denotes the efficiency of the electric motors of the EDFs. The electric power demand for propulsion ( $\dot{W}_{\text{cr}}$ ) is evaluated in Equation 3.12. The cruise mass ( $m_{\text{cr}}$ ), used as the reference aircraft

mass for assessing cruise performance, is defined in Equation 3.13. Here,  $m_{\text{fuel,cr}}$  represents the total fuel consumption for a nominal mission, excluding diversion or loitering. The efficiency of propulsive power production ( $\eta_{\text{pp,core}}$ ) is defined as shown in Equation 3.14. The efficiency of propulsive power production by the ram air ducts together with the EDFs is defined in Equation 3.15. The sum of  $\eta_{\text{pp,core}}$  and  $\eta_{\text{pp,EDF,RAD}}$  is the total efficiency ( $\eta_{\text{total}}$ ).

$$\dot{W}_{\text{chem}} = \dot{m}_{\text{fuel}} \cdot \text{LHV} \quad (3.4)$$

$$\dot{W}_{\text{net,ORCT}} = \dot{W}_{\text{gross,ORCT}} \cdot \eta_{\text{mech,ORCT}} \cdot \eta_{\text{gen,ORCT}} \quad (3.5)$$

$$\eta_{\text{net,ccpu}} = \frac{\dot{W}_{\text{net,ccpu}}}{\dot{W}_{\text{chem}}} \quad (3.6)$$

$$\dot{W}_{\text{net,ccpu}} = \dot{W}_{\text{net,pu}} + \dot{W}_{\text{net,ORCT}} - \frac{\dot{W}_{\text{net,pump}}}{\eta_{\text{mech,pump}} \cdot \eta_{\text{mot,pump}}} \quad (3.7)$$

$$\dot{W}_{\text{net,pu}} = \dot{W}_{\text{gross,pu}} \cdot \eta_{\text{mech,pu}} \cdot \eta_{\text{gen,pu}} \quad (3.8)$$

$$\eta_{\text{net,orc}} = \frac{\dot{W}_{\text{net,orc}}}{Q_{\text{evap}}} \quad (3.9)$$

$$\dot{W}_{\text{net,orc}} = \dot{W}_{\text{net,ORCT}} - \frac{\dot{W}_{\text{net,pump}}}{\eta_{\text{mech,pump}} \cdot \eta_{\text{mot,pump}}} \quad (3.10)$$

$$\eta_{\text{trans}} = \eta_{\text{acdc}} \cdot \eta_{\text{pmu}} \cdot \eta_{\text{dcac}} \cdot \eta_{\text{mot,EDF}} \quad (3.11)$$

$$\dot{W}_{\text{cr}} = \frac{(D - 2 \cdot F_{\text{jet}}) \cdot V_{\infty}}{\eta_{\text{trans}} \cdot \eta_{\text{prop}}} \quad (3.12)$$

$$m_{\text{cr}} = \sqrt{m_{\text{t,TO}} \cdot (m_{\text{t,TO}} - m_{\text{fuel,cr}})} \quad (3.13)$$

$$\eta_{\text{pp,core}} = \frac{F_{\text{jet}} \cdot V_{\infty}}{\dot{W}_{\text{chem}}} \quad (3.14)$$

$$\eta_{\text{pp,EDF,RAD}} = \frac{4 \cdot V_{\infty} \cdot F_{\text{RAD}} + \dot{W}_{\text{net,ccpu}} \cdot \eta_{\text{mech,pump}} \cdot \eta_{\text{prop}}}{\dot{W}_{\text{chem}}} \quad (3.15)$$



**Figure 3.1:** Illustration of the ONERA Dragon aircraft [49]. Figure shows a version with more than 13 EDFs per wing.

**Table 3.1:** TLARs of the ONERA Dragon [49].

Parameter	Value
Design Range / km	5100
Passengers	150
Cruise Mach number	0.78
Design Payload / kg	13600

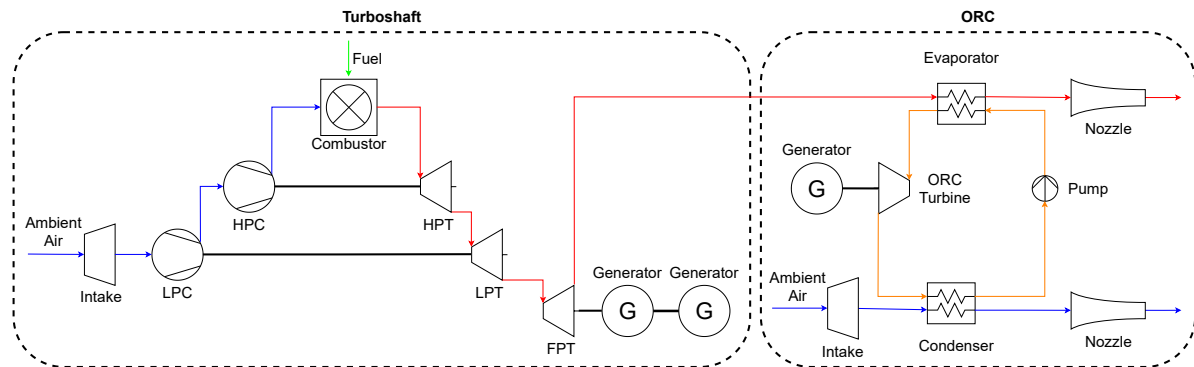


Figure 3.2: Process Flow Diagram of a CCPU [7].

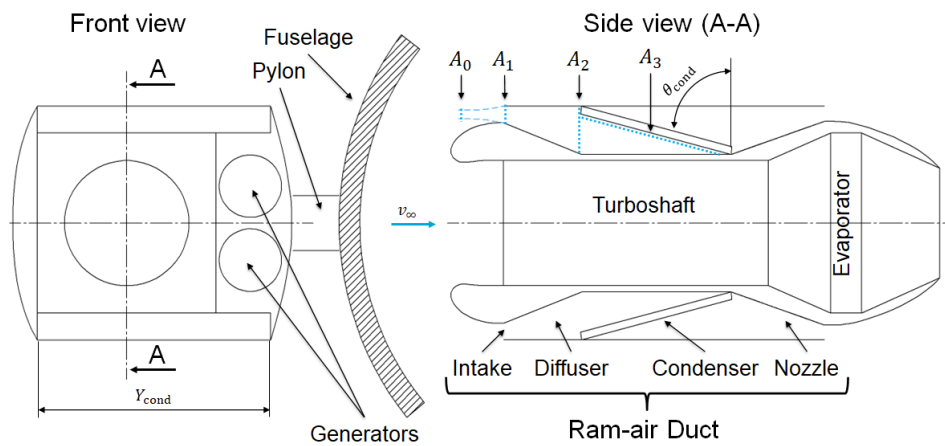
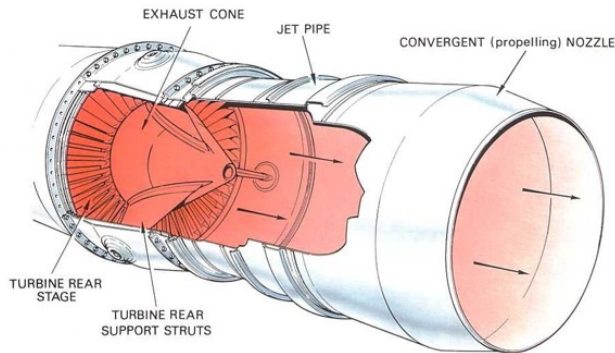


Figure 3.3: Schematic of a CCPU [7]. The X dimension of the condensers is the blue dotted line corresponding to A3 on the right side of the figure. The Y dimension of the HRSG (indicated in the figure as 'Evaporator') is defined similarly to that of the condenser in the spanwise direction.



**Figure 3.4:** Illustration of a generic aero-engine exhaust duct.<sup>1</sup>



**Figure 3.5:** Picture of a Bare Tube Bundle (BTB) heat exchanger.<sup>2</sup>

### Heat Exchanger Modeling

The heat exchangers are modeled and sized in this work using an in-house tool called *HeXacode*. The primary heat exchanger (the HRSG), which recovers heat from the exhaust gas, is a cross-counterflow Bare Tube Bundle heat exchanger. An image of a generic rectangular BTB is shown in Figure 3.5. An illustration of the BTB with relevant definitions is shown in Figure 3.7. As seen in Figure 3.3, it is mounted orthogonal to the centerline of the engine in the exhaust duct. An illustration of a generic aero-engine exhaust duct is shown in Figure 3.4. The section of the exhaust duct where the HRSG is integrated is square-shaped, with a side slightly larger than the core diameter. The longitudinal ( $x_l$ ) and transverse ( $x_t$ ) spacing of the tubes, as seen in the top right of Figure 3.7, are normalized with the outer diameter of the tubes: 1.8 mm. The top left part of the figure shows the cross-counterflow configuration. From previous works by Sinopoli et al. [9] and Krempus et al. [7], it is concluded that the optimum of both the transverse and longitudinal adimensional spacing of the HRSG tubes is independent of the other design variables that are considered. The values are fixed to 3 for the transverse spacing and 1.3 for the longitudinal one. 1.3 is slightly greater than 1.25, which is found in the works by Sinopoli et al. and Krempus et al. 1.25 is at the limit of the Heat Transfer Coefficient (HTC) correlation. 1.3 is chosen instead since it is expected that for this value, the accuracy of the HTC correlation is better.

Heat rejection is facilitated by a flat-tube microchannel condenser with louvered fins; see Figure 3.8 for an illustration. The condensers are mounted with a tilt angle to allow for a large frontal area without requiring a large flaring angle for the diffuser. A large flaring angle is detrimental to diffuser efficiency, leading to increased pressure loss. A large tilt angle for the condenser also causes additional pressure loss. This is estimated using a function fitted by Krempus et al. [7] to data from ref. [32]. The massflow ratio, representing the compression of the air streamtube before it enters the ram air duct, is one of the optimization variables ( $\xi$ ). The condenser microchannel width is added as a design variable for a more robust convergence by *HeXacode*. To use microchannel width as a design variable, a different version of *HeXacode* is required compared to the one used in previous works by Sinopoli et al. and Krempus et al. The performance estimations obtained with the two different versions of *HeXacode* are not identical. The initial version of *HeXacode* uses the correlation by Taler [52] for the HTC of single phase flow, while the newly adopted version uses the correlation by Gnielinski [16] by default. This results in different performance predictions, which will be highlighted again in section 4.1.

Moreover, the *HeXacode* package does not have a two-phase condensation HTC correlation for mixtures exhibiting a temperature glide. Such a correlation was developed by Deng et al. [10], and was implemented in *HeXacode* in this project. The implementation of this correlation is verified with the values predicted by Shah [51] for cyclopentane. It can be seen in Figure 3.6 that the agreement is decent. Unless indicated otherwise, Deng's correlation is used for all simulations of this work. It is also used for pure fluids, such that  $f_1$  results can be compared between mixture and pure fluids.

<sup>1</sup><http://aeromodelbasic.blogspot.com/2012/01/exhaust-system-exhaust-gas-flow.html>, accessed 22-04-2025

<sup>2</sup><https://emergentcoils.com/pages/mammoth-coil-replacements>, accessed 22-04-2025

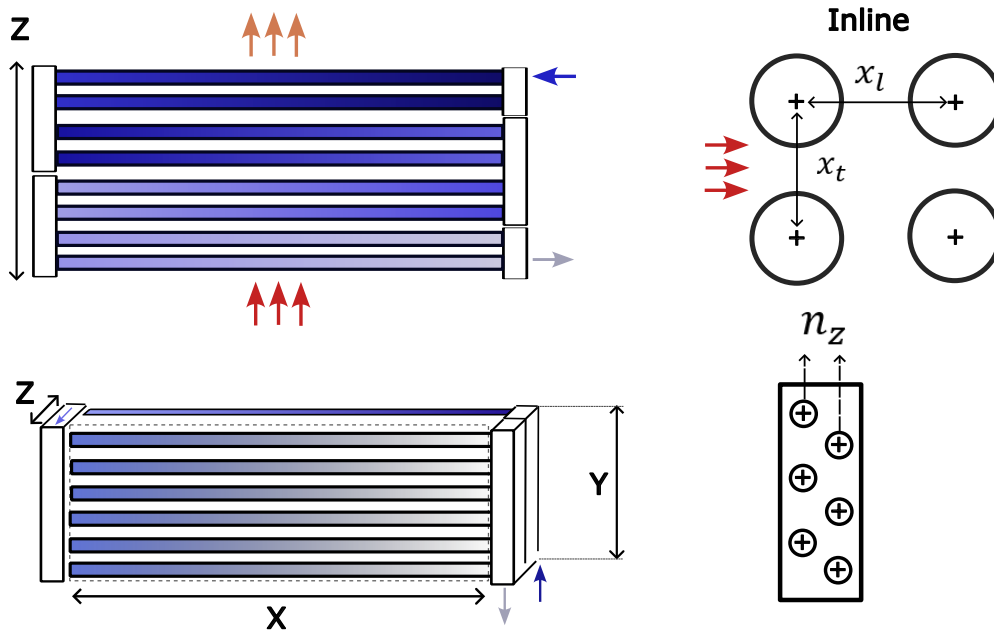


Figure 3.7: Illustration of a cross-counterflow bare tube bundle [7].

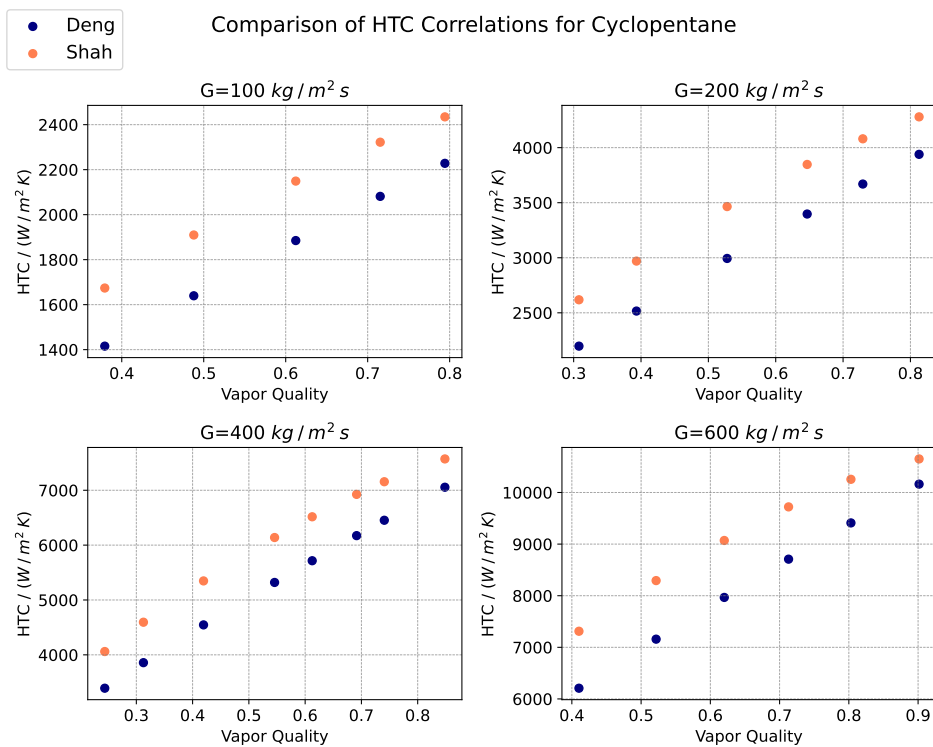


Figure 3.6: Comparison of HTC correlations by Deng et al. [10] and Shah [51] for cyclopentane.

### Engine and Turbomachinery Performance

The turboshaft engines are modeled using a package called *pyCycle* for *Python* [19]. The polytropic efficiency of axial compressors and turbines are predicted based on engine Entry Into Service (EIS),

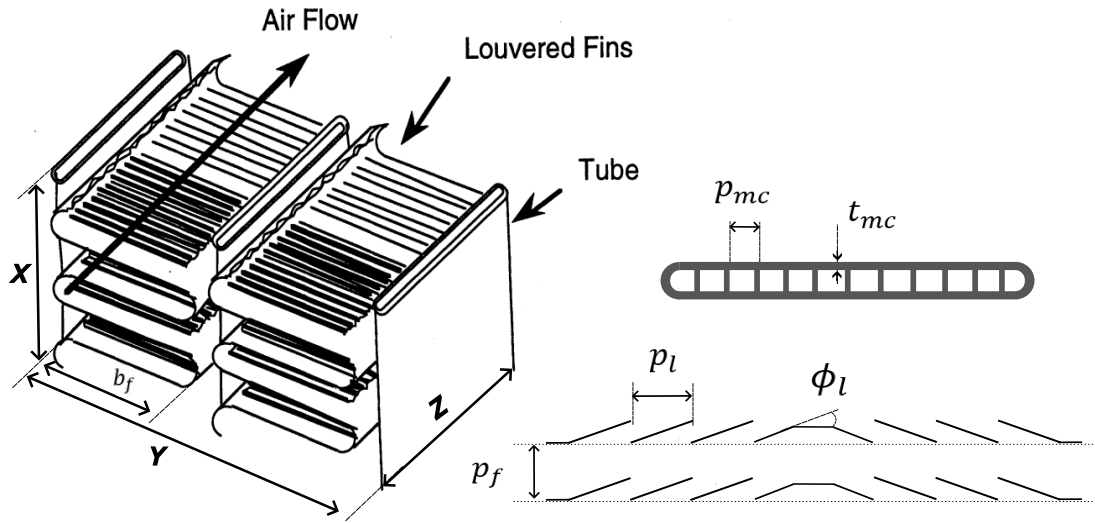


Figure 3.8: Illustration of a flat-tube microchannel condenser with louvered fins [7].

duty coefficient, and massflow using the correlations from ref. [44]. The cooling air demand is estimated using the model of Gauntner [15]. The OPR in the cruise condition is set to 45. From analysis by Kremus et al. [7], this is found to be the highest possible OPR in cruise while ensuring the compressor exit temperature does not exceed 950 K in the takeoff condition. This temperature limit is due to material considerations. While the OPR cannot currently be optimized above 45, it is found from two investigative optimizations that the optimal OPR for cyclopentane, if unconstrained, would be 55.3 while for a pseudo-fluid it would be 53.7, assuming the ratio of  $\Pi_{LPC}$  to  $\Pi_{HPC}$  remains constant. Since this is above 45, the OPR is not adopted as an additional design variable. The duty coefficients from Sinopoli et al. are adopted initially. Since the effect of the duty coefficients on the mass and size of the engine is not modeled, optimizing the duty coefficients would likely not result in a realistic design and instead tend to the highest possible turbomachinery efficiency regardless of the effect this would have on the sizing of the components. Similarly, for the choice of  $\Pi_{LPC}$  and  $\Pi_{HPC}$ , if just taking into account the efficiency correlation, an optimization algorithm would tend to maximize the compression in the most efficient of the two. The problem, then, would be that the effect of shaft speed on the turbomachinery design is not considered. For the reasons mentioned, the input parameter values for the engine design are left unchanged compared to the previous work by Sinopoli et al. [9]. As shall be highlighted later on in section 4.1, there is some discrepancy in the engine design specifications between the previous works. However, it is not believed that the engine design affects the trends of the ORC system performance and the identification of the optimal working fluid.

### 3.2. Working Fluid Optimization Approach

The PC-SAFT equation of state, together with  $c_p^{ig}$  are used to obtain state and caloric properties. The (polar) PC-SAFT equation implemented in *FluidProp* [6] is used to model the working fluid of the ORC unit. Not all substance properties can be predicted using the PC-SAFT EOS. The method from Chung is used for predicting viscosity and thermal conductivity [5]. The method by Sastri and Rao [45] is used for the surface tension. The molecular mass and  $c_p^{ig}$  are estimated using the QSPRs presented in ref. [30]. The critical point, which is needed for the method from Chung, is predicted using the PC-SAFT EOS. Also, the normal boiling point, which is required for the method from Sastri and Rao, is calculated using the PC-SAFT EOS. It should be noted that different QSPR's are used for polar molecules than non-polar molecules. For optimizations with cyclopentane as a fixed working fluid, fluid properties from *CoolProp* are used instead.

### 3.2.1. Continuous-Molecular Targeting

In this work, the integrated working fluid optimization involves treating the PC-SAFT parameters as continuous design variables. This is the method that is indicated in the literature study (section 2.3) as CoMT. The goal of pseudo-fluid optimization here is to identify the upper performance limit of the ORC system that can be achieved through working fluid selection. Since two distinct QSPRs are used for polar and non-polar fluids, the optimization is performed twice: once for a non-polar pseudo-fluid and once for a polar pseudo-fluid. Optimization runs with different optimization seeds can converge to different PC-SAFT parameters. This results in a ranking of optima. The ranking might change when evaluating the real fluids associated with the optima (see subsection 3.2.2) or by considering additional criteria at a later stage.

The results from this step, the target, should indicate whether the improvement in the objective function relative to the cyclopentane baseline case justifies the effort of finding a real working fluid. Also, a target can help judge whether or not a real fluid is likely to be a local optimum that is far from the global optimum. Furthermore, by simultaneously optimizing two pseudo-fluid components and the mixture fraction, it can be investigated if binary mixtures have the potential to allow a greater improvement of the objective function than a pure fluid. Similar to the pure fluids, the pseudo-fluid mixture optimizations need to be repeated for mixtures of non-polar pseudo-fluid mixtures and polar pseudo-fluid mixtures. For pseudo-fluid mixtures,  $k_{ij}$  values (see Equation 2.1) are set to zero.

### 3.2.2. Finding a Real Fluid

If the integrated working fluid optimization using the CoMT approach shows a substantial objective function improvement compared to the baseline working fluid, a CAMD method is used to identify an optimal real working fluid. In this work, the CAMD approach is to ensure that the PC-SAFT parameters of the pseudo-fluid closely match those of a real fluid through a bi-objective optimization. The additional objective of this optimization ( $f_2$ ) is to minimize the distance between the PC-SAFT parameters of the pseudo-fluid and those of the Closest Neighbouring Real Fluid (CNRF).

To define the CNRF, an appropriate distance metric must be established. This is done using normalized PC-SAFT parameters, as defined in Equation 3.17, for the PC-SAFT parameter vector  $\mathbf{q}$  in Equation 3.16. The normalization process involves scaling the PC-SAFT parameters using the mid-points of their respective bounds. This approach prevents biases that could arise due to differences in the orders of magnitude among the PC-SAFT parameters.

The CNRF is then identified as the real fluid, from a set of  $N_{\text{rf}}$  fluids, for which the Euclidean distance  $\|\bar{\mathbf{q}}^{\text{pf}} - \bar{\mathbf{q}}^{\text{rf},i}\|$  is the lowest value out of all  $i \in N_{\text{rf}}$ . In other words, the CNRF is the real fluid whose normalized PC-SAFT parameters are closest to those of the pseudo-fluid.

The objective function  $f_2$  is defined in Equation 3.18, incorporating the non-dimensionalized PC-SAFT parameters from Equation 3.17. In these equations,  $\mathbf{q}$  represents a PC-SAFT parameter vector corresponding to either a real fluid or a pseudo-fluid (as defined in Equation 3.16), with subscripts  $\text{rf}$  and  $\text{pf}$  denoting real fluids and pseudo-fluids, respectively. Additionally,  $\mu$  is set to zero for non-polar fluids.

The set  $N_{\text{rf}}$  includes integer indices corresponding to real fluids in the database compiled by Esper et al. [14]. Some fluids are filtered out of the database; this is explained in more detail in subsection 3.2.3. This database contains various substances, including fluid families that are currently considered suitable for ORC applications. The fluid families are listed in Table 3.2.

The result of the bi-objective optimization is a Pareto front comprising  $f_1$ - $f_2$  combinations. For the points on this front, no other solution was found where either  $f_1$  or  $f_2$  can be improved without worsening the other. The Pareto front will thus contain two types of optima: pseudo-fluid optima, where  $f_2$  has a non-negligible value, and real fluid optima, where  $f_2$  is sufficiently close to zero. The upper limit for  $f_2$  ensuring that the properties of the pseudo-fluid relevant for its performance in the ORC system are nearly identical to the properties of the CNRF cannot be predicted a priori with certainty. In this work, a threshold of  $1e-3$  is used.

If the above-mentioned approach does not deliver satisfying results, the fluid can be parameterized using the GCM in combination with an optimization algorithm capable of handling integer design variables. In this approach, the occurrences of the different groups under consideration are optimized by

the algorithm, which treats them as integer design variables.

While a fluid may be optimal in terms of enabling an improved  $f_1$  value compared to cyclopentane, there are numerous boundary conditions that need to be satisfied before the fluid can be seriously considered for usage in an airborne WHR system. Such considerations include toxicity, GWP, ODP, flammability, etc. While the evaluation of these properties is critical, no models for any of the mentioned criteria are adopted, meaning they cannot be taken into account by the optimization algorithm as a constraint.

$$\mathbf{q} = \begin{bmatrix} m \\ \sigma \\ \epsilon_k \\ \mu \end{bmatrix} \quad (3.16)$$

$$\bar{\mathbf{q}} = \begin{bmatrix} \frac{m}{m_{mp}} \\ \frac{\sigma}{\sigma_{mp}} \\ \frac{\epsilon_k}{\epsilon_{k,mp}} \\ \frac{\mu}{\mu_{mp}} \end{bmatrix} \quad (3.17)$$

$$f_2(\mathbf{q}^{pf}) = \min_{i \in N_{rf}} (\|\bar{\mathbf{q}}^{pf} - \bar{\mathbf{q}}^{rf,i}\|) \quad (3.18)$$

### 3.2.3. Fluid Database and Convex Hull

The lower limit found from the integrated working fluid optimization with the CoMT approach should be close to the real fluid global optimum. Put differently, the pseudo-fluid found from the CoMT step should ideally be in a region of the PC-SAFT parameter space where real fluids exist. A convex hull around a set of points corresponding to real fluids in the PC-SAFT parameter space is used as an inequality constraint for this purpose. The set of points corresponding to real fluids is obtained from a fluid database from Esper et al. [14]. However, fluid families for which the molar mass is poorly predicted by the QSPR are excluded. Examples of fluid families with good, mediocre, and poor molar mass prediction are included in Appendix A. Table 3.2 shows which fluid families are included in the definition of the convex hull. This is not only relevant for the bi-objective optimization but also for the pseudo-fluid optimization. If the fluid families with a poor molar mass prediction define the perimeter of the convex hull, the pseudo-fluid optimization should avoid these regions, as the accuracy of the model is expected to be lower. Finally, no QSPRs are available for associating fluids. Thus, the associating fluids are also filtered out of the database.

Two convex hulls are generated, one for the polar fluids and one for the non-polar fluids. This is done because polar and non-polar fluid optimizations are done separately. The convex hull around the non-polar fluids is shown in Figure 3.9.

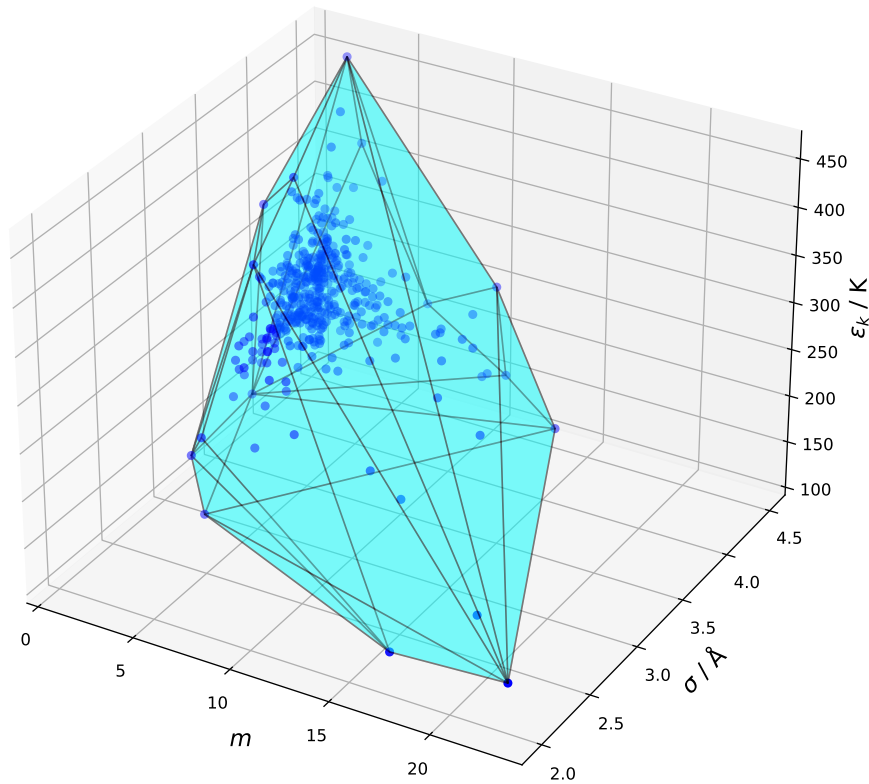


**Figure 3.9:** Convex hull for the non-polar fluids.

### 3.3. Optimizer Details

The genetic algorithm implemented in the package *Pymoo* is used. For optimization problems with local optima, it is always possible that the algorithm converges to one of these local optima. If multiple optimizations are done with different random mutations (through changing the seed for the pseudo-random mutations) and vastly different optima are found, it may be necessary to adjust the algorithm settings to have more aggressive mutations such that the algorithm will no longer get stuck in the different local optima. Having more aggressive mutations does mean the convergence speed is decreased. The main elements of the optimization problem are described in this section.

- **Objective function.** The total fuel mass of the aircraft (including reserves for loitering and diversion), that is, the first objective function ( $f_1$ ), is minimized. As explained above, a second objective ( $f_2$ ) can be used to favor PC-SAFT parameters that more closely match those of a real fluid. In such a case,  $f_2$  is also minimized. The design problem is then formulated as a bi-objective optimization.
- **Constraints.** Compared to previous works, the only constraint that is added is the convex hull constraint as explained in subsection 3.2.3. This hull is defined by a set of hyperplanes of the form shown in Equation 3.19, where  $i$  is the index of the hyperplane. For any point inside the hull, Equation 3.20 is satisfied. The maximum value of the left-hand side of Equation 3.19 for  $i \in N_{\text{eqs}}$  is passed to the optimization algorithm as the constraint value, where a value greater than zero is a violation.

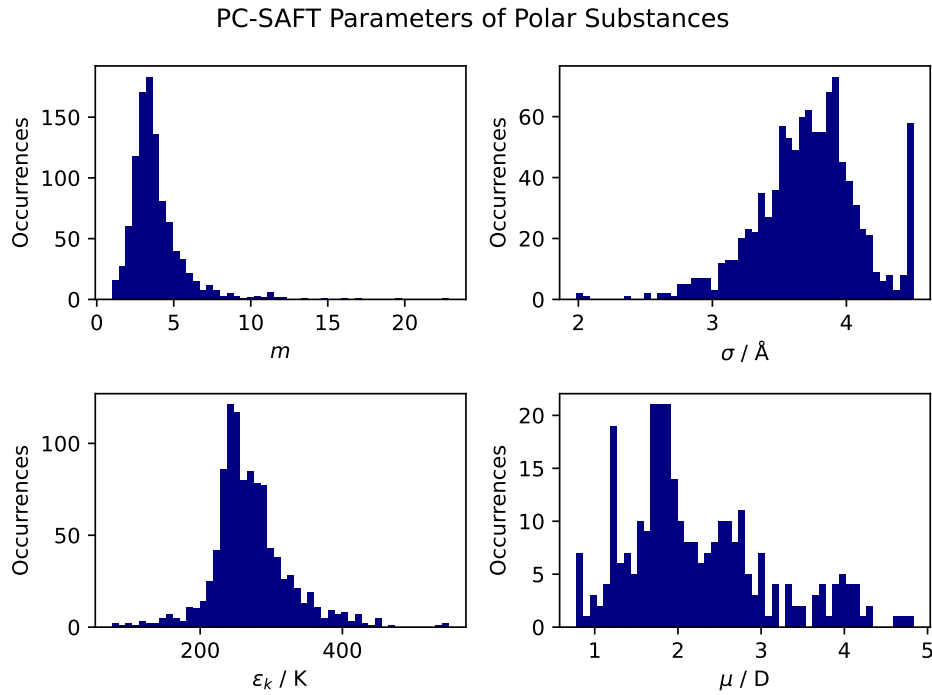
**Table 3.2:** Selection of fluid families in the database by Esper et al. [14] based on the quality of molar-mass fit.

<b>Family</b>	<b>Included</b>	<b>Comment</b>
Sulfides/thiophenes	✓	2 outliers
Fluorides		
Alkynes	✓	
Nitriles	✓	3 outliers
Alkenes	✓	
Aldehydes	✓	2 outliers
Esters	✓	
Other compounds	✓	Second, deviating, trend
Ethers	✓	
Chlorides		
Acids	✓	
Ketones	✓	
Polyfunctional compounds		No discernible trend
Amines	✓	1 bad outlier
Cyclic compounds	✓	
Thiols	✓	
Inorganic compounds		
Halogenated compounds		
Elements		
Silanes/siloxanes	✓	
Alkanes	✓	
Aromatic hydrocarbons	✓	
Alcohols	✓	6 outliers

$$c_{1,i} \cdot m + c_{2,i} \cdot \sigma + c_{3,i} \cdot \epsilon_k + c_{4,i} \cdot \mu + c_{5,i} = 0, \quad (3.19)$$

$$c_{1,i} \cdot m + c_{2,i} \cdot \sigma + c_{3,i} \cdot \epsilon_k + c_{4,i} \cdot \mu + c_{5,i} < 0, \quad \forall i \in N_{\text{eqs}}, \quad (3.20)$$

- **Bounds.** The bounds as shown in Table 3.4 are used. The bounds for the PC-SAFT parameters are the extrema occurring in the filtered database of Esper et al. For mixtures, different bounds are used for the PC-SAFT parameters. These are shown in Table 3.5. The motivation for this is to avoid excessive computational cost for evaluating the fluid properties with *FluidProp* since some combinations at the extremes of PC-SAFT parameter bounds lead to lengthy evaluations. The bounds for the mixture optimizations are chosen such that the outlier PC-SAFT parameter values are excluded. See Figure 3.10 and Figure 3.11 for histograms of the PC-SAFT parameters for the fluids in the filtered database from Esper et al. [14].
- **Algorithm Settings.** The algorithm settings used for most runs are shown in Table 3.3. Since the goal of optimization is to find a global optimum, multiple identical optimization runs are performed with different seed values for the pseudo-random numbers used by the algorithm. This helps determine whether the chosen settings prevent the algorithm from getting stuck in local optima. Different seed values can also lead to slightly different optima, allowing for the selection of the best result. As a rule of thumb, the population size is set to 10 times the number of design variables. Initially, the number of generations is 150, but this can be extended by restarting the optimization with the final population from a previous run. Convergence is assessed on a case-by-case basis. A guideline for convergence is that  $f_1$  remains constant within a 1 kg margin for at least 25 generations.

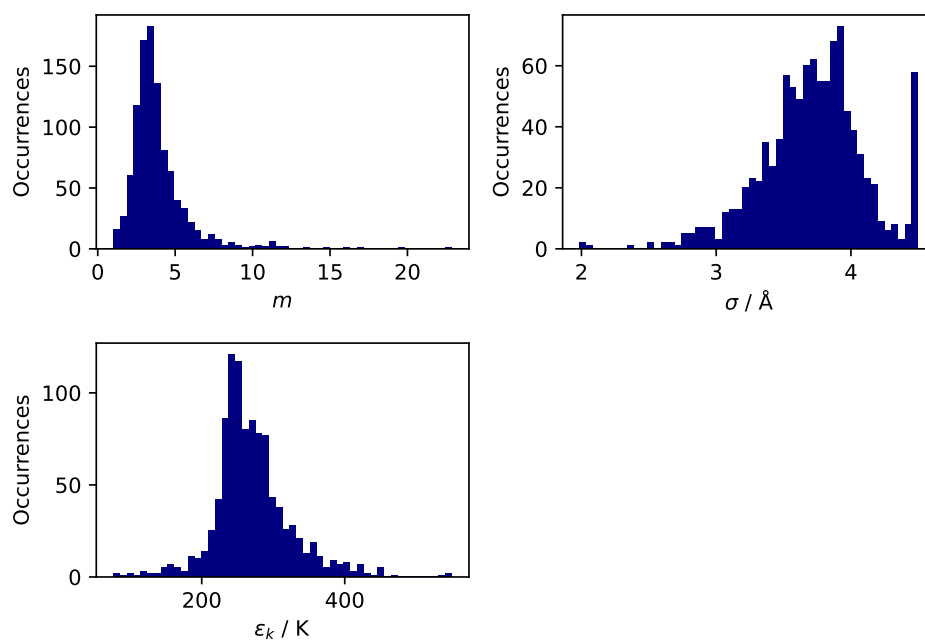


**Figure 3.10:** PC-SAFT parameter histogram for the polar fluids occurring in the database of Esper et al. [14].

**Table 3.3:** Optimizer settings.

Variable	Setting	Value
Real	Crossover eta	15
	Crossover probability	0.8
	Mutation eta	15
	Mutation probability	0.2
Integer	Crossover eta	15
	Crossover probability	0.8
	Mutation eta	15
	Mutation probability	0.2

PC-SAFT Parameters of non-Polar Substances

**Figure 3.11:** PC-SAFT parameter histogram for the non-polar fluids occurring in the database of Esper et al. [14].

**Table 3.4:** Bounds of the optimization problem.

Variable	Symbol / Unit	Lower Bound	Upper Bound
Engine Exhaust PR	$\Pi_{noz} / -$	1.1	1.8
ORC minimum T	$T_{min,orc} / K$	323	423
ORC maximum T	$T_{max,orc} / K$	520	600
ORC maximum normalized p	$\tilde{p}_{max,orc} / Pa$	1.1	1.5
Condenser Pinch Point Delta T	$\Delta T_{pp,cond} / K$	10	100
HRSG Pinch Point Delta T	$\Delta T_{pp,evap} / K$	40	100
Condenser X length	$X_{cond} / m$	0.8	1
Condenser louver angle	$\phi_{l,cond} / ^\circ$	10	30
Condenser fin height	$b_{f,cond} / m$	0.007	0.012
Condenser fin pitch	$p_{f,cond} / m$	0.001	0.004
Condenser microchannel width	$w_{mc,cond} / m$	0.00008	0.003
HRSG number of passes	$n_{pass,evap} / -$	6	19
Massflow ratio intake	$\xi / -$	0.4	1
Condenser tilt angle	$\theta_{cond} / ^\circ$	45	75
Working fluid m	$m / -$	1	23.322
Working fluid sigma	$\sigma / \text{\AA}$	1.9	4.5
Working fluid epsilon	$\epsilon_k / K$	50	550
Working fluid mu	$\mu / D$	0.781	4.83

**Table 3.5:** Deviating and additional bounds for a (pseudo-fluid) mixture optimization. Note that the PC-SAFT parameters occur twice in the design vector for the mixture case.

Variable	Symbol / Unit	Lower Bound	Upper Bound
Working fluid m	$m / -$	2	6
Working fluid sigma	$\sigma / \text{\AA}$	2.5	4.5
Working fluid epsilon	$\epsilon_k / K$	200	300
Working fluid mu	$\mu / D$	0.781	4.83
Working fluid mixture fraction	$z / -$	0.01	0.5

# 4

## Results

First, in section 4.1, the optimization results from previous studies on the Onera Dragon CC-TS equipped with an ORC, along with the reference cases for this work, are discussed. Next, the findings from the optimizations of this work are presented in section 4.2. Finally, to better understand these findings, trends of  $f_1$  for varying  $\Pi_{noz}$  values are analyzed in section 4.3.

### 4.1. Reference Cases

Two reference cases are necessary to interpret the working fluid optimization results. The first is the original Onera Dragon aircraft without an ORC system, as modeled by the *ARENA* framework. The second is the Dragon aircraft, adopting as prime movers turboshaft engines combined with a WHR system with cyclopentane as the working fluid. Both cases have been evaluated in the previous work by Krempus et al. [7].

Building upon the work by Krempus et al., Sinopoli et al. [9] compared the performance of an ORC system operating with toluene or ethanol to that employing cyclopentane as a working fluid. A set of input variables and the optimized design vector are available. However, the exact fuel mass reported in the work by Sinopoli et al. [9] could not be reproduced. This means that the cyclopentane case must be re-evaluated for the current work. The original Dragon case has also been re-evaluated for consistency. For the working fluid optimization results presented later in this chapter, *the input parameter values made available by the main author of ref. [9] are used unless otherwise indicated*. The reference cases, the original Dragon aircraft without the ORC and the aircraft equipped with the ORC using cyclopentane as a working fluid, are presented in subsection 4.1.1 and subsection 4.1.2, respectively.

#### 4.1.1. Original Dragon Aircraft

Of the design variables considered in the CCPU optimization, only one variable, namely  $\Pi_{noz}$ , is considered for the original Dragon aircraft. To understand later how the ORC system affects the optimal  $\Pi_{noz}$  value, it is first investigated what the optimal value for  $\Pi_{noz}$  is for the turboshaft engines on the original Dragon aircraft.

Assuming the required power is constant, the value of  $\Pi_{noz}$  should be such that the total efficiency of the propulsion system, including the propulsive power from the core exhaust, the ram air ducts, and the EDFs is maximized. One effect is that an increased value for  $\Pi_{noz}$  will lead to a higher jet velocity for the core exhaust flow. This decreases the propulsive efficiency for core thrust. An increased  $\Pi_{noz}$  also causes a decreased  $\Pi_{FPT}$ , which affects the isentropic efficiency of the free power turbine ( $\eta_{s,FPT}$ ). Finally, the hotside pressure for the HRSG is increased if  $\Pi_{noz}$  increases. These effects, among others, mean that the complexity is such that analytically determining the optimal  $\Pi_{noz}$  value is not possible.

To still gain insight into the optimal  $\Pi_{noz}$  for the Onera Dragon aircraft without an ORC system, the fuel mass ( $f_1$ ) is determined for  $\Pi_{noz}$  values between 1.15 and 1.50 with steps of 0.05. The result is shown in Figure 4.1. A smooth trend is observed, with a minimum at  $\Pi_{noz} = 1.325$ . This value roughly agrees with what Krempus et al. [7] found, namely an optimal  $\Pi_{noz}$  of 1.35 for the original Dragon case.

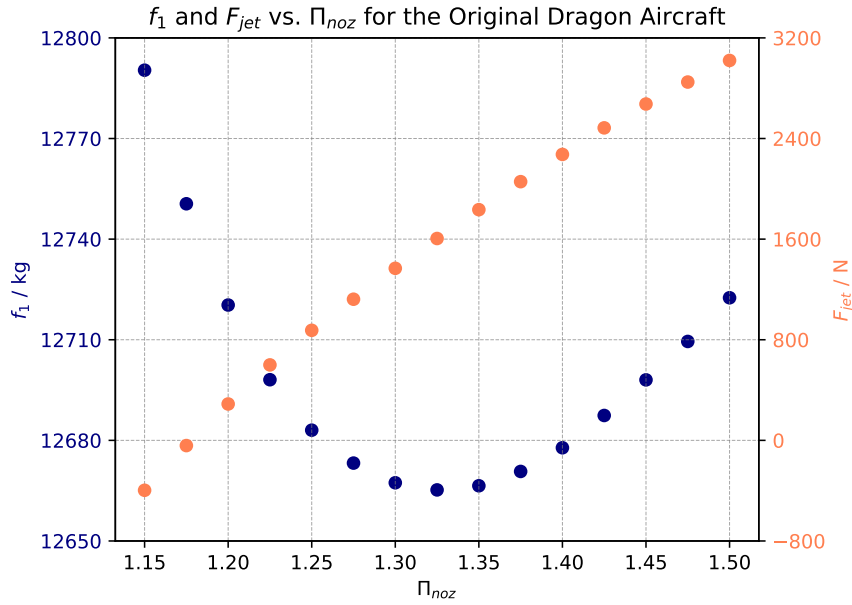


**Figure 4.1:** Trends of jet thrust (Combined thrust of the two CCPUs, excluding the Ram Air Duct) and fuel mass for varying  $\Pi_{noz}$ .

#### 4.1.2. Cyclopentane Baseline Case

In the works by Krempus et al. [7] and Sinopoli et al. [9], the ORC system designed for the aircraft under consideration, the Dragon CC-TS, adopts cyclopentane as a working fluid. The fuel mass reported by Krempus et al. for this case is 12.8t, while Sinopoli et al. report 12.45t. This discrepancy is explained since Sinopoli et al. use different duty coefficients for the engine's turbomachinery.<sup>1</sup> The different parameter values are shown in Table 4.1. The polytropic efficiency estimate is sensitive to changes in the turbomachinery duty coefficients since the polytropic efficiency of the turbomachinery is predicted as a function of the massflow, EIS, and the work coefficient using the correlations presented by Samuelsson et al. [44].

Due to the updated HTC correlations for condensing and single phase flows, as used in the latest version of *HeXacode* and detailed in section 3.1, the CCPU optimization for cyclopentane needs to be re-evaluated. The optimal  $f_1$  value for the system using cyclopentane is needed as a reference to quantify a potential improvement with alternative working fluids. To assess the impact of the modifications made in *HeXacode* with respect to the original work of Krempus et al., optimizations with different combinations of single phase HTC correlation and condensing HTC correlations are done. The results are shown in Table 4.3. It can be seen that with the Gnielinski correlation (as used in the more recent *HeXacode* version), the predicted performance is worse. Also, the correlation by Deng predicts worse performance. Using the correlation by Deng [10] instead of the one by Shah [51] leads to roughly 10 kg of extra fuel consumption. The correlation by Gnielinski [16] leads to roughly 50 kg of extra fuel consumption compared to usage of the Taler correlation [52] that is the default correlation in the previous version of *HeXacode*. The cyclopentane reference case for this work will be referred to as the Baseline case, see Table 4.3. From these results, 50 kg is regarded as a preliminary estimate of the uncertainty of the  $f_1$  prediction due to the model uncertainties.

To gain some more insight into how the Baseline case of this work compares to the original Dragon aircraft according to the calculations in this work,<sup>2</sup> a comparison of key aircraft characteristics is shown in Table 4.2. It can be seen that while the operating empty mass ( $m_{t,oe}$ ) is increased by 1% by adding the ORC system, the total fuel mass ( $f_1$ ) is decreased by 0.92%. This difference is smaller than the 1.5%

<sup>1</sup>There are other differences in input parameters, but those did not show a significant influence on  $f_1$ .

<sup>2</sup>The calculations in this work found slightly different results than what was found in Krempus et al. [7]. This is caused by the differing duty coefficients for the turbomachinery in the turboshaft engine. See Table 4.1.

decrease reported by Krempus et al. The discrepancy can likely be attributed to the use of different HTC correlations. The drag is not significantly different. However, the drag of the enlarged nacelle for the CCPU is not modeled, so, in reality, the difference could be significant, as also recognized by Krempus et al. The jet thrust of the original Dragon aircraft is significantly greater than that of the Baseline case. This either means that the efficiency from fuel to core jet thrust is less with the ORC, or the total efficiency from fuel to EDFs thrust is increased by the inclusion of the ORC. Most likely, the latter is the case.

The optimized design vector of the Baseline case and the total fuel mass ( $f_1$ ) are compared with the previous works in Table 4.4 as evaluated using the same input parameter values and HTC correlations as for the Baseline case. Note that the values for  $x_{l, \text{evap}}$  and  $x_{t, \text{evap}}$  are mixed up in the paper by Sinopoli et al. [9]. Furthermore, this paper also reports a  $\Pi_{\text{noz}}$  value of 1.45. This is also incorrect; the original run data showed a value of 1.24. Finally, Krempus et al. [7] report a  $T_{\text{min,orc}}$  value of 398 K. This value is incorrect; the original run data was reviewed, which showed a value of 368 K instead.

The  $f_1$  values, as shown in Table 4.4 for the optimized design vectors reported in Ref - [7] and Ref - [9], are higher than the Baseline case for this work. This either means that previous optimizations were terminated in local optima further away from the global optimum than the Baseline case or that the optimal design vector depends on input parameter values and/or the HTC correlations that are used. In the work by Krempus et al.,  $\Pi_{\text{noz}}$  is 1.27, which roughly agrees with the value in the Baseline case. The cyclopentane case of Sinopoli et al. agrees well with a value of 1.24 for  $\Pi_{\text{noz}}$ . The condenser pinch point temperature difference is slightly lower in the Baseline case. This can be advantageous for minimizing the irreversibilities arising during heat transfer in the condenser. The Ref - [9] case has a deviating  $n_{\text{pass}}$  value. The optimal value of design variables where the sign and magnitude of the  $\Delta$  are (roughly) the same for Ref - [7] and Ref - [9] are likely affected by the newly used HTC correlations. For example,  $b_{f, \text{cond}}$  and  $p_{f, \text{cond}}$  both have significantly smaller values in both the Ref - [7] and Ref - [9] cases.

**Table 4.1:** Comparison of parameter values used by Krempus et al. (Ref - [7]) and Sinopoli et al. (Ref - [9]).

Parameter	Ref - [7]	Ref - [9]	Parameter	Ref - [7]	Ref - [9]
$\psi_{\text{LPC}}$	0.8	0.3	$\psi_{\text{FPT}}$	3.5	1.5
$\psi_{\text{HPC}}$	1	0.5	$\Pi_{\text{LPC}}$	2.25	5.07
$\psi_{\text{HPT}}$	3.5	2.25	$\Pi_{\text{HPC}}$	20	8.88
$\psi_{\text{LPT}}$	3.5	1.5			

**Table 4.2:** Comparison of the aircraft without ORC (Original Dragon) and the cyclopentane reference case for the current work (Baseline). The  $\Delta$  column reports the difference with respect to the Original Dragon case.

Parameter	Original Dragon	Baseline	$\Delta$
$f_1 / \text{kg}$	12665	12549	-0.92%
$m_{t\text{oe}} / \text{kg}$	42633	43069	+1.0%
$D / \text{N}$	36122	36109	~
$F_{\text{jet}} / \text{N}$	1605	204	-87.3%
$\eta_{\text{net,pu}}$	51.4%	51.8%	+0.4%pt.

**Table 4.3:** Fuel mass comparison of optimized CCPU cases using cyclopentane with different versions of HTC correlations. Correlations from Shah [51], Deng et al. [10], Taler [52] and Gnielinski [16].

Case Tag	Single Phase HTC Correlation	Condensing HTC Correlation	$f_1$ / kg
	Taler	Shah	12499
	Taler	Deng	12517
Baseline	Gnielinski	Deng	12549

**Table 4.4:** Comparison of the design vectors for the Baseline case, Krempus et al. (Ref - [7]) and Sinopoli et al. (Ref - [9]). The  $f_1$  values reported in this table are evaluated with the input parameter values and the same heat transfer correlations as for the Baseline case; see Table 4.3. The asterisk (\*) denotes that the value was fixed during the optimization. The  $\Delta$  column reports the difference with respect to the Baseline case.

Parameter	Baseline	Ref - [7]	$\Delta$	Ref - [9]	$\Delta$
$f_1$ / kg	12549	12588	+0.31%	12577	+0.22%
$\Pi_{\text{noz}}$ / -	1.24	1.27	+2.8%	1.24	
$T_{\text{min,orc}}$ / K	364	368	+1.1%	373	+2.3%
$T_{\text{max,orc}}$ / K	545	549	+0.7%	544	-0.2%
$p_{\text{max,orc}}$ / bar	54.4*	54.4		53.1	-2.4%
$\Delta T_{\text{pp,evap}}$ / K	100	97.8	-2.2%	99.9	-0.1%
$\Delta T_{\text{pp,cond}}$ / K	39.7	41.8	+5.3%	43.1	+8.6%
$X_{\text{cond}}$ / m	1	1		1	
$\phi_{\text{l,cond}}$ / °	30	29.7	-1.0%	29.8	-0.6%
$b_{\text{f,cond}}$ / mm	11.3	10.1	-10.3%	10.4	-7.6%
$p_{\text{f,cond}}$ / mm	1.67	1.41	-15.5%	1.5	-10.1%
$x_{\text{t,evap}}$ / -	3*	3		3	
$x_{\text{l,evap}}$ / -	1.3*	1.25	-3.8%	1.25	-3.8%
$n_{\text{pass,evap}}$ / -	10	9		5	
$\xi$ / -	0.673	0.67	-0.4%	0.676	+0.5%
$\theta_{\text{cond}}$ / °	61.1	59.4	-2.7%	64.5	+5.6%

## 4.2. Working Fluid Optimization Results

In this section, the results of the working fluid optimizations are presented. First, in subsection 4.2.1, the results of pure fluid optimizations are explained and compared to the reference cases. Next, in subsection 4.2.2, the binary mixture optimization results are presented.

### 4.2.1. Optimized CCPU using Pure Fluids

As explained in section 3.2, the first step is to study the potential improvement possible for a pure fluid. Using the CoMT approach resulted in optimal polar and non-polar pseudo-fluids. Subsequently, a bi-objective optimization problem is solved attempting to identify optimal real fluids in a single step. The results for the pure pseudo-fluid optimization are presented first. Then, results for real fluids closely neighboring the pseudo-fluid optima (CNRFs) and the bi-objective optimization are presented.

### Optimized CCPU using CoMT

Various CoMT optimizations are carried out for both non-polar and polar PC-SAFT parameters. The optimizations with different algorithm seeds converged to different optimal design vectors, implying multiple local optima for the optimization problem. The three best-performing pseudo-fluids are selected from the sets of non-polar and polar CoMT optimizations. The  $f_1$  values of these cases can be found in the left part of Table 4.5. For the non-polar pseudo-fluids, the best performance is reached by the Non-Polar Pseudo-Fluid (NPPF)-1 case. The fuel mass for this case is 12467 kg, which raises the ORC fuel savings from 0.92% for cyclopentane to 1.56%. The two other NPPFs are NPPF-2 and NPPF-3. Both have an  $f_1$  just under 12490 kg. Next are the polar pseudo-fluids. The best case there is Polar Pseudo-Fluid (PPF)-1 with an  $f_1$  value of 12472 kg. This value is followed by PPF-2 and PPF-3 with  $f_1$  close to 12480 kg. The  $f_2$  value, measuring the distance to the CNRF, which is the fluid from the database by Esper et al. with the least Euclidean distance in the normalized PC-SAFT space to the pseudo-fluid currently considered (see Equation 3.18), is also given in the table to get a sense of how close the pseudo-fluid is to a real fluid. It is noticed that there is a wide variation in  $f_2$ , an outlier of 0.16 for PPF-3 and a relatively small  $f_2$  of 0.0253 for NPPF-1. Do note that  $f_2$  only indicates how well the CNRF resembles the pseudo-fluid in terms of the PC-SAFT parameters. The relation between  $f_2$  and the performance discrepancy in terms of  $f_1$  between optimized designs for a pseudo-fluid and the corresponding CNRF shall become apparent later in this subsection.

**Table 4.5:**  $f_1$  values for the six best performing pseudo-fluids and four CNRF counterparts to pseudo-fluids. The  $\Delta$  value indicates the difference with respect to the Original Dragon case as indicated by the  $\equiv$  sign.

Case Tag	$f_1$ / kg	$\Delta$	$f_2$	Case Tag	$f_1$ / kg	$\Delta$
Original Dragon	12665	$\equiv$				
Baseline	12549	-0.92%				
NPPF-1	12467	-1.56%	0.0253	CaDi	12495	-1.35%
NPPF-2	12487	-1.41%				
NPPF-3	12489	-1.39%				
PPF-1	12472	-1.53%	0.0592	AcCh	12492	-1.37%
PPF-2	12481	-1.45%	0.0776	Mecro	12500	-1.3%
PPF-3	12482	-1.45%	0.16	AcAn	13137	+3.72%

The PC-SAFT parameter values for the six pseudo-fluid cases are visualized in Figure 4.2. This figure shows that  $m$  and  $\mu$  have relatively narrow ranges for optimal pseudo-fluids compared to the bounds interval. The values are more spread out for  $\sigma$  and  $\epsilon_k$ . For  $m$ , this is primarily because of a few substances with outlier values for this parameter, as can be seen in the PC-SAFT parameter histograms (Figure 3.10 and Figure 3.11) for the fluid database from ref. [14] which lead to the relatively wide bounds for this parameter. The following observation is that for  $m$  and  $\epsilon_k$ , the values for the pseudo-fluids are more or less centered around the value for cyclopentane. Only for  $\sigma$  do the pseudo-fluids show a tendency for lower values. None of the PC-SAFT parameters of the NPPF-1 and PPF-1 cases are very close together, which suggests there is not a single optimum for the PC-SAFT parameters  $m$ ,  $\sigma$ , and  $\epsilon_k$ . All PC-SAFT parameter values for the pseudo-fluids and those of the CNRFs together with the  $f_2$  values can be found in Table 4.6.

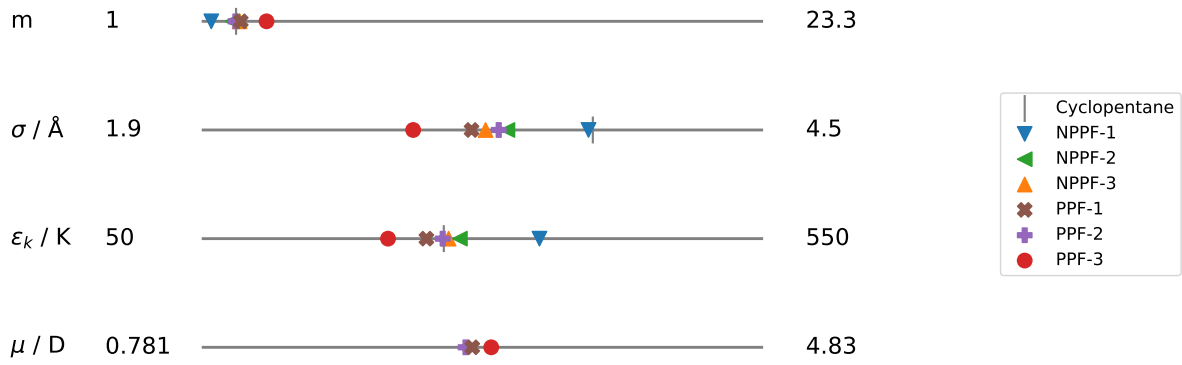


Figure 4.2: Pseudo-fluid optima positioning on the bounds interval.

Table 4.6: PC-SAFT Parameters of the the six best performing pseudo-fluids and CNRFs to four of the six pseudo-fluids. NPPF-2 and NPPF-3 have the same CNRF: 1,4-dioxane. This fluid is not considered in this work since, initially, a different fluid was mistakenly identified as CNRF, such that there was not sufficient time left to consider this fluid.

(Pseudo-) Fluid	$m$	$\sigma / \text{\AA}$	$\epsilon_k / \text{K}$	$\mu / \text{D}$	$f_2$
Cyclopentane	2.36	3.71	266		
NPPF-1	1.38	3.69	351		0.0253
Carbon disulfide	1.54	3.75	354		
NPPF-2	2.22	3.32	280		
NPPF-3	2.51	3.21	270		
PPF-1	2.55	3.15	250	2.73	0.0592
Acetyl chloride	2.63	3.26	237	2.72	
PPF-2	2.34	3.28	265	2.68	0.0776
Methacrolein	2.58	3.49	257	2.68	
PPF-3	3.58	2.88	216	2.87	0.16
Acetic anhydride	4.12	3.14	248	2.87	

For a more detailed evaluation of the obtained optimal designs, the NPPF-1 and PPF-1 cases are selected since they exhibit the lowest  $f_1$  values. The design vectors for these cases are shown alongside the one for cyclopentane (Baseline case) in Table 4.7. Compared to the bounds,  $\Pi_{\text{noz}}$  shows little variability.  $T_{\text{min,orc}}$  as well as  $T_{\text{max,orc}}$  show some variation.  $\tilde{p}_{\text{max,orc}}$  is the first variable showing significant variability. While it is lower for both pseudo-fluid cases, the maximum cycle pressure is greater, as shown in Table 4.9. This is because the predicted  $p_{\text{crit}}$  is much greater for the pseudo-fluids. An effect of a high maximum pressure is heavier HRSG tubing. This might cause  $\tilde{p}_{\text{max,orc}}$  to be at its lower bound for the pseudo-fluid cases. Next to consider are the condenser and HRSG temperature differences at the respective pinch points. For the pseudo-fluid cases, these values are somewhat smaller in the HRSG and significantly smaller in the condenser, compared to the Baseline case. From an ORC thermodynamic efficiency point of view, heat transfer across a smaller temperature difference is favorable. While this points to decreased irreversibilities arising during heat transfer, leading to increased cycle efficiency, the pinch point temperature difference by itself is not sufficient information to draw any definitive conclusions on the irreversibilities arising during heat transfer. Next,  $X_{\text{cond}}$  shows very little variation with a tendency to hit the upper bound. The  $\phi_{1,\text{cond}}$  values are also invariably hitting the upper bound. The condenser fin height and fin pitch are decreased for both pseudo-fluid cases compared to the Baseline case. This is possibly explained by the decreased pinch point temperature difference in the condenser and the constrained outer dimensions of the condenser, causing the need for higher fin efficiency (smaller fin height) and more fins (smaller fin pitch). The condenser microchannel width

affects the heat transfer through the Reynolds number and the temperature profile in the fluid as well as the number of microchannels for a fixed flat-tube width, which is in turn related to the heat transfer area between the working fluid and the flat-tube walls. The number of passes in the HRSG is relatively stable across the three cases, between eight and ten. Thus, this is a reasonable balance between working fluid pressure loss and irreversibilities due to heat transfer. Also, this optimum for the number of passes seems independent of the working fluid. The massflow ratio of the intake ( $\xi$ ) is stable at around 0.67 to 0.68.

Looking at the system characteristics shown in Table 4.8, the optimized pseudo-fluid cases show a roughly equal operating empty mass ( $m_{t,oe}$ ). Indeed, the variation of the ORC system mass ( $m_{t,orc}$ ) is negligible. Interestingly, the drag of the NPPF-1 case is increased by 0.3% compared to the Baseline case, while for the PPF-1 case, the drag is decreased by 0.2%. The drag is proportional to  $m_{cr}$  (see Equation 3.13), assuming a constant L/D.  $m_{cr}$  increases with increasing fuel mass, also through the snowball effect of increased fuel mass, leading to increased takeoff mass and thus increased aircraft empty mass, since empty mass is proportional to the takeoff mass. The operating empty mass indeed varies with the same sign, albeit with a decreased magnitude. Also affecting the drag is the ram air duct thrust ( $F_{RAD}$ ) since that is counted as a decrease in zero-lift drag. Indeed, the NPPF-1 case shows a strongly decreased  $F_{RAD}$ . The PPF-1 case shows an increased  $F_{RAD}$  values compared to the Baseline case. Looking at the cruise power demand ( $\dot{W}_{ccpu}$ ) for the pseudo-fluid cases, this shows the compounded effect of increased core jet thrust and, in the case of PPF-1, decreased drag. More closely related to the fuel consumption is the engine power ( $\dot{W}_{ts}$ ). It can be seen that the NPPF-1 has the strongest decrease, closely followed by PPF-1. The net efficiency of the engine ( $\eta_{net,pu}$ ) of both the pseudo-fluid cases is decreased. This is mostly due to the definition of efficiency where core jet thrust is not counted as power output; only electrical output power is counted. The ORC characteristics provide a clear picture of how the pseudo-fluids improve the engine performance with respect to the Baseline case. In both pseudo-fluid cases, the power output of the ORC is increased, although this is seen most strongly for the NPPF-1 case. The efficiency of the ORC system is also significantly improved. Again, it is most strongly improved for the NPPF-1 case. The increased ORC efficiency comes at the cost of higher HRSG hotside pressure drop ( $\Delta p_{evap,HS}$ ). The NPPF-1 solution features the highest pressure drop. This is expected for the most efficient ORC system since the strict size constraints on the heat exchangers lead to strong trade-offs between pressure loss and the effectiveness of the heat exchangers. The exhaust gas temperature at the HRSG inlet ( $T_{evap,HS,in}$ ) is indicative of the efficiency of the turboshaft engine. This variable slightly increases in the two pseudo-fluid cases, shifting some power production from the FPT to the ORC system. This is due to the increased value of  $\Pi_{noz}$  for the pseudo-fluid designs compared to the Baseline design. Concerning the ram air duct, the decreased  $F_{RAD}$  in the NPPF-1 case seems caused by the increased  $\Delta p_{cond,CS}$  which in turn is affected by the increased  $Z_{cond}$ . It is seen that the increased  $\dot{m}_{RAD}$  is correlated with a lower optimal value of the condenser tilt angle ( $\theta_{cond}$ ) where a  $\theta_{cond}$  of 0 means orthogonal to the bulk flow direction. Since the optimal value of  $X_{cond}$  is near the upper bound at 1 m, the diffuser outlet area is determined primarily by  $\theta_{cond}$ . When  $\dot{m}_{RAD}$  increases, so must the diffuser inlet area. When the area ratio of the diffuser remains constant, this entails the diffuser outlet area increases,  $\theta_{cond}$  can decrease to decrease pressure loss due to the tilted position of the condenser. The alternative solution will be to decrease the diffuser area ratio ( $R_{diffuser}$ ) and maintain the same tilt angle. The fact that the optimizer does not select this solution suggests that reducing the tilt angle is more effective in mitigating the pressure loss than decreasing the area ratio of the diffuser. Indeed, in Table 4.9 it is shown that  $R_{diffuser}$  is at the upper bound of the feasible range.

Looking at the PPF-1 case, the condenser heat load ( $Q_{cond}$ ) is decreased. This allows for a decreased  $Z_{cond}$  which in turn enables a decreased  $\Delta p_{cond,CS}$  and thus a slightly increased  $F_{RAD}$ .

**Table 4.7:** Design vectors for the optimal non-polar (NPPF-1) and polar (PPF-1) pseudo-fluid cases. The  $\Delta$  column reports the difference with respect to the Baseline case. The asterisk (\*) denotes that the value was fixed during the optimization.

Parameter	Baseline	NPPF-1	$\Delta$	PPF-1	$\Delta$
$f_1 / \text{kg}$	12549	12467	-0.65%	12472	-0.61%
$\Pi_{\text{noz}}$	1.24	1.3*	5.2%	1.3	5.3%
$T_{\text{min,orc}} / \text{K}$	364	356	-2.2%	374	2.8%
$T_{\text{max,orc}} / \text{K}$	545	557	2.0%	570	4.6%
$\tilde{p}_{\text{max,orc}}$	1.32	1.1	-16.8%	1.1	-16.7%
$\Delta T_{\text{pp,evap}} / \text{K}$	100	95.1	-4.9%	83.6	-16.4%
$\Delta T_{\text{pp,cond}} / \text{K}$	39.7	17.9	-54.8%	21	-47.1%
$X_{\text{cond}} / \text{m}$	1	1		0.977	-2.3%
$\phi_{1,\text{cond}} / ^\circ$	30	30		30	
$b_{f,\text{cond}} / \text{mm}$	11.3	10.6	-6.0%	8.43	-25.1%
$p_{f,\text{cond}} / \text{mm}$	1.67	1.62	-2.9%	1.5	-10.3%
$w_{\text{mc,cond}} / \text{mm}$	-	1.72		2.99	
$n_{\text{pass,evap}}$	10	10		8	
$\xi$	0.673	0.681	1.3%	0.673	0.1%
$\theta_{\text{cond}} / ^\circ$	61.1	57.3	-6.2%	65.1	6.5%
$m$	-	1.38		2.55	
$\sigma / \text{\AA}$	-	3.69		3.15	
$\epsilon_k / \text{K}$	-	351		250	
$\mu / \text{D}$	-	-		2.73	

**Table 4.8:** Aircraft and CCPU characteristics for the reference cyclopentane case (Baseline), the best performing non-polar pseudo-fluid case (NPPF-1) and the best performing polar pseudo-fluid case (PPF-1). The  $\Delta$  column reports the difference with respect to the Baseline case.

	Parameter	Baseline	NPPF-1	$\Delta$	PPF-1	$\Delta$
Aircraft	$f_1 / \text{kg}$	12549	12467	-0.65%	12472	-0.61%
	$m_{\text{toe}} / \text{kg}$	43069	43101	+0.1%	43025	-0.1%
	$D / \text{N}$	36109	36210	+0.3%	36025	-0.2%
	$F_{\text{jet}} / \text{N}$	204	747	+267%	827	+306%
	L/D	17.32	17.27	-0.3%	17.34	+0.1%
CCPU	$\dot{W}_{\text{ccpu}} / \text{kW}$	5385	5318	-1.2%	5280	-2.0%
	$\eta_{\text{net,ccpu}}$	54.0%	53.7%	-0.3%pt.	53.3%	-0.7%pt.
Turbo-shaft	$\dot{W}_{\text{ts}} / \text{kW}$	5169	5026	-2.8%	5033	-2.6%
	$\eta_{\text{net,pu}}$	51.8%	50.8%	-1.0%pt.	50.8%	-1.0%pt.
	$\dot{m}_2 / (\text{kg/s})$	10.62	10.54	-0.7%	10.55	-0.6%

**Table 4.9:** ORC and ram air duct characteristics for the reference cyclopentane case (Baseline), the best performing non-polar pseudo-fluid case (NPPF-1) and the best performing polar pseudo-fluid case (PPF-1). The  $\Delta$  column reports the difference with respect to the Baseline case.

	Parameter	Baseline	NPPF-1	$\Delta$	PPF-1	$\Delta$
ORC	$p_{\max,orc}$ / bar	54.4	98.2	+80%	78.3	+44%
	$\dot{W}_{orc}$ / kW	217	292	+35%	247	+14%
	$\eta_{orc}$	16.0%	20.2%	+4.2%pt.	18.9%	+2.9%pt.
	$m_{torc}$ / kg	219	242	+10.7%	215	-1.8%
	$\eta_{s,ORCT}$	89.0%	89.1%	+0.1%pt.	88.1%	-0.9%pt.
HRSG	$\Delta p_{evap,HS}$ / Pa	1660	1990	+20%	1880	+13%
	$T_{evap,HS,in}$ / K	653	663	+1.5%	662	+1.4%
	$Q_{evap}$ / kW	1360	1450	+6.5%	1310	-3.7%
	$T_{t,5}$ / K	653	663	+1.5%	662	+1.4%
	$T_{t,7}$ / K	537	539	+0.3%	550	+2.5%
COND & RAD	$\mathcal{R}_{diffuser}$	5.99	5.99	-0.0%	5.94	-0.7%
	$Q_{cond}$ / kW	1130	1140	+0.7%	1050	-7.2%
	$Z_{cond}$ / m	0.065	0.069	+6.5%	0.048	-26.2%
	$F_{RAD}$ / N	228	119	-47.8%	263	+15.5%
	$\dot{m}_{RAD}$ / (kg/s)	6.39	7.21	+13.0%	5.50	-13.9%
	$\Delta p_{cond,CS}$ / Pa	369	493	+33.7%	310	-15.9%
	$\theta_{cond}$ / °	61.1	57.3	-6.2%	65.1	+6.5%

The T-s diagrams of the Baseline case and the optimal polar and non-polar pseudo-fluid cases are shown together in Figure 4.3. It is noticed that for both the NPPF-1 and PPF-1 cases, the desuperheating is negligible, whereas for cyclopentane, the desuperheating is significant. Since there is no recuperator used in the current system, desuperheating leads to a larger amount of thermal energy being rejected through the condenser. Thus, the optimal fluid is less complex than cyclopentane and is characterized by a more symmetric saturation dome, such that the working fluid at the turbine exit is in a saturated condition. As mentioned previously and can be recognized in the diagram, the pinch point temperature differences in both the condenser and the HRSG for the two pseudo-fluid cases are relatively small compared to the Baseline case. The temperature profile in the HRSG is comparable. The slope of the bubble line varies slightly between the three cases. Also, the decreased slope of the isobaric curve near the critical point is more pronounced for the pseudo-fluids. This makes sense because the normalized maximum pressure ( $\tilde{p}_{\max,orc}$ ) is at the lower bound (1.1) for both pseudo-fluid cases such that the increase of the heat capacity near the critical point is stronger. The flattening of the isobars near the critical point is illustrated for cyclopentane in Figure A.4 in Appendix A.

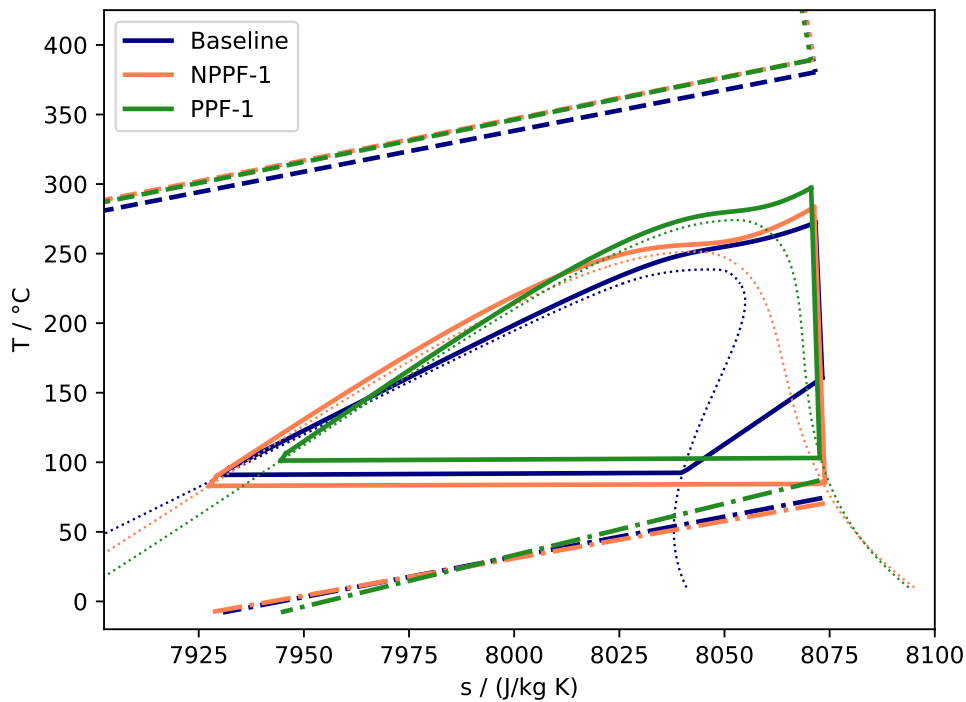


**Figure 4.3:** T-s diagrams for the non-polar (NPPF-1) and polar (PPF-1) optimal pseudo-fluid cases versus the reference cyclopentane case (Baseline).

#### Optimized CCPU using Real Fluids

In the best-case scenario, (NPPF-1), The  $f_1$  improvement due to the ORC system increases by 0.64 percentage points compared to the Baseline case. While this may seem modest, it is significant given that  $f_1$  improvement of the Baseline case compared to the original Dragon aircraft is of a similar magnitude, at 0.92%, according to the calculations in this work. However, a real fluid is unlikely to match the improvement found for the optimal pseudo-fluid. To a certain extent, real fluids represent a subset of the pseudo-fluid design space. This means that the optimal pseudo-fluid sets the ceiling for any performance improvement achievable by selecting the optimal working fluid for the ORC system under design.

The approaches for identifying a suitable real fluid were outlined in subsection 3.2.2. Given that the maximum potential improvement in  $f_1$  is already modest, an extensive search for the optimal real fluids using these approaches is not justified. Instead, the study focused on comparing CNRFs—the real fluids that are closest to the pseudo-fluid optima, as defined according to the  $f_2$  formulation (see Equation 3.18)—with the pseudo-fluid optima. The CNRFs for four of the six pseudo-fluid cases will be evaluated next. Four CNRFs were identified during the project. Their characteristics and the corresponding performance of the CC-TS engine are discussed below.

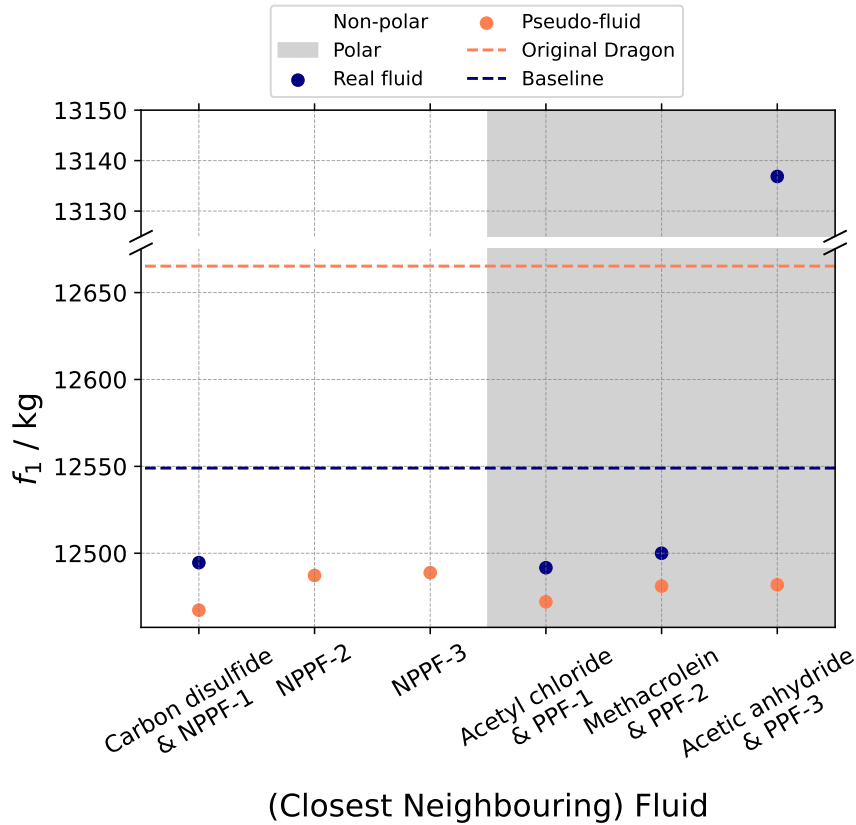


**Figure 4.4:** Fuel consumption of the Dragon aircraft for the optimal pseudo-fluids and the identified CNRF. Note that the fluid model for the 'real fluids' is still the PC-SAFT EOS with the fixed parameters of that fluid fixed according to Esper et al. [14].

The four real fluid candidates corresponding to pseudo-fluid cases are shown in the right part of Table 4.5. Some safety and hazard classifications for these substances are shown in Table 4.10. Whereas the best-performing pseudo-fluid exhibited an improvement in  $f_1$  of 0.64 percentage points with respect to the Baseline case, the best real fluid from the four that are tested is acetyl chloride. This fluid exhibits a 0.45 percentage point improvement upon the Baseline case. The two other fluids with a slightly less, but still decent agreement with their pseudo-fluid counterpart are methacrolein and carbon disulfide. Methacrolein and carbon disulfide practically exhibit the same performance as acetyl chloride considering the magnitude of the model uncertainty, estimated at 50 kg. Finally, acetic anhydride shows very poor performance, with a 3.72% increase in fuel consumption with respect to the original Dragon aircraft. It is not surprising that there is a large discrepancy between the performance of the system with the pseudo-fluid and the CNRF, given the high  $f_2$  value for the pseudo-fluid. Considering the hazard classifications in Table 4.10, it does not seem likely that any of the identified molecules are usable as a working fluid. However, a thorough evaluation of whether the substances are feasible working fluids is outside the scope of this work. While flammability does not necessarily prevent the use of a compound as an ORC working fluid, being corrosive and toxic is likely problematic. Finally, a substance is only suitable as a working fluid if the thermal stability is sufficient to avoid decomposition at the highest temperature reached in the cycle.

For the carbon disulfide, acetyl chloride, and methacrolein cases, the discrepancy with the pseudo-fluid cases is insignificant compared to the discrepancy of acetic anhydride with its corresponding pseudo-fluid. In the pseudo-fluid cases, desuperheating is eliminated by finely adjusting the PC-SAFT parameters such that the saturated vapor line is close to the turbine exit flow state. Considering this, it is not surprising that for CNRFs, with notably different PC-SAFT parameters from those of the corresponding pseudo-fluids, the dew line is not sufficiently close to the turbine expansion process to eliminate vapor desuperheating in the condenser.

As seen in Table 4.5, an  $f_2$  value in the 0.025–0.078 range—where NPPF-1, PPF-1, and PPF-2 fall—

**Table 4.10:** Safety and hazard classifications for the four CNRFs identified in the study. The checkmark indicates that the substance has the characteristic reported along the table columns [38, 39, 40, 41].

Substance	Flammable	Toxic	Corrosive
Carbon disulfide	✓	✓	
Acetic anhydride	✓		✓
Methacrolein	✓	✓	✓
Acetyl chloride	✓		✓

suggests that the properties of the CNRF will, to some extent, resemble those of the pseudo-fluid, such that the  $f_1$  value for the optimized systems is roughly similar. However, a precise match is not guaranteed.

The T-s diagram for the optimized system in the NPPF-1 case and the optimized system for the corresponding CNRF, namely carbon disulfide, are compared in Figure 4.5. Given the fact that the  $f_1$  values of the pseudo-fluid and real fluid are relatively close, the thermodynamic characteristics of carbon disulfide are unsurprisingly similar to those of the original pseudo-fluid. Carbon disulfide shows a higher critical temperature and a more skewed saturation dome. Thus, the saturation dome is not such that the vapor is saturated at the turbine exit, and a certain level of desuperheating occurs in the condenser.

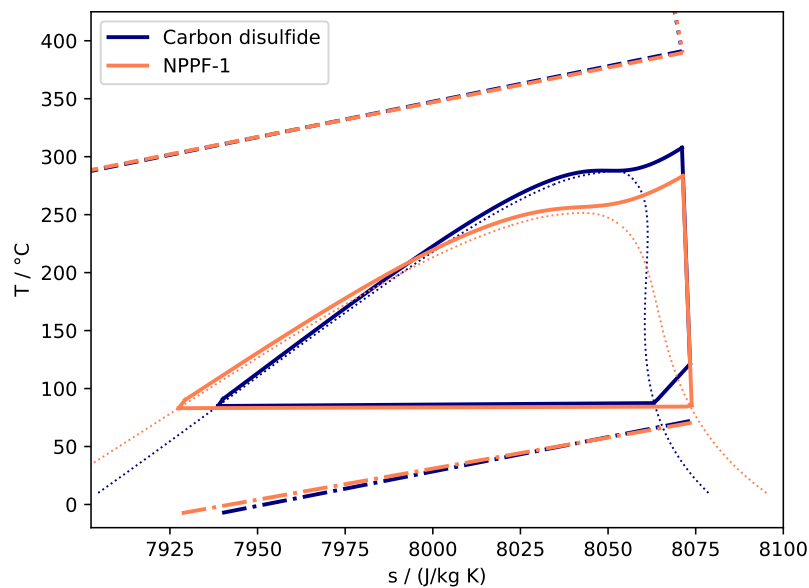


**Figure 4.5:** T-s diagram of the optimized ORC systems for NPPF-1 and the corresponding CNRF (Carbon disulfide).

The T-s diagram for the optimized systems using acetyl chloride and the corresponding pseudo-fluid are shown in Figure 4.6. The critical temperature of acetyl chloride is lower than that of the pseudo-fluid. Also, similar to the carbon disulfide case, some vapor desuperheating is needed. For the real fluid (CNRFs) discussed thus far, vapor desuperheating in the condenser is still of limited extent compared to cyclopentane.

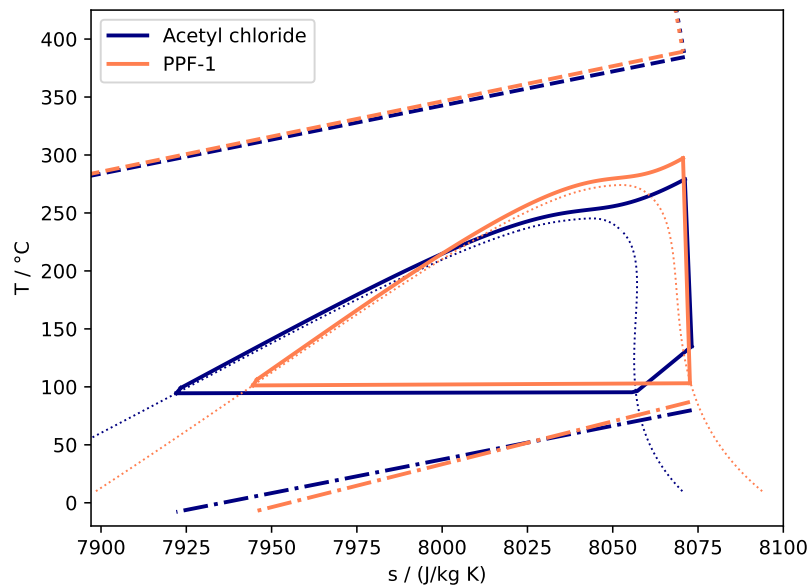


**Figure 4.6:** T-s diagram of the optimized ORC systems for PPF-1 and the corresponding CNRF (Acetyl chloride).

The approach of finding pseudo-fluids that perform well and evaluating the CNRFs in a second stage proved to be a reasonably effective way to optimize the preliminary design of the ORC system for a pure component working fluid. A more sophisticated method is the bi-objective optimization as explained in subsection 3.2.2. The results of two bi-objective non-polar fluid optimizations are presented next.

The first bi-objective optimization (case tag NPPF-MO-1 where MO means Multi-Objective) found the lowest  $f_1$  value of 12514 kg for a pseudo-fluid with the CNRF furan. The  $f_2$  value for this solution is 0.03. The order of magnitude of  $f_2$  is similar to that found for the pseudo-fluid optima shown in Table 4.5. This implies that the properties of the pseudo-fluid are still significantly different from the properties of the CNRF, meaning that the performance in terms of  $f_1$  cannot be matched by adopting the identified working fluid.

since the order of magnitude of  $f_2$  is similar to those of the pseudo-fluid optima shown in Table 4.5, the properties of the pseudo-fluid are still significantly different from the properties of the CNRF. This implies that the performance in terms of  $f_1$  cannot be matched by the real molecule.

The  $f_1$ - $f_2$  Pareto front for NPPF-MO-1 is seen in Figure 4.7. It is observed that the best  $f_1$  value reached for an  $f_2$  value near zero ( $f_2 < 1e-3$ ) is 12.6t. There, the fluid parameters approach those of 2,3-pentadiene. Thus, this optimization did not successfully find well-performing pure fluids such as carbon disulfide or acetyl chloride.

A second optimization with a different algorithm seed (case tag NPPF-MO-2) did not succeed in finding well-performing fluids either. The Pareto front of this optimization is shown in Figure 4.8. The best-performing individuals have the CNRF furan with a minimum  $f_1$  value of 12496 kg. Again, with a  $f_2$  value of 0.031, the discrepancy between the properties of the pseudo-fluid and those of the CNRF is still significant. The best-performing point in the real fluid part of the  $f_2$  interval ( $f_2 < 1e-3$ ), is 1,3-cyclohexadiene with  $f_1$  values starting around 12.56t.

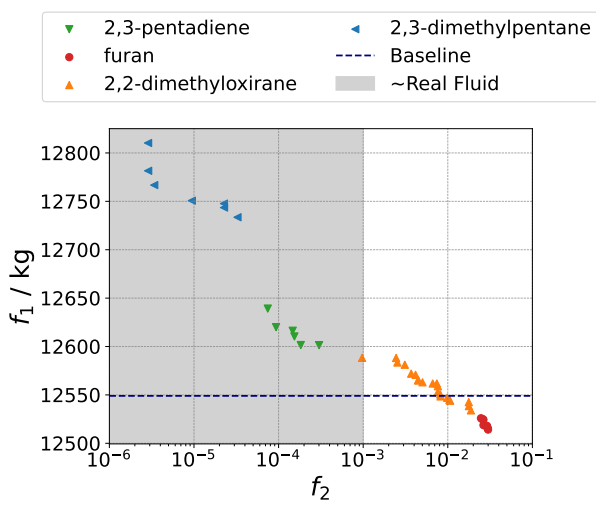


Figure 4.7: Pareto front for the NPPF-MO-1 bi-objective optimization.

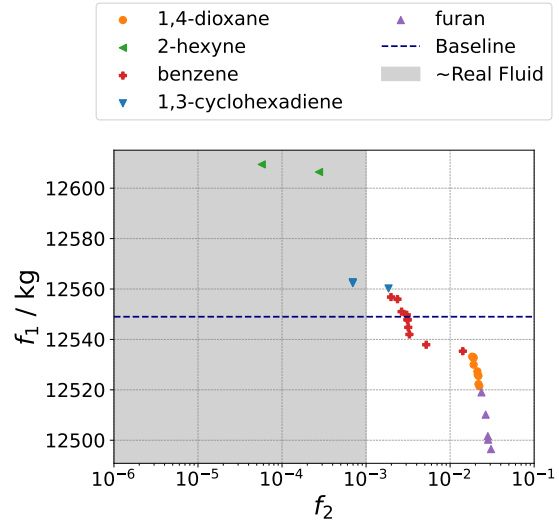


Figure 4.8: Pareto front for the NPPF-MO-2 bi-objective optimization.

#### 4.2.2. Optimized CCPU using Fluid Mixture CoMT

Binary mixtures as a working fluid can be beneficial for the performance of an ORC system. For a given pinch point temperature difference in the condenser, this is the case if the temperature glide during condensation matches well with the temperature increase in the cooling medium, or, in other words, if the temperature profile of the mixture during condensation tends to be parallel to the heat exchanger's cold side temperature profile.

This means that the minimum cycle temperature ( $T_{\min,orc}$ ) can be decreased compared to a cycle where condensation occurs isothermally with the same pinch point temperature difference ( $\Delta T_{pp,cond}$ ). This is favorable for the efficiency of the ORC. Additionally, a lower  $T_{\min,orc}$  allows the working fluid to cool the heat source to a lower temperature, thus increasing the power recovered from the heat source. However, as previously mentioned, achieving a smaller temperature difference in the condenser implies an increased heat transfer area. This conflicts with the space limitations of the CCPU. Additionally, as mentioned in section 2.4, the application can come with adverse effects, such as a decreased heat transfer coefficient compared to pure fluids [31].

To discover if mixtures have the potential to improve  $f_1$  for the system under consideration, a non-polar pseudo-fluid mixture optimization is done. The best  $f_1$  value for this case study (case NPPF-MIX) is 12,496 kg. Compared to the best pure pseudo-fluid result, the NPPF-1 case with an  $f_1$  value of 12,467 kg, the mixture performs worse. The reason why a pseudo-fluid mixture cannot offer a performance benefit becomes more apparent when looking at the T-s diagram of the non-polar pseudo-fluid mixture compared to the NPPF-1 case in Figure 4.9. The temperature glide in the condenser for the NPPF-MIX case is negligible. Indeed, when looking at the PC-SAFT parameters of the pseudo-fluid mixture, shown in Table 4.11, the two fluids have relatively similar parameters with the result that the temperature glide is negligible.

Table 4.11: PC-SAFT parameters of the non-polar pseudo-fluid mixture case NPPF-MIX.

CNRF	$f_2$	$m_1$	$\sigma_1 / \text{\AA}$	$\epsilon_{k1} / \text{K}$	$Z$
Cyclobutane	0.0189	2.11	3.64	264	0.15
CNRF	$f_2$	$m_2$	$\sigma_2 / \text{\AA}$	$\epsilon_{k2} / \text{K}$	
Furan	0.0767	2.57	3.13	263	0.85

In theory, when a heat sink with limited heat capacity is employed, the optimal solution sink should feature a temperature glide so that it more closely follows the temperature profile of the heat sink. This would, in

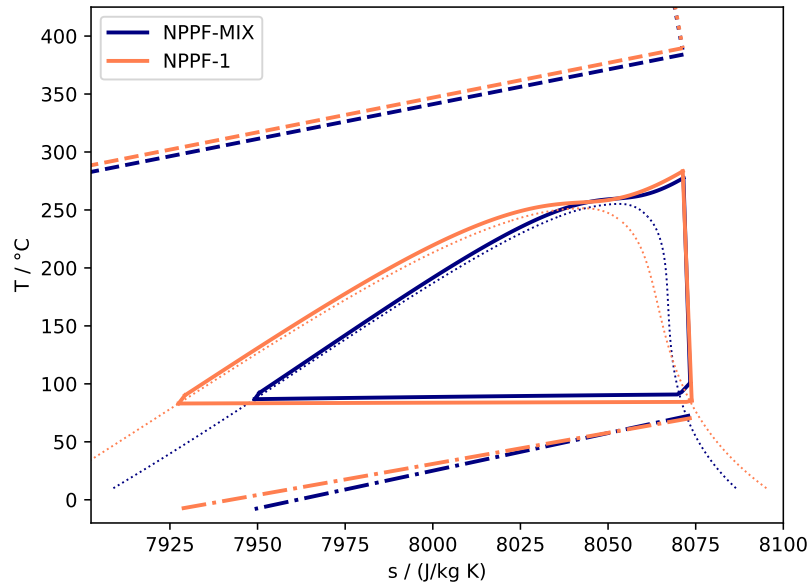


**Figure 4.9:** T-s diagrams of the best performing non-polar pseudo-fluid mixture and the best performing non-polar pure pseudo-fluid.

turn, require a smaller average temperature difference in the heat exchanger. Since the HTC decreases for mixtures compared to pure fluids [31], the heat transfer area would need to increase significantly for a zeotropic mixture. As shown in Table 4.12, the X dimension remains comparable to that of the Baseline and NPPF-1 cases, while the Y dimension is a fixed parameter in the model. Notably, the condenser depth ( $Z_{\text{cond}}$ ) is smaller than in the Baseline and NPPF-1 cases. This reduction, combined with a larger microchannel width ( $w_{\text{mc}}$ ), results in a lower condenser mass ( $m_{t\text{cond}}$ ), which contrasts with expectations for a bottoming unit operating with a mixture as a working fluid. (see Table 4.13). Most of the other design parameters of the NPPF-MIX case align closely with those in the NPPF-1 case, as detailed in Table 4.12.

This design choice has significant performance implications. A smaller  $Z_{\text{cond}}$  decreases the heat transfer area on both the hot and cold sides of the condenser, leading to suboptimal ORC performance. In the optimization study for pure fluids, as discussed in subsection 4.2.1, a negative correlation was observed between  $Z_{\text{cond}}$  and ram air duct thrust ( $F_{\text{RAD}}$ ). Larger  $Z_{\text{cond}}$  values increase coldside pressure losses, reducing  $F_{\text{RAD}}$ . As mentioned above, working fluid mixtures exhibiting a temperature glide require a greater heat transfer area. Given the fixed X and Y dimensions, this would necessitate an increase in  $Z_{\text{cond}}$ . However, in the NPPF-MIX case, the optimizer does not follow this trend. Despite the potential benefits of temperature glide—such as enhanced cycle efficiency or an increased heat recovery from the engine exhaust gases—it is possible that the associated drawbacks, including higher pressure loss leading to reduced  $F_{\text{RAD}}$ , outweigh these advantages. If this is indeed the case, this would explain why the optimizer prioritizes minimizing these adverse effects over exploiting a temperature glide, identifying a design that does not increase the condenser size with respect to pure fluids. However, this cannot be concluded definitively based on the current results.

To gain a better understanding of why mixtures cannot offer a benefit for the system here studied, two additional optimizations are performed. The first one is with a fixed working fluid mixture of 50% cyclohexane and 50% cyclopentane (BM-Cyhe-Cype, where BM means Binary Mixture). The second optimization is with a mixture of cyclopropane and cyclopentane, where the mixture fraction is allowed to vary between 6% and 94% (BM-Cypr-Cype). The convergence of this optimization run is visible in Figure 4.10. The reason for not selecting the mixture fraction bounds as 0% and 100% is to ensure the final design exhibits some temperature glide in the condenser such that this effect on the thermodynamic cycle can be better understood. For the BM-Cypr-Cype case, the mixture fraction converged

**Table 4.12:** Comparison of the design vector for a 50% cyclohexane 50% cyclopentane mixture (BM-Cyhe-Cype, where BM stands for Binary Mixture), a 6% cyclopropane 94% cyclopentane mixture (BM-Cypr-Cype), and an optimized pseudo-fluid mixture (NPPF-MIX). The  $\Delta$  column reports the difference with respect to the Baseline case.

Variable	Baseline	BM-Cypr-Cype	$\Delta$	BM-Cyhe-Cype	$\Delta$	NPPF-MIX	$\Delta$
$f_1 / \text{kg}$	12549	12620	+0.6%	12578	+0.2%	12496	-0.4%
$\Pi_{\text{noz}} / -$	1.24	1.23	-0.1%	1.27	+2.5%	1.28	+3.2%
$T_{\text{min,orc}} / \text{K}$	364	371	+1.9%	369	+1.4%	360	-1.1%
$T_{\text{max,orc}} / \text{K}$	545	546	+0.2%	549	+0.7%	551	+1.0%
$\tilde{p}_{\text{max,orc}} / -$	1.32	1.12	-15.7%	1.1	-16.8%	1.1	-16.7%
$\Delta T_{\text{pp,evap}} / \text{K}$	100	99.4	-0.5%	99.3	-0.7%	100	-0.0%
$\Delta T_{\text{pp,cond}} / \text{K}$	39.7	50.4	+27.0%	44.4	+11.9%	22.3	-43.9%
$X_{\text{cond}} / \text{m}$	1	0.966	-3.4%	0.984	-1.6%	0.993	-0.7%
$\phi_{1,\text{cond}} / \text{degrees}$	30	27.9	-7.0%	28.3	-5.5%	28.9	-3.7%
$b_{\text{f,cond}} / \text{mm}$	11.3	9.5	-15.6%	8.12	-27.8%	11	-2.3%
$p_{\text{f,cond}} / \text{mm}$	1.67	1.62	-3.0%	1.52	-8.7%	1.63	-2.4%
$w_{\text{mc,cond}} / \text{mm}$	-	1.94		1.58		1.9	
$n_{\text{pass,evap}} / -$	10	9		9		9	
$\xi / -$	0.673	0.643	-4.5%	0.693	+3.1%	0.661	-1.7%
$\theta_{\text{cond}} / \text{degrees}$	61.1	63.1	+3.4%	75	+22.8%	62.7	+2.7%
$m_1 / -$	-	2.26		2.26		2.11	
$\sigma_1 / \text{\AA}$	-	3.75		3.76		3.64	
$\epsilon_{k1} / \text{K}$	-	273		274		264	
$z / -$	-	0.938		0.5		0.15	
$m_2 / -$	-	1.86		2.5		2.57	
$\sigma_2 / \text{\AA}$	-	3.48		3.85		3.13	
$\epsilon_{k2} / \text{K}$	-	233		281		236	

to the lower bound with 6% cyclopropane and 94% cyclopentane.

The design vectors for the BM-Cypr-Cype and BM-Cyhe-Cype cases are shown in Table 4.12. The  $f_1$  values are higher than that of the Baseline case. Notably, the values for  $\Delta T_{\text{pp,cond}}$  are significantly greater than that of the Baseline.  $T_{\text{min,orc}}$  increases by 7 K or 5 K, and the  $\Delta T_{\text{pp,cond}}$  values rise by 11 K or 5 K. This suggests that the Logarithmic Mean Temperature Difference (LMTD) (see Equation 4.1, where the subscripts  $A$  and  $B$  represent the two ends of the heat exchanger, respectively), which can be seen as the effective temperature difference for heat transfer, cannot be reduced in the condenser to enhance system performance when the working fluid mixture exhibits a temperature glide during condensation. Another notable difference is that the louver angle is not at the upper bound for any of the mixture cases, in contrast to the clear trend observed for the pure pseudo-fluids. Additionally, the condenser fin height is significantly reduced for the BM-Cypr-Cype and BM-Cyhe-Cype cases, possibly to increase the efficiency of the fins by limiting the temperature decrease of the fin away from the flattubes, compensating for a decreased HTC. It is also worth mentioning the increased tilt angle of the condenser for the BM-Cyhe-Cype case, which suggests a decreased air mass flow for the ram air duct.

$$\text{LMTD} = \frac{\Delta T_A - \Delta T_B}{\ln \Delta T_A - \ln \Delta T_B} \quad (4.1)$$

**Table 4.13:** Comparison of condenser characteristics for the best non-polar pseudo-fluid case (NPPF-1), the best polar pseudo-fluid case (PPF-1) and the best non-polar pseudo-fluid mixture case (NPPF-MIX). The  $\Delta$  column reports the difference with respect to the Baseline case.

	Parameter	Baseline	NPPF-1	$\Delta$	PPF-1	$\Delta$	NPPF-MIX	$\Delta$
COND	$Z_{\text{cond}} / \text{m}$	0.065	0.069	+6.5%	0.048	-26.2%	0.055	-15.8%
	$m_{t\text{cond}} / \text{kg}$	35.7	38.8	+8.9%	27.5	-23.0%	29.9	-16.2%
	$\phi_1 / ^\circ$	30	30		30	+0.0%	28.9	-3.7%
	$b_f / \text{mm}$	11.3	10.6	-6.0%	8.43	-25.1%	11	-2.3%
	$p_f / \text{mm}$	1.67	1.62	-2.9%	1.5	-10.3%	1.63	-2.4%
	$w_{\text{mc}} / \text{mm}$	1.6	1.72	+7.4%	2.99	+86.7%	1.9	+18.5%
	$F_{\text{RAD}}$	228	119	-47.8%	263	+15.5%	161	-29.3%
Ram Air Duct	$\dot{m}_{\text{RAD}} / (\text{kg/s})$	6.39	7.21	+13.0%	5.5	-13.9%	6	-6.0%
	$\Delta p_{\text{cond,CS}} / \text{Pa}$	369	493	+33.7%	310	-15.9%	298	-19.2%
	$\theta_{\text{cond}} / ^\circ$	61.1	57.3	-6.2%	65.1	+6.5%	62.7	+2.7%

Details regarding the solution at the aircraft and the CCPU level are provided in Table 4.14. It is observed that the jet thrust ( $F_{\text{jet}}$ ) for the BM-Cypr-Cypr and BM-Cyhe-Cypr cases falls between the values for the Baseline and the optimal pseudo-fluid cases. Overall, the characteristics of the CCPU and the turboshaft are comparable to those of the Baseline case. Information about the ORC system and the ram air duct is shown in Table 4.15. The power generated by the ORC system and its efficiency are lower than those of the Baseline case.  $Z_{\text{cond}}$  is reduced, with the most significant decrease seen in the BM-Cyhe-Cypr case. This reduction appears to be related to the decreased ram air duct air mass flow and the relatively small condenser heat duty in this case. A trend is observed: as the temperature glide in the condenser increases, the thermal power entering and exiting the ORC system decreases. In Figure 4.11, two T-s diagrams for the mixture cases are compared to the Baseline case. Although the condenser temperature glide remains small compared to, for instance, the desuperheating temperature difference ( $\Delta T$ ), it is not negligible. In conclusion, while the results suggest that working fluid mixtures do not benefit the system, a well-founded explanation for why temperature glide in these mixtures fails to improve performance has not yet been established based on the current results.

**Table 4.14:** Characteristics for the reference cyclopentane case (Baseline), a 50% cyclohexane 50% cyclopentane mixture (BM-Cyhe-Cypr) and a 6% cyclopropane 94% cyclopentane mixture (BM-Cypr-Cypr). The  $\Delta$  column reports the difference with respect to the Baseline case.

	Parameter	Baseline	BM-Cypr-Cypr	$\Delta$	BM-Cyhe-Cypr	$\Delta$
Aircraft	$f_1 / \text{kg}$	12549	12620	+0.6%	12578	+0.2%
	$m_{t\text{oe}} / \text{kg}$	43069	43109	+0.1%	42962	-0.2%
	$D / \text{N}$	36109	36091	0%	36067	-0.1%
	$F_{\text{jet}} / \text{N}$	204	154	-24.7%	581	+185%
	L/D	17.3	17.4	+0.20%	17.3	00%
	CCPU	$\dot{W}_{\text{ccpu}} / \text{kW}$	5385	5390	+0.1%	5322
$\eta_{\text{net,ccpu}}$		54.0%	53.8%	-0.30%	53.3%	-0.80%
Turbo-shaft	$\dot{W}_{\text{ts}} / \text{kW}$	5170	5190	+0.40%	5150	-0.40%
	$\eta_{\text{net,pu}}$	51.8%	51.8%	-0.10%	51.5%	-0.30%
	$\dot{m}_2$	10.62	10.68	+0.56%	10.64	+0.19%

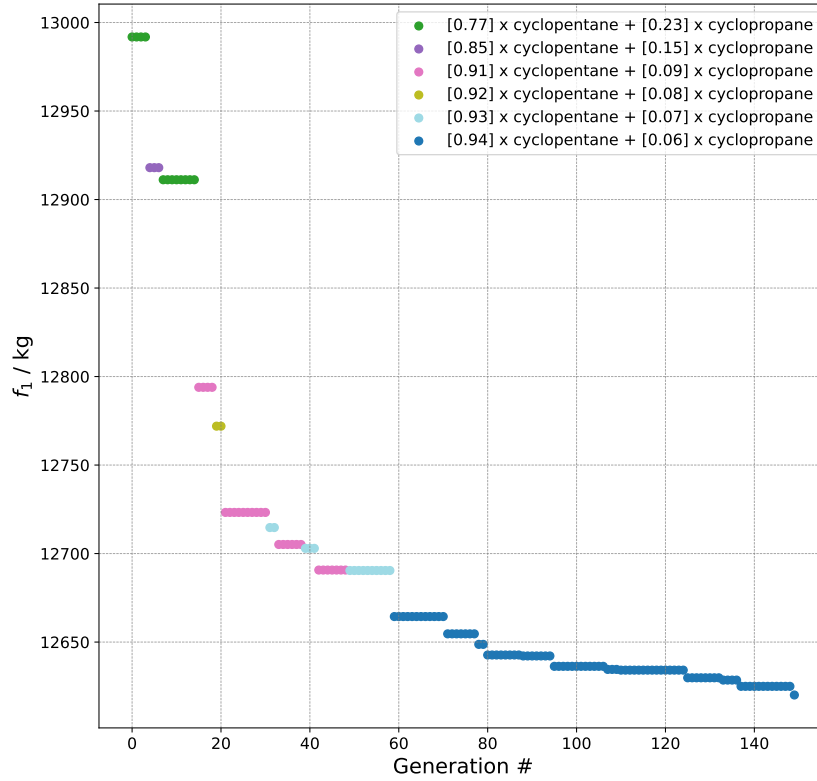
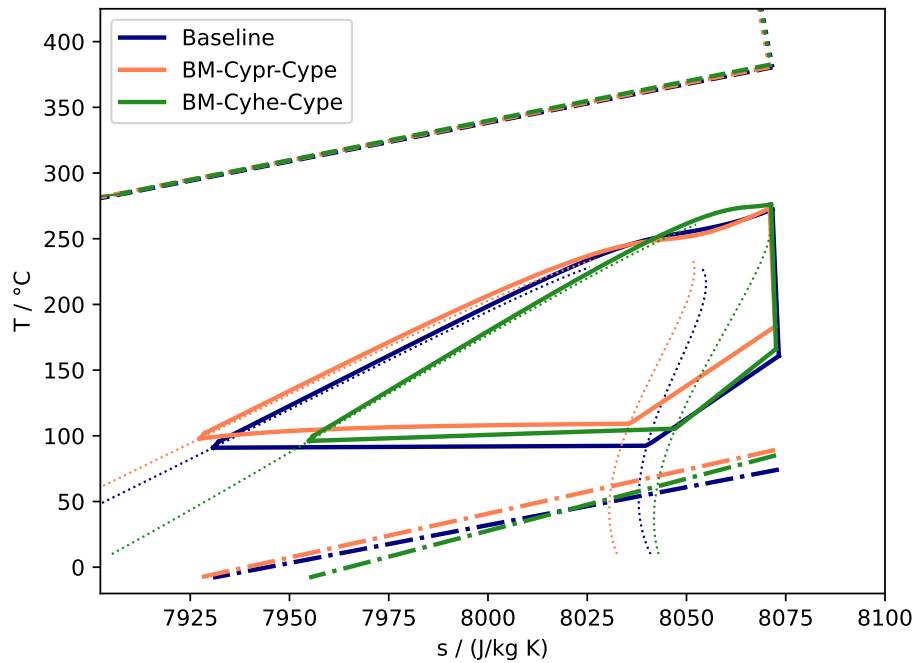


Figure 4.10:  $f_1$  convergence for the BM-Cypr-Cypr optimization.

Table 4.15: Characteristics for the reference cyclopentane case (Baseline), a 50% cyclohexane 50% cyclopentane mixture (BM-Cyhe-Cypr) and a 6% cyclopropane 94% cyclopentane mixture (BM-Cypr-Cypr). The  $\Delta$  column reports the difference with respect to the Baseline case.

	Parameter	Baseline	BM-Cypr-Cypr	$\Delta$	BM-Cyhe-Cypr	$\Delta$
ORC	$\dot{W}_{orc} / \text{kW}$	217	202	-6.70%	173	-20.2%
	$\eta_{orc}$	16.0%	13.9%	-2.10%	15.0%	-1.00%
	$p_{max,orc} / \text{bar}$	54.4	58.7	+7.80%	53.7	-1.30%
	$m_{torc} / \text{kg}$	219	223	+1.90%	175	-20.1%
	$\eta_{s,FPT}$	89.0%	89.1%	+0.10%	87.2%	-1.80%
	$\Delta T_{GL} / \text{K}$	-	6.9		10.9	
HRSG	$T_{evap,HS,in} / \text{K}$	653	654	+0.10%	656	+0.40%
	$\Delta p_{evap,HS} / \text{Pa}$	1662	1897	+14.1%	1453	-12.6%
	$Q_{evap} / \text{kW}$	1359	1454	+7.1%	1154	-15.1%
COND & RAD	$Q_{cond} / \text{kW}$	1131	1242	+9.8%	972	-14.1%
	$Z_{cond} / \text{m}$	0.0650	0.0601	-7.60%	0.0411	-36.7%
	$F_{RAD}$	228	291	+27.7%	217	-4.60%
	$\dot{m}_{RAD} / (\text{kg/s})$	6.39	6.36	-0.50%	5.20	-18.6%
	$\Delta p_{cond,CS} / \text{Pa}$	369	394	+6.90%	238	-35.5%
	$\theta_{cond} / \text{degrees}$	61.1	63.1	+3.40%	75.0	+22.8%



**Figure 4.11:** T-s diagrams for the cyclopentane reference case (Baseline), a 50% cyclohexane 50% cyclopentane mixture (BM-Cyhe-Cype) and a 6% cyclopropane 94% cyclopentane mixture (BM-Cypr-Cype).

### 4.3. Parametric Studies

Downstream of the HRSG, the exhaust gases are expanded through a nozzle, whose pressure ratio ( $\Pi_{noz}$ ), together with the total temperature ( $T_7$ ), determines the exhaust jet velocity. The exhaust jet velocity, together with the turboshaft engine mass flow, determines the gross thrust of the engine. The Baseline design shows around 200 N of jet thrust ( $F_{jet}$ ) produced by the two CCPU's combined for a  $\Pi_{noz}$  value of 1.24. This amounts to roughly half a percent of the total thrust required in the cruise condition. The solutions obtained for the optimal pseudo-fluid show jet thrust values up to 830 N with a  $\Pi_{noz}$  value of 1.3.

Thus, the pseudo-fluid optimizations revealed values for  $F_{jet}$  that significantly deviate from those for the cyclopentane Baseline case and the previous works by Krempus et al. [7] and Sinopoli et al. [9]. To better understand the reasons behind this and to gain further insight into how the presence of the ORC system downstream of the gas turbine influences the optimal value for  $\Pi_{noz}$  and, consequently,  $F_{jet}$ , a parametric study is conducted on the value of  $\Pi_{noz}$ . First, to gain some perspective on the trend for the baseline employing cyclopentane, the analysis for this working fluid is provided in subsection 4.3.1. Next, the results of the study for designs employing pseudo-fluids are presented in subsection 4.3.2.

#### 4.3.1. Core exhaust nozzle pressure ratio trend for cyclopentane as working fluid

The result is shown in Figure 4.12. The optimal  $\Pi_{noz}$  value appears to be on the lower end of the 1.22 to 1.3 interval. However, since the lower bound of the interval is not low enough to observe an increase in  $f_1$ , it cannot be concluded which is the optimal value of  $\Pi_{noz}$  of the CC-TS engine considered in this work, though the optimum is expected to lie within the 1.22 to 1.25 range. For the cyclopentane designs,  $f_1$  shows a distinct trend as a function of  $\Pi_{noz}$ . The effect of the different algorithm seeds is not significant. Also worth noting is that for the Baseline design a decrease in  $F_{jet}$  compared to the original Dragon aircraft is seen.

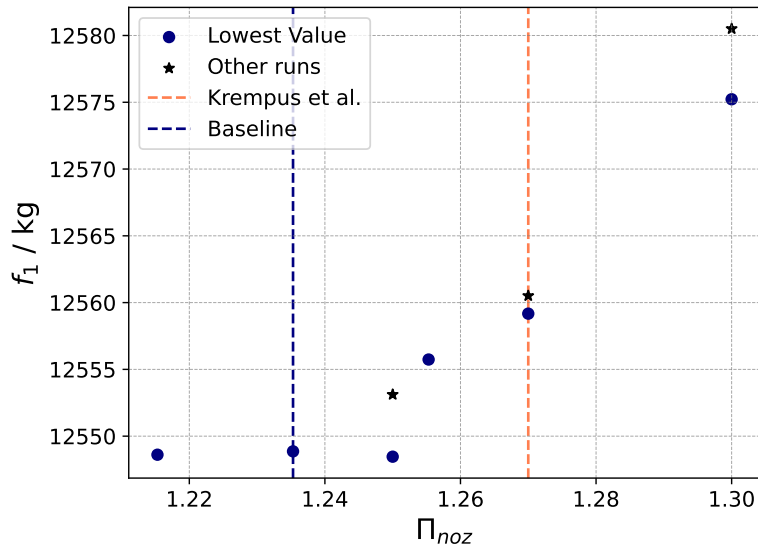


**Figure 4.12:**  $f_1$  for designs with different values of  $\Pi_{noz}$  using cyclopentane as a working fluid. The values for 'Other runs' illustrate the convergence uncertainty compared to the trend.

### 4.3.2. Core exhaust nozzle pressure ratio trend for pseudofluids as working fluids

The  $f_1$  values obtained by optimizing the CC-TS engine design for a range of  $\Pi_{noz}$  values are shown in Figure 4.13. Unlike the original Dragon aircraft, the relationship between  $\Pi_{noz}$  and  $f_1$  is not smooth or easily identifiable. This is because the EDFs now also receives power from the ORC system. Additionally, the core nozzle inlet pressure is affected by the pressure drop in the HRSG. This means that many effects related to the CC-engine design influence the relative contribution of the core nozzle to the overall thrust. For example, there is a trade-off between the pressure loss in the HRSG duct and the magnitude of the thermal energy input of the ORC system. Also, lowering the exhaust gas temperature by transferring thermal power to the ORC working fluid leads to a decreased jet thrust for a constant  $\Pi_{noz}$ .

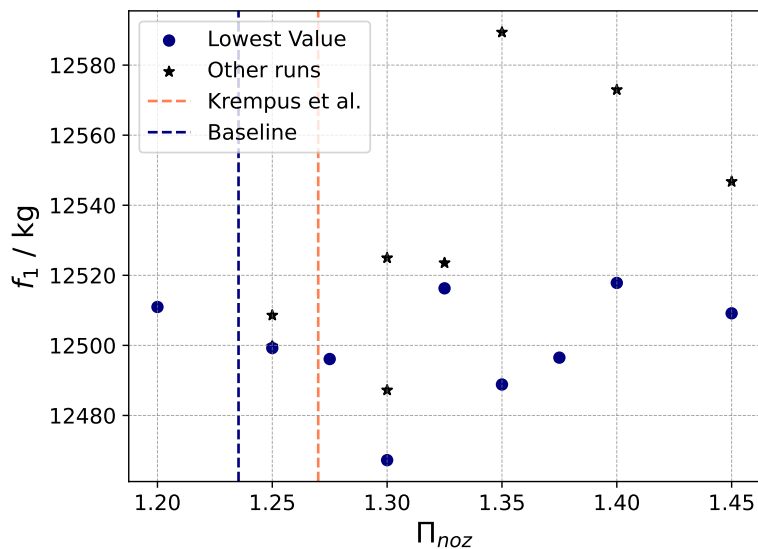


**Figure 4.13:** Fuel mass for optimized pseudo-fluid designs as a function of the prescribed value of  $\Pi_{noz}$ .

These interactions and the limited number of optimizations make it challenging to establish if a distinct

trend exists. For example, for  $\Pi_{noz} = 1.325$ , it was expected that  $f_1$  should be somewhere between the  $f_1$  values for  $\Pi_{noz} = 1.3$  and  $\Pi_{noz} = 1.35$ . The reason is likely that the number of optimizations carried out with different optimization seeds is insufficient or that the genetic algorithm settings are suboptimal. The points labeled 'other runs' are included to illustrate the uncertainty associated with different local optima identified by varying the algorithm seed. The figure indicates an optimum at  $\Pi_{noz} = 1.3$ , but  $f_1$  remains relatively insensitive to  $\Pi_{noz}$  within the tested range. In fact, the variation of  $f_1$  between  $\Pi_{noz}$  values of 1.2 and 1.45 is roughly 40 kg of fuel.

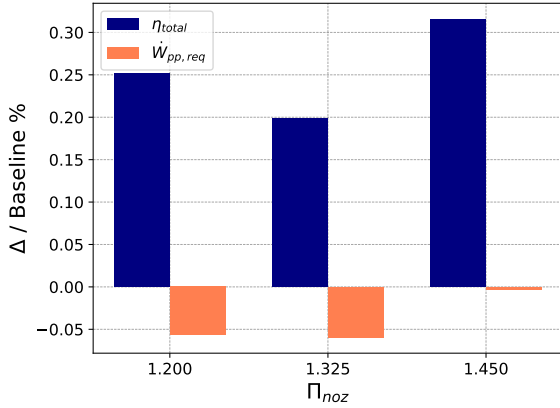


**Figure 4.14:** Normalized overall efficiency ( $\eta_{total}$ ) and normalized required power ( $\dot{W}_{pp,req}$ ) for pseudo-fluid designs in the cruise condition with respect to  $\Pi_{noz}$ . The reference values are those of the Baseline design. Trends of both variables with respect to  $\Pi_{noz}$ .

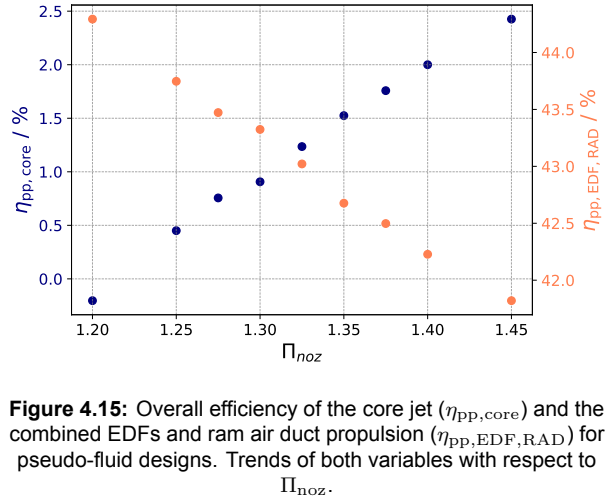


**Figure 4.15:** Overall efficiency of the core jet ( $\eta_{pp,core}$ ) and the combined EDFs and ram air duct propulsion ( $\eta_{pp,EDF,RAD}$ ) for pseudo-fluid designs. Trends of both variables with respect to  $\Pi_{noz}$ .

In Figure 4.14, the total efficiency of propulsive power production ( $\eta_{total}$ ), that is the propulsive power divided by the chemical power ( $\dot{W}_{chem}$ ) for designs employing pseudo-fluids is plotted, non-dimensionalized with respect to the efficiency of the baseline design. Also, the required cruise power ( $\dot{W}_{pp,req}$ ) is plotted using the same non-dimensionalization procedure. Some variation in the normalized required power is also observed. However, the variation is one order of magnitude less than that of the normalized  $\eta_{total}$  values. Thus, the best  $f_1$  value is expected where the value of  $\eta_{total}$  is highest. This is the case for  $\Pi_{noz} = 1.3$ . In Figure 4.15, the total efficiencies of propulsive power production are shown for both the contributions from the core exhaust jet (see Equation 3.14) and the EDFs together with the ram air ducts of the ORC bottoming unit (see Equation 3.15). As the value of  $\Pi_{noz}$  increases, the propulsive power of the core jet increases, leading to a higher value of  $\eta_{pp,core}$ . Conversely, the value of  $\eta_{pp,EDF,RAD}$  decreases with an increasing value of  $\Pi_{noz}$ . The trends are linear.

Increasing  $\Pi_{noz}$  simultaneously increases the share of the total thrust provided by the core exhaust and deteriorates the propulsive efficiency of the core jet. By reasoning, it is speculated that if the gas power can be converted to thrust more efficiently by the EDFs than by the core nozzle, it is beneficial to decrease  $\Pi_{noz}$ . This is the case for the region to the right of the intersection between the red and the solid green line in Figure 4.16. Note that this figure is purely illustrative and that in reality, the relevant efficiencies are the product of jet generation and propulsive efficiency for the core jet, and for the EDFs, this is also multiplied by the conversion efficiency of the turbine, generator, power distribution system, and the fans. Additionally, the relation is affected by the power recovery of the ORC system and the thrust of the ram air ducts. However, for simplicity, the efficiencies are labeled as propulsive efficiency only. As mentioned, the optimal  $\Pi_{noz}$  could not be determined for designs operating with pseudo-fluids. Since adopting an ORC bottoming system with cyclopentane affects the optimal  $\Pi_{noz}$ , it is conceivable that a design with an ORC system utilizing an optimal pseudo-fluid again has a different value for  $\Pi_{noz}$ . Furthermore, the efficiency of the FPT can be slightly affected by a change in the engine design, which would affect the  $\Pi_{noz}$  according to the reasoning explained above. The effect of a more efficient ORC system could entail that the optimal  $\Pi_{noz}$  is increased because this would entail an increased exhaust gas pressure in the evaporator. However, this cannot be determined from the results of the current work.

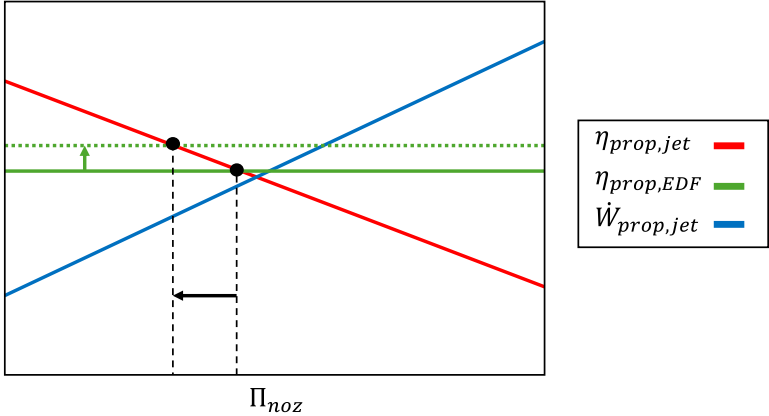


Figure 4.16: Illustration of the effect of a changing  $\eta_{prop,EDF}$  on the  $\Pi_{noz}$  value where increasing  $\Pi_{noz}$  leads to lower total efficiency.

# 5

## Conclusions and Recommendations

This work aimed to investigate if the fuel consumption of the CC-TS version of the Onera Dragon aircraft concept can be reduced by selecting a different working fluid from cyclopentane. The reference cases of the original Dragon aircraft and the Dragon aircraft equipped with the Organic Rankine Cycle (ORC) system using cyclopentane were re-evaluated using a refined version of the ARENA framework with respect to the original study performed by Krempus.

The Perturbed Chain (PC)-Statistical Associating Fluid Theory (SAFT) Equation of State (EOS), together with Quantitative Structure Property Relationship (QSPR)s for transport properties, are used as a fluid model to perform an integrated system and working fluid optimization. The fluid object instances in the ARENA framework were replaced with the new fluid model. The pure component parameters are treated as continuous design variables. From optimizing the continuous fluid parameters, an optimized pseudo-fluid is found. To limit the design space of the pseudo-fluid and identify corresponding real fluids, a database of 1842 fluids is used. The database is split into polar and non-polar fluids. Fluid families for which the accuracy of the molar mass prediction is insufficient are filtered out. Subsequently, polar and non-polar pseudo-fluid optimizations are run. Additionally, a bi-objective optimization is tested to search for optima for which the PC-SAFT parameters approach those of a real fluid. This is done by introducing an objective function defined as the relative deviation between the PC-SAFT parameters of the pseudo-fluid and corresponding Closest Neighbouring Real Fluid (CNRF), which is the fluid from the database by Esper et al. with the least Euclidean distance in the normalized PC-SAFT space to the pseudo-fluid currently considered. The CNRF for each identified pseudo-fluid optimum is also evaluated. Finally, binary non-polar pseudo-fluid mixtures are optimized.

For the pure fluids, a non-polar pseudo-fluid can decrease the fuel consumption by an additional 0.64 percentage points on top of the 0.92% fuel saving of the ORC system using cyclopentane as a working fluid. The best-performing real fluid identified is the polar fluid acetyl chloride, which showed 0.45 percentage points of additional fuel savings compared to cyclopentane. This is closely followed by the non-polar fluid carbon disulfide with a 0.43 percentage point fuel saving over the Baseline case. Carbon disulfide is highly toxic, and acetyl chloride is corrosive. This most likely renders both fluids unfeasible for an actual ORC application. However, a more thorough investigation is required to draw a definitive conclusion.

The potential fuel savings from optimizing the working fluid are of the same order of magnitude as those achieved with the ORC using cyclopentane. However, the absolute savings on the total fuel mass—82 kg for the best pseudo-fluid and 57 kg for the best real fluid—are small relative to the model's uncertainty, which is approximately 50 kg based on the sensitivity of  $f_1$  to the choice of Heat Transfer Coefficient (HTC) correlations used in the model.

Bi-objective optimization did not identify the best-performing pseudo-fluids or real fluids. Suboptimal algorithm settings or the small number of runs with varying algorithm seeds are likely the main reasons for the poorer performance observed for the bi-objective optimization compared to the single-objective optimizations of pseudo-fluids.

The optimization of a binary pseudo-fluid mixture did not result in better performance compared to a pure pseudo-fluid. In particular, optimizing a binary mixture of cyclopropane and cyclopentane with a variable mixture fraction showed that a temperature glide in the condenser does not provide an advantage for the current system operating with a supercritical cycle. This is likely due to the negative impact of larger heat exchangers on ram drag and overall system mass.

The fact that the optimizer does not find a solution with temperature glide suggests that the detrimental effects of a larger condenser outweigh the benefits of a well-matched temperature profile. However, a subcritical cycle might be able to take advantage of a temperature glide under certain conditions—specifically, if the liquid has a low heat capacity and the latent heat of evaporation is relatively high. In that case, both the condensing and evaporating temperature profiles could closely follow the temperature glide of the heat source.

The integrated pure pseudo-fluid and system optimizations were performed with a variety of algorithm seed values and optimizer settings. Thus, the obtained results are the true optima of the analyzed test cases, apart from the effect of model uncertainties. This is more likely the case for the bi-objective and integrated pseudo-fluid mixture and system optimizations. It is recommended that the bi-objective optimization methodology is thoroughly tested. Then, it can be established whether the bi-objective optimization is an effective approach to implement Computer Aided Molecular Design (CAMD) of ORC systems. In theory a the solution of a bi-objective optimization problem would be the preferred option for CAMD since it combines the pseudo-fluid and real fluid optimization into a single step. The use of a Group Contribution Method (GCM) also represents a valid alternative, though the mathematical problem to be solved may become more complicated as the design vector includes integer variables. However, the fact that the GCM does not allow for the identification of a pseudo-fluid optimum leaves more uncertainty on whether the best fluid is indeed identified. For future optimizations of the system studied in this work, the design variable  $X_{\text{cond}}$  can be set fixed at 1 m if the current bounds are maintained. The optimal values for the design variables  $\xi$  and  $\phi_{1,\text{cond}}$  did not show significant variation across the different optimizations done in the current work. This suggests that these can also be set at a fixed value. However, a more thorough understanding of what could affect the optimal value of these design variables is needed before making this decision.

Given that the fuel savings for the Waste Heat Recovery (WHR) system are small relative to the model uncertainty, it is recommended that the integrated working fluid optimization is applied to airborne WHR systems with more significant fuel-saving potential. One such candidate is the combined cycle turbofan version of the Onera Dragon, as studied by Krempus [25, p. 123].

The following limitations are identified. First, a major limitation is the accuracy in the prediction of the aerodynamic, thermodynamic, volumetric, and gravimetric characteristics of the propulsion system, due to the simplifications introduced in the various models of the *ARENA* framework. For example, the molar mass estimate of the QSPR or the prediction of state properties using the PC-SAFT equation of state are not perfectly accurate. Besides this, the current limitations of the *ARENA* framework include the lack of a gas path analysis for the turboshaft engine, the lack of nacelle drag estimation, and no detailed modelling of the diffuser and nozzle losses downstream of the free power turbine. Furthermore, the genetic algorithm used to optimize the system relies on a stochastic exploration of the design space such that poor algorithm settings may cause that the global optimum is not found and instead the optimization converges to a local optimum. This could be mitigated by repeating the optimizations with different algorithm seeds.

There are also limitations more specifically related to the fluid optimization. The best-performing real fluids identified in this work are those with the PC-SAFT parameters closest to the pseudo-fluid optima. It is possible that the real fluid identified with this method is not the optimal real fluid. While it is not expected that a significant performance increase compared to the results from this work can be achieved, a function fitted to known points, that locally approximates the objective function, with the PC-SAFT parameters as input variables, can be used to create a ranking of fluids and mitigate this limitation.

# References

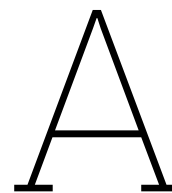
- [1] André Bardow, Klaas Steur, and Joachim Gross. “Continuous-Molecular Targeting for Integrated Solvent and Process Design”. In: *Industrial & Engineering Chemistry Research* 49.6 (Mar. 2010). Publisher: American Chemical Society, pp. 2834–2840. ISSN: 0888-5885. DOI: 10.1021/ie901281w. URL: <https://doi.org/10.1021/ie901281w> (visited on 12/06/2024).
- [2] Samil Beret and J. M. Prausnitz. “Perturbed hard-chain theory: An equation of state for fluids containing small or large molecules”. de. In: *AIChE Journal* 21.6 (1975), pp. 1123–1132. ISSN: 1547-5905. DOI: 10.1002/aic.690210612. URL: <https://onlinelibrary.wiley.com/doi/abs/10.1002/aic.690210612> (visited on 03/06/2025).
- [3] Walter G. Chapman, George Jackson, and Keith E. Gubbins. “Phase equilibria of associating fluids: Chain molecules with multiple bonding sites”. In: *Molecular Physics* 65.5 (Dec. 1988). Publisher: Taylor & Francis \_eprint: <https://doi.org/10.1080/00268978800101601>, pp. 1057–1079. ISSN: 0026-8976. DOI: 10.1080/00268978800101601. URL: <https://doi.org/10.1080/00268978800101601> (visited on 03/06/2025).
- [4] Walter G. Chapman et al. “New reference equation of state for associating liquids”. In: *Industrial & Engineering Chemistry Research* 29.8 (Aug. 1990). Publisher: American Chemical Society, pp. 1709–1721. ISSN: 0888-5885. DOI: 10.1021/ie00104a021. URL: <https://doi.org/10.1021/ie00104a021> (visited on 03/06/2025).
- [5] Ting Horng Chung, Lloyd L. Lee, and Kenneth E. Starling. “Applications of kinetic gas theories and multiparameter correlation for prediction of dilute gas viscosity and thermal conductivity”. In: *Industrial & Engineering Chemistry Fundamentals* 23.1 (Feb. 1984). Publisher: American Chemical Society, pp. 8–13. ISSN: 0196-4313. DOI: 10.1021/i100013a002. URL: <https://doi.org/10.1021/i100013a002> (visited on 01/24/2025).
- [6] P Colonna, T.P. Van der Stelt, and A. Guardone. *FluidProp*.
- [7] DABO KREMPUS et al. “Organic Rankine Cycle Waste Heat Recovery for Turbohaft Engines of Turboelectric Aircraft”. Eng. In: (2023). Artwork Size: 18 pages Medium: PDF Publisher: [object Object], 18 pages. DOI: 10.13009/EUCASS2023-658. URL: <https://www.eucass.eu/doi/EUCASS2023-658.pdf> (visited on 05/15/2024).
- [8] Reynard De Vries and Roelof Vos. “Aerodynamic Performance Benefits of Over-the-Wing Distributed Propulsion for Hybrid-Electric Transport Aircraft”. en. In: *Journal of Aircraft* 60.4 (July 2023), pp. 1201–1218. ISSN: 0021-8669, 1533-3868. DOI: 10.2514/1.C036909. URL: <https://arc.aiaa.org/doi/10.2514/1.C036909> (visited on 01/10/2024).
- [9] Delft University of Technology + Technische Universität Braunschweig et al. “Impact of the working fluid in orc-based waste heat recovery systems for turboshaft engines”. In: Sept. 2024. DOI: 10.33737/gpps24-tc-075. URL: [https://gpps.global/wp-content/uploads/2024/09/GPPS-TC-2024\\_paper\\_075.pdf](https://gpps.global/wp-content/uploads/2024/09/GPPS-TC-2024_paper_075.pdf) (visited on 03/03/2025).
- [10] Han Deng et al. “A new simplified model for condensation heat transfer of zeotropic mixtures inside horizontal tubes”. In: *Applied Thermal Engineering* 153 (May 2019), pp. 779–790. ISSN: 1359-4311. DOI: 10.1016/j.applthermaleng.2019.02.128. URL: <https://www.sciencedirect.com/science/article/pii/S135943111837529X> (visited on 06/14/2024).
- [11] M. D. Donohue and J. M. Prausnitz. “Perturbed hard chain theory for fluid mixtures: Thermodynamic properties for mixtures in natural gas and petroleum technology”. en. In: *AIChE Journal* 24.5 (1978). \_eprint: <https://onlinelibrary.wiley.com/doi/pdf/10.1002/aic.690240511>, pp. 849–860. ISSN: 1547-5905. DOI: 10.1002/aic.690240511. URL: <https://onlinelibrary.wiley.com/doi/abs/10.1002/aic.690240511> (visited on 03/06/2025).

- [12] *Elite Status: How a small minority around the world take an unfair share of flights*. en-US. Mar. 2021. URL: <https://www.wearepossible.org/latest-news/elite-status-how-a-small-minority-around-the-world-take-an-unfair-share-of-flights> (visited on 05/22/2024).
- [13] *ESDU 86002: Auxiliary air inlet pressure recovery characteristics*. URL: [https://www.esdu.com/cgi-bin/ps.pl?t=doc&p=esdu\\_86002d](https://www.esdu.com/cgi-bin/ps.pl?t=doc&p=esdu_86002d) (visited on 02/06/2025).
- [14] Timm Esper et al. "PCP-SAFT Parameters of Pure Substances Using Large Experimental Databases". In: *Industrial & Engineering Chemistry Research* 62.37 (Sept. 2023). Publisher: American Chemical Society, pp. 15300–15310. ISSN: 0888-5885. DOI: 10.1021/acs.iecr.3c02255. URL: <https://doi.org/10.1021/acs.iecr.3c02255> (visited on 12/19/2024).
- [15] J. W. Gauntner. *Algorithm for calculating turbine cooling flow and the resulting decrease in turbine efficiency*. Tech. rep. NASA-TM-81453. NTRS Author Affiliations: NASA Lewis Research Center NTRS Document ID: 19800011581 NTRS Research Center: Legacy CDMS (CDMS). Feb. 1980. URL: <https://ntrs.nasa.gov/citations/19800011581> (visited on 01/24/2025).
- [16] V. Gnielinski. "New equations for heat and mass transfer in turbulent pipe and channel flow". In: 1976. URL: <https://www.semanticscholar.org/paper/New-equations-for-heat-and-mass-transfer-in-pipe-Gnielinski/47764632bbcc7f797d3bc65c2ed997a31a723a26> (visited on 02/25/2025).
- [17] Joachim Gross and Gabriele Sadowski. "Application of the Perturbed-Chain SAFT Equation of State to Associating Systems". In: *Industrial & Engineering Chemistry Research* 41.22 (Oct. 2002). Publisher: American Chemical Society, pp. 5510–5515. ISSN: 0888-5885. DOI: 10.1021/ie010954d. URL: <https://doi.org/10.1021/ie010954d> (visited on 06/06/2024).
- [18] Joachim Gross and Gabriele Sadowski. "Perturbed-Chain SAFT: An Equation of State Based on a Perturbation Theory for Chain Molecules". In: *Industrial & Engineering Chemistry Research* 40.4 (Feb. 2001). Publisher: American Chemical Society, pp. 1244–1260. ISSN: 0888-5885. DOI: 10.1021/ie0003887. URL: <https://doi.org/10.1021/ie0003887> (visited on 06/06/2024).
- [19] Eric S. Hendricks and Justin S. Gray. "pyCycle: A Tool for Efficient Optimization of Gas Turbine Engine Cycles". en. In: *Aerospace* 6.8 (Aug. 2019), p. 87. ISSN: 2226-4310. DOI: 10.3390/aerospace6080087. URL: <https://www.mdpi.com/2226-4310/6/8/87> (visited on 01/24/2025).
- [20] Momar Hughes and John Olsen. "Fuel Burn Reduction of Hybrid Aircraft Employing an Exhaust Heat Harvesting System". In: *Journal of Propulsion and Power* 38.2 (2022). Publisher: American Institute of Aeronautics and Astronautics \_eprint: <https://doi.org/10.2514/1.B38393>, pp. 241–253. ISSN: 0748-4658. DOI: 10.2514/1.B38393. URL: <https://doi.org/10.2514/1.B38393> (visited on 06/10/2024).
- [21] William Stanley Jevons. *The Coal Question: An Enquiry Concerning the Progress of the Nation, and the Probable Exhaustion of Our Coal-mines*. en. Google-Books-ID: gAAKAAAAIAAJ. Macmillan, 1865. ISBN: 978-1-78987-646-8.
- [22] José C. Jiménez-García et al. "A Comprehensive Review of Organic Rankine Cycles". en. In: *Processes* 11.7 (July 2023). Number: 7 Publisher: Multidisciplinary Digital Publishing Institute, p. 1982. ISSN: 2227-9717. DOI: 10.3390/pr11071982. URL: <https://www.mdpi.com/2227-9717/11/7/1982> (visited on 01/31/2025).
- [23] K.G. JOBACK and R.C. REID. "Estimation of Pure-Component Properties from Group-Contributions". In: *Chemical Engineering Communications* 57.1-6 (July 1987). Publisher: Taylor & Francis \_eprint: <https://doi.org/10.1080/00986448708960487>, pp. 233–243. ISSN: 0098-6445. DOI: 10.1080/00986448708960487. URL: <https://doi.org/10.1080/00986448708960487> (visited on 05/30/2024).
- [24] Alan R. Katritzky, Victor S. Lobanov, and Mati Karelson. "QSPR: the correlation and quantitative prediction of chemical and physical properties from structure". en. In: *Chemical Society Reviews* 24.4 (1995), p. 279. ISSN: 0306-0012, 1460-4744. DOI: 10.1039/cs9952400279. URL: <https://xlink.rsc.org/?DOI=cs9952400279> (visited on 05/27/2024).
- [25] D. Krempus. "Organic Rankine Cycle Waste Heat Recovery Systems for Aircraft Engines". en. In: (2025). URL: <https://repository.tudelft.nl/record/uuid:5e565f99-a9f4-4208-95e9-2c542fd720f8> (visited on 02/07/2025).

- [26] Dabo Krempus et al. "On mixtures as working fluids of air-cooled ORC bottoming power plants of gas turbines". en. In: *Applied Thermal Engineering* 236 (Jan. 2024), p. 121730. ISSN: 13594311. DOI: 10.1016/j.applthermaleng.2023.121730. URL: <https://linkinghub.elsevier.com/retrieve/pii/S1359431123017593> (visited on 05/15/2024).
- [27] M. Lampe et al. "Simultaneous Optimization of Working Fluid and Process for Organic Rankine Cycles Using PC-SAFT". en. In: *Industrial & Engineering Chemistry Research* 53.21 (May 2014), pp. 8821–8830. ISSN: 0888-5885, 1520-5045. DOI: 10.1021/ie5006542. URL: <https://pubs.acs.org/doi/10.1021/ie5006542> (visited on 04/30/2024).
- [28] D. S. Lee et al. "The contribution of global aviation to anthropogenic climate forcing for 2000 to 2018". In: *Atmospheric Environment* 244 (Jan. 2021), p. 117834. ISSN: 1352-2310. DOI: 10.1016/j.atmosenv.2020.117834. URL: <https://www.sciencedirect.com/science/article/pii/S1352231020305689> (visited on 05/22/2024).
- [29] Oliver Lötgering-Lin and Joachim Gross. "Group Contribution Method for Viscosities Based on Entropy Scaling Using the Perturbed-Chain Polar Statistical Associating Fluid Theory". In: *Industrial & Engineering Chemistry Research* 54.32 (Aug. 2015). Publisher: American Chemical Society, pp. 7942–7952. ISSN: 0888-5885. DOI: 10.1021/acs.iecr.5b01698. URL: <https://doi.org/10.1021/acs.iecr.5b01698> (visited on 06/13/2024).
- [30] M. Stavrou. "Integrated process and solvent design for CO<sub>2</sub> capture using Continuous Molecular Targeting - Computer Aided Molecular Design (CoMT-CAMD)". PhD thesis. [object Object], 2017. DOI: 10.4233/UUID:B44DE3D4-25DD-453C-988C-07FCA027A612. URL: <http://resolver.tudelft.nl/uuid:b44de3d4-25dd-453c-988c-07fca027a612> (visited on 04/30/2024).
- [31] Ennio Macchi and Marco Astolfi, eds. *Organic rankine cycle (ORC) power systems: technologies and applications*. eng. Woodhead publishing series in energy number 107. Amsterdam Boston Cambridge Heidelberg: Elsevier, Woodhead Publishing, 2017. ISBN: 978-0-08-100511-8 978-0-08-100510-1.
- [32] Mark R. Nichols. *Investigation of flow through an intercooler set at various angles to the supply duct*. NTRS Author Affiliations: NTRS Report/Patent Number: NACA-WR-L-408 NTRS Document ID: 19930093676 NTRS Research Center: Legacy CDMS (CDMS). Apr. 1942. URL: <https://ntrs.nasa.gov/citations/19930093676> (visited on 02/07/2025).
- [33] Ed Obert. *Aerodynamic Design of Transport Aircraft*. en. Google-Books-ID: V1DuJfPov48C. IOS Press, 2009. ISBN: 978-1-58603-970-7.
- [34] ONERA. *DRAGON : Comment réduire la consommation de carburant ? / How to reducing fuel consumption ?* June 2019. URL: <https://www.youtube.com/watch?v=B-GyFihMUVU> (visited on 02/10/2025).
- [35] Athanasios I. Papadopoulos, Mirko Stijepovic, and Patrick Linke. "On the systematic design and selection of optimal working fluids for Organic Rankine Cycles". In: *Applied Thermal Engineering* 30.6 (May 2010), pp. 760–769. ISSN: 1359-4311. DOI: 10.1016/j.applthermaleng.2009.12.006. URL: <https://www.sciencedirect.com/science/article/pii/S1359431109003536> (visited on 05/28/2024).
- [36] Athanasios I. Papadopoulos et al. "Toward Optimum Working Fluid Mixtures for Organic Rankine Cycles using Molecular Design and Sensitivity Analysis". en. In: *Industrial & Engineering Chemistry Research* 52.34 (Aug. 2013), pp. 12116–12133. ISSN: 0888-5885, 1520-5045. DOI: 10.1021/ie400968j. URL: <https://pubs.acs.org/doi/10.1021/ie400968j> (visited on 04/30/2024).
- [37] Christopher A. Perullo, Dimitri N. Mavris, and Eduardo Fonseca. "An Integrated Assessment of an Organic Rankine Cycle Concept for Use in Onboard Aircraft Power Generation". In: *Volume 2: Aircraft Engine; Coal, Biomass and Alternative Fuels; Cycle Innovations*. San Antonio, Texas, USA: American Society of Mechanical Engineers, June 2013, V002T01A028. ISBN: 978-0-7918-5513-3. DOI: 10.1115/GT2013-95734. URL: <https://asmedigitalcollection.asme.org/GT/proceedings/GT2013/55133/San%20Antonio,%20Texas,%20USA/236124> (visited on 05/23/2024).
- [38] PubChem. *Acetic Anhydride*. en. URL: <https://pubchem.ncbi.nlm.nih.gov/compound/7918> (visited on 01/31/2025).

- [39] PubChem. *Acetyl chloride*. en. URL: <https://pubchem.ncbi.nlm.nih.gov/compound/6367> (visited on 01/31/2025).
- [40] PubChem. *Carbon Disulfide*. en. URL: <https://pubchem.ncbi.nlm.nih.gov/compound/6348> (visited on 01/31/2025).
- [41] PubChem. *Methacrolein*. en. URL: <https://pubchem.ncbi.nlm.nih.gov/compound/6562> (visited on 01/31/2025).
- [42] Philipp Rehner, André Bardow, and Joachim Gross. *Modeling mixtures with PC-SAFT: Insights from large-scale parametrization and group-contribution method for binary interaction parameters*. Aug. 2023. DOI: 10.21203/rs.3.rs-3296113/v1. URL: <https://www.researchsquare.com/article/rs-3296113/v1> (visited on 04/30/2024).
- [43] Dan Rutherford and Sola Zheng. *Fuel burn of new commercial jet aircraft: 1960 to 2019*. en-US. Tech. rep. International Council on Clean Transportation, Sept. 2020. URL: <https://theicct.org/publication/fuel-burn-of-new-commercial-jet-aircraft-1960-to-2019/> (visited on 03/06/2025).
- [44] Sebastian Samuelsson, Konstantinos G. Kyprianidis, and Tomas Grönstedt. “Consistent Conceptual Design and Performance Modeling of Aero Engines”. en. In: American Society of Mechanical Engineers Digital Collection, Aug. 2015. DOI: 10.1115/GT2015-43331. URL: <https://dx.doi.org/10.1115/GT2015-43331> (visited on 12/23/2024).
- [45] S. R. S. Sastri and K. K. Rao. “A simple method to predict surface tension of organic liquids”. In: *The Chemical Engineering Journal and the Biochemical Engineering Journal* 59.2 (Oct. 1995), pp. 181–186. ISSN: 0923-0467. DOI: 10.1016/0923-0467(94)02946-6. URL: <https://www.sciencedirect.com/science/article/pii/0923046794029466> (visited on 01/24/2025).
- [46] Elmar Sauer, Marina Stavrou, and Joachim Gross. “Comparison between a Homo- and a Heterosegmented Group Contribution Approach Based on the Perturbed-Chain Polar Statistical Associating Fluid Theory Equation of State”. In: *Industrial & Engineering Chemistry Research* 53.38 (Sept. 2014). Publisher: American Chemical Society, pp. 14854–14864. ISSN: 0888-5885. DOI: 10.1021/ie502203w. URL: <https://doi.org/10.1021/ie502203w> (visited on 05/30/2024).
- [47] J. Schilling et al. “Towards optimal mixtures of working fluids: Integrated design of processes and mixtures for Organic Rankine Cycles”. en. In: *Renewable and Sustainable Energy Reviews* 135 (Jan. 2021), p. 110179. ISSN: 13640321. DOI: 10.1016/j.rser.2020.110179. URL: <https://linkinghub.elsevier.com/retrieve/pii/S1364032120304688> (visited on 04/30/2024).
- [48] Johannes Schilling et al. “1-stage CoMT-CAMD: An approach for integrated design of ORC process and working fluid using PC-SAFT”. en. In: *Chemical Engineering Science* 159 (Feb. 2017), pp. 217–230. ISSN: 00092509. DOI: 10.1016/j.ces.2016.04.048. URL: <https://linkinghub.elsevier.com/retrieve/pii/S0009250916302196> (visited on 04/30/2024).
- [49] Peter Schmollgruber et al. “Multidisciplinary Design and performance of the ONERA Hybrid Electric Distributed Propulsion concept (DRAGON)”. In: *AIAA Scitech 2020 Forum*. AIAA SciTech Forum. American Institute of Aeronautics and Astronautics, Jan. 2020. DOI: 10.2514/6.2020-0501. URL: <https://arc.aiaa.org/doi/10.2514/6.2020-0501> (visited on 12/03/2024).
- [50] C. M. de Servi et al. “Exploratory assessment of a combined-cycle engine concept for aircraft propulsion”. en. In: *Proceedings of the 1st Global Power and Propulsion Forum* (2017). URL: <https://repository.tudelft.nl/islandora/object/uuid%3A9150dd0e-b2ef-46dd-8b1d-9bd59831e234> (visited on 05/15/2024).
- [51] Mirza M. Shah. “Improved correlation for heat transfer during condensation in conventional and mini/micro channels”. In: *International Journal of Refrigeration* 98 (Feb. 2019), pp. 222–237. ISSN: 0140-7007. DOI: 10.1016/j.ijrefrig.2018.07.037. URL: <https://www.sciencedirect.com/science/article/pii/S0140700718302871> (visited on 12/03/2024).
- [52] Dawid Taler. “Simple power-type heat transfer correlations for turbulent pipe flow in tubes”. en. In: *Journal of Thermal Science* 26.4 (Aug. 2017). Company: Springer Distributor: Springer Institution: Springer Label: Springer Number: 4 Publisher: Science Press, pp. 339–348. ISSN: 1993-033X. DOI: 10.1007/s11630-017-0947-2. URL: <https://link-springer-com.tudelft.idm.oclc.org/article/10.1007/s11630-017-0947-2> (visited on 02/25/2025).

- [53] M. S. Wertheim. “Fluids with highly directional attractive forces. I. Statistical thermodynamics”. en. In: *Journal of Statistical Physics* 35.1 (Apr. 1984), pp. 19–34. ISSN: 1572-9613. DOI: 10.1007/BF01017362. URL: <https://doi.org/10.1007/BF01017362> (visited on 03/06/2025).
- [54] M. S. Wertheim. “Fluids with highly directional attractive forces. II. Thermodynamic perturbation theory and integral equations”. In: *Journal of Statistical Physics* 35 (Apr. 1984). Publisher: Springer ADS Bibcode: 1984JSP...35...35W, pp. 35–47. ISSN: 0022-4715. DOI: 10.1007/BF01017363. URL: <https://ui.adsabs.harvard.edu/abs/1984JSP...35...35W> (visited on 03/06/2025).
- [55] M. S. Wertheim. “Fluids with highly directional attractive forces. III. Multiple attraction sites”. en. In: *Journal of Statistical Physics* 42.3 (Feb. 1986), pp. 459–476. ISSN: 1572-9613. DOI: 10.1007/BF01127721. URL: <https://doi.org/10.1007/BF01127721> (visited on 03/06/2025).
- [56] M. S. Wertheim. “Fluids with highly directional attractive forces. IV. Equilibrium polymerization”. en. In: *Journal of Statistical Physics* 42.3 (Feb. 1986), pp. 477–492. ISSN: 1572-9613. DOI: 10.1007/BF01127722. URL: <https://doi.org/10.1007/BF01127722> (visited on 03/06/2025).



## Figures Related to Fluid Modeling

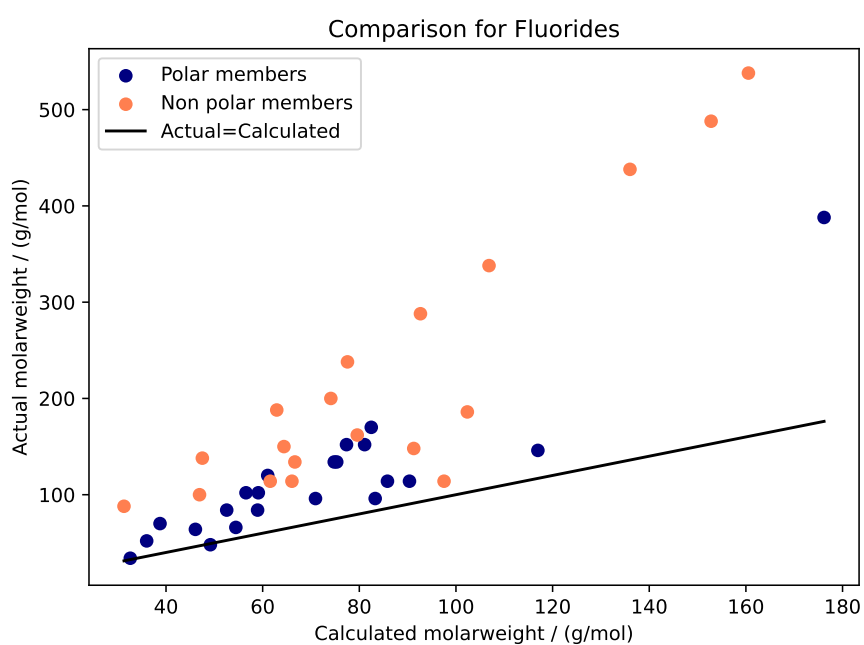


**Figure A.1:** Comparison of molar mass and molar mass estimated by the QSPR from ref. [30] for the substances in the fluorides family in the database from ref. [14].

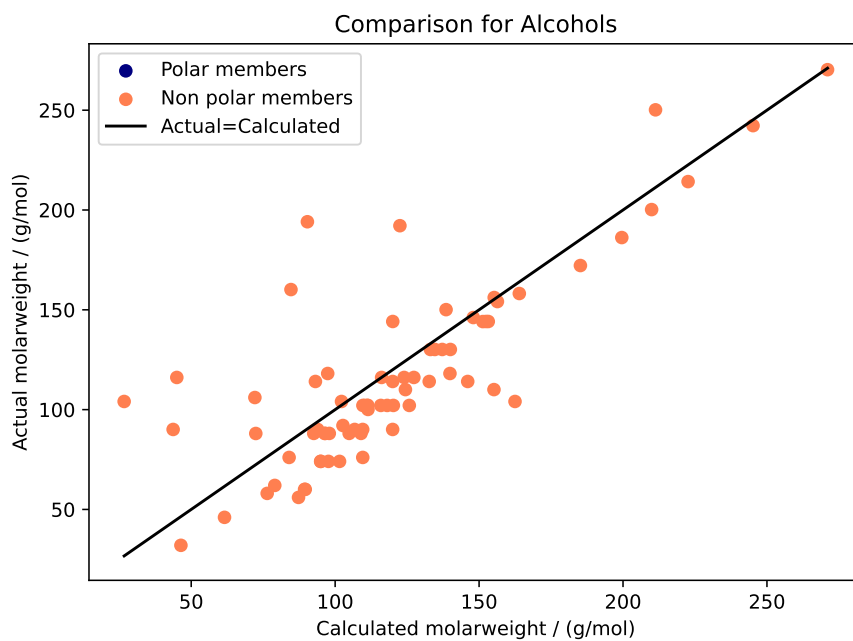


**Figure A.2:** Comparison of molar mass and molar mass estimated by the QSPR from ref. [30] for the substances in the alcohols family in the database from ref. [14].

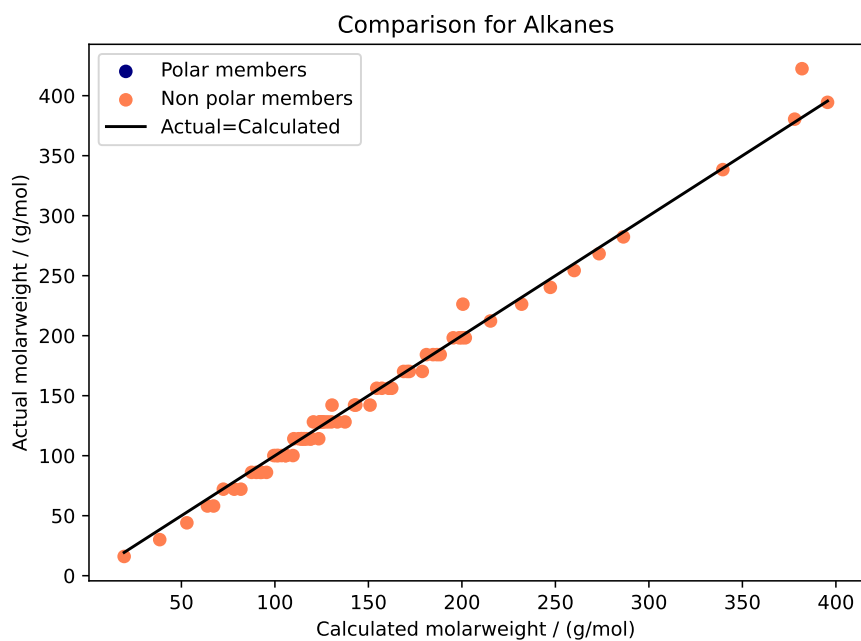


**Figure A.3:** Comparison of molar mass and molar mass estimated by the QSPR from ref. [30] for the substances in the alkanes family in the database from ref. [14].

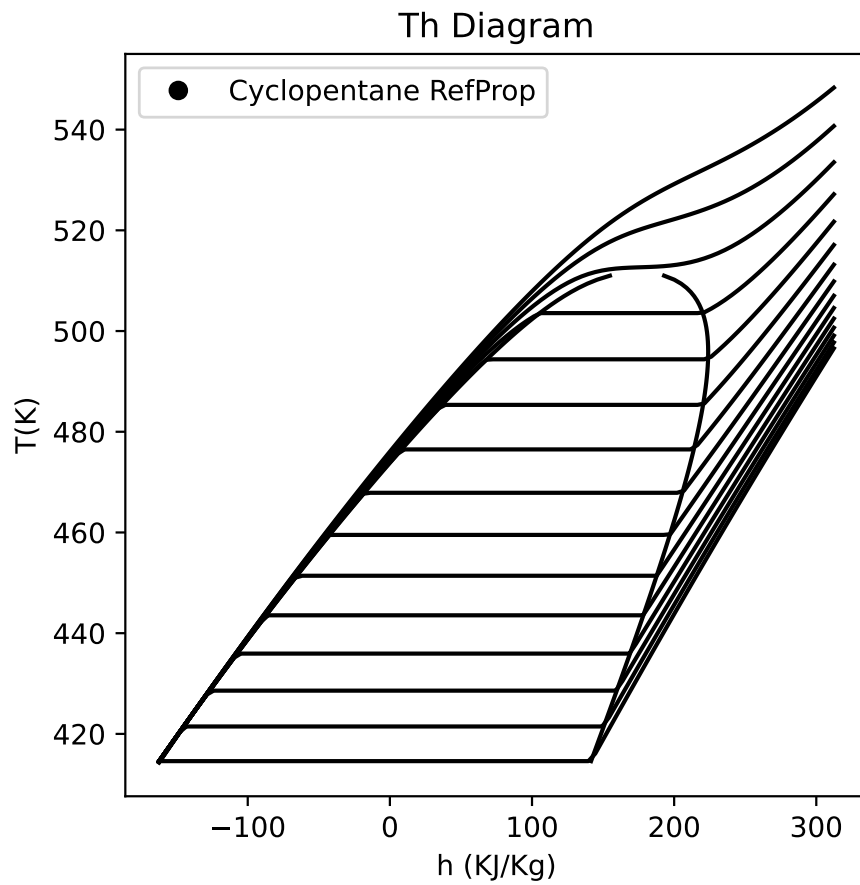


**Figure A.4:** T-h diagram for cyclopentane from *REFPROP* data showing a heat capacity spike near the critical point, marked by flattening isobars. As pressure increases above the critical pressure, this flattening becomes less pronounced.